A METHOD FOR PIXEL-BY-PIXEL ABSOLUTE QUANTITATION IN POSITRON EMISSION TOMOGRAPHY

To my children,
Calin and Irina.

A METHOD FOR PIXEL-BY-PIXEL ABSOLUTE QUANTITATION IN POSITRON EMISSION TOMOGRAPHY

by

ALINA POPESCU, Ph.D.

A Project Report
Submitted to the School of Graduate Studies
in Partial Fulfilment of the Requirements
for the Degree of
Master of Science

McMaster University

MASTER OF SCIENCE (1990) McMASTER UNIVERSITY
(Physics) Hamilton, Ontario

TITLE: A Method for Pixel-by-Pixel Absolute Quantitation in Positron Emission Tomography

AUTHOR: Alina Popescu, B.Sc. (Bucharest University, Romania)
M.Sc. (Bucharest University, Romania)
Ph.D. (Central Institute of Physics, Bucharest, Romania)

SUPERVISOR: Dr. C. Nahmias

NUMBER OF PAGES: VII, 178

Abstract.

This study attempts to develop a method for absolute quantitation in Positron Emission Tomography. This includes the definition of the dimension and the position of a tumour in the brain as well as the evaluation of the amount of drug delivered to the tumour and to surrounding tissues in a pixel-by-pixel way, from the image. The defined objectives can be achieved using the calibrated FWHM values of the distribution of events in the tumour image, versus distance, to determine the dimension and the position of the tumour. The concentration activity in the tumour and the tumour-to-nontumour activity ratios can be obtained from the image, using a modified filter and the calibration of the tomograph. The colour scale of the image can be expressed in absolute units (μCi/ml) and the concentration activity can be evaluated in each pixel of the image or in each volume element of the body.

Acknowledgements.

I would like to express my gratitude to Dr. E.S. Garnett, the Director of the Nuclear Medicine Department of the McMaster Hospital for the creative discussions, for his help and support in realising this study.

I will not forget the advice, the coordination received from Dr. Brian Wilson in this period of my life as a student in Canada.

I would like to thank to Dr. C. Webber and to other members of the Nuclear Medicine Department who helped me in different ways.

I would like to thank for all my heart to Kay Brown for the help in preparing the radioisotopes used in these experiments, for her support and understanding.

The discussions with Martin Locken helped me in a better understanding of this complicated system named PET.

I would like to thank to Alex Kotzeff for his invaluable help in obtaining the experimental data included in this study.

I could not forget the collaboration of Dr. Tom Farrell.

I would like to thank to my supervisor, Dr. C. Nahmias for useful discussions and observations regarding this study.

TABLE OF CONTENT.

1. INTRODUCTION

The word *tomogram* is derived from the Greek words *tomos*, a cutting (section) and *gramma*, a writing.

The purpose of Positron Emission Tomography is the reconstruction of an image that faithfully reproduces the spatial distribution of a radiotracer in the body. The method serves an unique and important role in medical research permitting a non-invasive digital cross-section of the activity distribution of a β^+ labelled compound within a patient.

PET method has unique capabilities in analyzing the biochemical status of tissues. Indices such as: metabolic rate of glucose utilization, oxygen extraction fraction, metabolic rate of oxygen utilization, provide significant dimensions in interpreting the results of a PET procedure.

PET has the possibility to distinguish normal from abnormal functions of tissues, the ability to assess various neurological diseases such as: Parkinson, Huntington, various types of epilepsy, to evaluate regional blood flow, tissue damage from stroke, etc.

The ultimate goal of these functional studies is to provide absolute quantitative data with standardized, reproductibile and accurate methods of obtaining and analyzing data. However, current PET and SPECT (Single Photon Emission Computed Tomography) methodologies have been significantly limited by data analysis. In addition to the image distortion associated with scattering and accidental coincidences, spatial nonuniformity, count rate nonlinearity, etc., the reconstruction procedure seriously affects the quantitative capability of a nuclear medicine imaging system.

The purpose of this study is to introduce a reliable method capable of determining the position and the dimensions of the tumour, to evaluate the amount of activity delivered to a tumour and to surrounding tissues from the PET images, in a pixel-by-pixel way.

2. POSITRON EMISSION TOMOGRAPHY (PET) METHOD

The ability of PET instrumentation to measure tracer concentration is strongly dependent on the physical processes involved in positron emission, the detection of the annihilation photons and the tomographic reconstruction.

2.1 Physics of Positron Emission Tomography.

2.1.1 The positron emitting radionuclides used in PET.

A. Isotope Selection

The primary isotopes of interest for PET are listed in Table 2.1. [1, 2]

^{11}C, ^{13}N and ^{15}O are extremely important since their stable counterparts are the building blocks of the chemical constituents of the body, and can be replaced by these radioactive nuclei without changing the relevant biochemistry. The decay half-lives of ^{11}C (20.3 min) and ^{13}N (10 min) are sufficiently long to permit chemical synthesis, but short enough to avoid excessive patient dose. ^{15}O (124 sec) labeled tracers are simply gases, including ^{15}O labeled oxygen gas, carbon monoxide (CO) and also liquid water.

^{18}F (110 min) can substitute for hydrogen in a molecule in many cases without destroying the significance of the biological response and it is the label in ^{18}F-FDG, a glucose analog.

^{55}Co has served for the labelling of radiopharmaceuticals used for tumour detection.

^{75}Br and ^{76}Br provides a useful label, its chemistry is simpler than that of ^{18}F.

^{68}Ga is suitable for incorporation in a radiotracer, labelling of microspheres for regional blood flow determination or of protein for regional blood volume studies. ^{68}Ga-labelled compounds have been employed clinically to detect molecular diffusion resulting from disruption of the blood-brain barrier.

Table 2.1 The primary isotopes of interest for PET.

Isotope	Half-life	% β^+ decay	Daughter	Means of production
^{11}C	20.3 min	99.8	^{11}B stable	Cyclotron
^{13}N	10.0 min	100	^{13}C stable	Cyclotron
^{15}O	124 sec	99.9	^{15}N stable	Cyclotron
^{18}F	110 min	96.9	^{18}O stable	Cyclotron
^{38}K	7.7 min	100	^{38}Ar stable	Cyclotron
^{55}Co	18 h	81	^{55}Fe ($T_{1/2}$=2.5 h)	Cyclotron
^{62}Cu	9.8 min	97	^{62}Ni stable	^{62}Zn generator Cyclotron
^{68}Ga	68.3 min	87	^{68}Zn stable	^{68}Ge generator
^{75}Br	1.6 h	90	^{75}Se ($T_{1/2}$=120 d)	Cyclotron
^{76}Br	16.1 h	67	^{76}Se stable	Cyclotron
^{82}Rb	75 sec	96	^{82}Kr stable	^{82}Sr generator

^{68}Ge-^{68}Ga solution is valuable in the laboratory for attenuation corrections, calibration and other utility functions.

^{82}Rb is a generator produced isotope that is useful as a myocardial flow tracer.

B. Isotope Production.

It would be most convenient if positron emitters were available from generator systems, as daughters of long-lived isotopes. The:

$$^{68}Ge \xrightarrow[EC]{280\ d} {}^{68}Ga \xrightarrow[\beta^+]{68\ min}$$

and

$$^{82}Sr \xrightarrow[EC]{25\ d} {}^{82}Rb \xrightarrow[\beta^+]{75\ sec}$$

generators, are two such systems. [3] Otherwise these isotopes must be produced by nuclear reactions. [2]

The radionuclides that are produced by positron generator systems have the same type of growth-decay kinetics as other types of generators. These relations are illustrated by:

Parent		Daughter		Grand daughter
N_1	$\longrightarrow$	N_2	$\longrightarrow$	N_3
A_1	T_1	A_2	T_2	Stable

In the case of these positron generator systems, the half lives of the daughters are much shorter than the half lives of the parents. As a result, for this situation, a secular equilibrium is reached when the activity of the parent is equal to that of the daughter:

$$\lambda_1 N_1 = \lambda_2 N_2 \qquad (2.1)$$

A great deal of effort has been devoted to the development of radiochemical separation of daughter from parent activities, suitable for short lived radionuclides. Because of operational simplicity and the potential for high selectivity with the direct production of physiologically compatible solutions, liquid column chromatography has generally proven to be the separation method of choice for generator systems. [3]

The PET techniques are used for monitoring, and in some cases quantitatively measuring, physiologic and metabolic parameters in vivo in humans, in a noninvasive fashion. The use of labelled compounds in most of these studies coupled with the unavailability of generator produced positron emitters that are suitable for labeling such tracers, has effectively eliminated the use of generator produced positron emitters for such measurements.

The positron emitters are isotopes that have fewer neutrons than protons and are most easily produced by bombardment of nuclei by protons, deuterons and alpha particles, although there are some possible neutron induced reactions. A partial list of suitable reactions for production of positron emitters by nuclear reactions is presented in Table 2.2. [4, 5]

It is important to point that:

- the rate of isotope production increases rapidly once the beam energy exceeds the Coulomb barrier in the entrance channel, up to a stabilized value. Practical beam energies for production of light isotopes are 8-20 MeV where facility of beam transport, target foil penetration, and the cross section reaction are the important considerations. Excessively high energy will produce long-lived, undesired isotopes that contaminate the product without significantly increasing reaction yields.
- the yield of isotopes approaches *saturation yield* exponentially, where the decay and production of nuclei are equal. One obtains 75% of saturation, for bombardment times of two half-lives. [5] Table 2.2 indicates that the saturation yields per microampere (μA) current for the light isotopes of interest are roughly comparable for E = 8-20 MeV.
- the proton reactions can be used for all the desired isotopes but deuteron beams can be used without enriched expensive targets, at lower cost. However, deuteron acceleration requires larger cyclotrons than proton acceleration for comparable beam energy.

Table 2.2 Positron Emitters Produced by Proton and Deuteron Reactions.

Isotope	Reaction	Beam energy (MeV)	Saturation per μA (mCi)	Yield (MBq)	Comments
^{11}C	$^{14}N(p,\alpha)^{11}C$	14 8	130 36	4810 1332	
	$^{10}B(\alpha,n)^{11}C$	8	13	481	
	$^{11}B(p,n)^{11}C$	12	210	7770	
^{13}N	$^{13}C(p,n)^{13}N$*	8	82	3034	^{13}C 1.1% of C
	$^{16}O(p,\alpha)^{13}N$	20	54	1998	
	$^{11}C(d,n)^{13}N$	8	50	1850	
^{15}O	$^{14}N(d,n)^{15}O$	8	50	1850	
	$^{15}N(p,n)^{15}O$*	8	47	1739	^{15}N 0.36% of N
^{18}F	$^{20}Ne(d,\alpha)^{18}F$	14 8	84 46	3108 1702	
	$^{18}O(p,n)^{18}F$*	14 8	216 110	7992 4070	^{18}O 0.2% of O
	$^{16}O(t,p)^{18}F$	22	20	740	

*Requires enriched target

C. Radiotracers

A radiopharmaceutical becomes a positron emitting radiotracer by having one of its natural atoms replaced by a radionuclide that decays by positron emission. The radiotracer enters the subject's circulating system either through an intravenous injection or by inhalation.

An important feature in the radiotracer production must be the ease and speed with which the final product is made and transported to the clinical setting. Some compounds can be prepared in a continuous process so that, they are available at the end of the bombardment, or very shortly after, whereas others require synthetic procedure before they are available.

The rational choice of a compound to be labeled for some particular PET application presents a challenge that requires an understanding not only of the interactions between chemical compounds and living systems but also of the limitations of PET in providing data from which biochemical measurements can be made.

PET measures regional concentrations of radioactivity, its ingress and egress from the region of the body. Thus, the concentration and rate are the two accessible measurements obtained from the PET itself. Further informations such as the nature of the metabolism etc., must be obtained by other methods. A model that allows the determination of the particular process, e.g., glucose metabolism, is required.

The major objectives in setting priorities for radiotracer synthesis have been directed toward development of labelled compounds that could be used to probe blood flow, oxygen metabolism, glucose metabolism, protein synthesis and neurotransmiter receptor properties. Tracers for the measurement of tissue proliferation, tissue pH, drug distribution profiles, steroid receptor properties and lung metabolism have been described also. [4, 5]

Labelled Sugars.

The most widely used method is the FDG method. The common method of synthesis is via electrophilic fluorination using fluorination reagents derived from ^{18}F-labeled elemental fluorine. [4] However, the nucleophilic fluorination reactions which lead to an isomerically pure product in high yields and high specific activity are being used. [4]

^{11}C-2-deoxy D glucose (^{11}C-2DG) is also used for measuring regional glucose metabolism. The shorter half-life of 20 min for ^{11}C compared to 110 min half-life of ^{18}F allows serial studies to be performed at short time intervals. The synthesis of ^{11}C-2DG from H[^{11}C]N is rapid. [4]

Labelled Amino-Acids.

The study of protein metabolism as well as certain aspects of neurotransmitter receptor populations requires labelled amino-acids.

There are two different radiotracers for measuring regional brain protein synthesis: C-leucine (^{11}C-carboxyl) and [^{11}C-methyl]-methionine. The studies comparing C-leucine and C-methionine showed that leucine provided a better measure of brain protein synthesis with PET. [6]

Labelled Neurotransmitter Radiotracers.

The study of neurotransmitter dopamine has been approached by using labelled antagonists to the dopamine receptor or by using labelled precursors to dopamine. Dopamine itself, unfortunately, does not cross the blood brain barrier. A suitable derivative that crosses the blood brain barrier and is converted in situ to dopamine via DOPA-decarboxylase, has been used to study dopamine distribution in the brain. [2] Both ^{11}C and ^{18}F labeled 5-fluoro-DOPA and 6-fluoro-DOPA were synthesised for this purpose. [5]

A DOPA molecule is presented in Fig. 2.1.

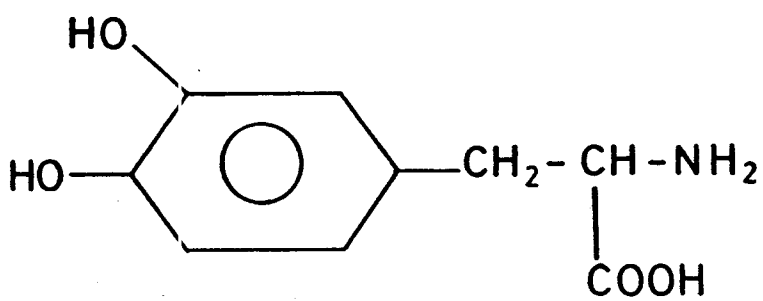

Fig. 2.1 DOPA.

Since fluorine does not naturally occur in L-DOPA, its use as a label represents a potential perturbation in the biological behaviour of the molecule. It was found that the substitution of fluorine for hydrogen on position 6 of the DOPA molecule results in the least alteration in the properties of the parent compound. [5]

The synthesis of ^{18}F-6-fluoro-DOPA by direct fluorination of DOPA with [^{18}F]F is the method of choice at McMaster Hospital eventhough the yield is low. [6]

Synthetic strategies were developed for labeling amino-acids in metabolically inert positions (2 and 3) via C and C-L-DOPA. [2, 6]

Other Labelled Tracers for PET.

The ^{15}O radiotracers are present in gaseous and liquid form. These tracers are used in the measurement of cerebral blood flow and oxygen utilization to determine the metabolic status of diseased tissue as in stroke and cerebral malignancy.

A number of compounds have been labelled in the search for the ideal tracer for measuring cerebral blood flow: ^{11}C-alcohols , ^{15}O tracers, etc. [2]

In vivo assessment of the metabolic status of tumors is an important problem. Here the tracers of glucose and oxygen metabolism play a major role. ^{11}C-putrecine has been developed to take advantage of the increase in polyamine metabolism associated with rapidly proliferating tissue. [6] Since the uptake in normal brain tissue is very low, a high contrast between tumour and normal brain is obtained in PET studies of human cerebral malignancy. [2] The development of tracers for the measurement of tissue proliferation has been of interest especially in view of their potential use to monitor response to chemotherapy.

The application of a β^+ emitter-labeled drugs and PET offers the possibility of correlating a drug's therapeutic efficiency with its regional concentration.

D. Radiation Dosimetry

The dose absorbed by a patient from decay of radionuclides is dependent on the energy and abundance of all ionizing radiation (photons, positrons, electrons) emitted by the radioactive atoms as well as the distribution and effective half-life of the radionuclide in the body. Careful calculations involve attenuation of Auger electrons, X-ray photons, internal conversion electrons as well as the γ ray photons and high energy electrons emitted as part of the primary decay event. For many of the radionuclides presently in use, it is possible to calculate doses for the whole body distribution.

The dose deposited by a radionuclide distributed in a particular organ is, of course, not the sum of all the energies released by the atoms because most of the energy is carried away by the γ photons we use to detect the presence of the radioactivity. In fact, for most radionuclides of interest only 1/2 to 1/3 of the energy is absorbed in the body. [7] Further, it should be realized that those organs which do not concentrate any isotope still receive some dose due to the energy deposited in the organs from photons that are emitted from contiguous tissues.

A recipe for dose calculations is [7]:

$$\text{Body dose (rad/mCi)} = \frac{k \times T_{eff}(\text{days}) \times [0.3 \times E_{\gamma}(\text{MeV}) + E_{\beta^+}(\text{MeV})]}{m(\text{Kg})} \qquad (2.2)$$

where: k = 71.2 is a conversion factor relating mCi, half-life expressed in days and energy in MeV, to dose in rads, T_{eff} is the effective half-life, E_{γ} = 0.511 MeV, E_{β^+} is the positron energy, m is body weight in kg. These calculations did not take in account Auger electrons, internal conversion electrons and X-rays.

Another way to estimate the absorbed dose is to evaluate tissue activity as a function of time, after administration of the radiotracer and then using MIRD (Medical Internal Radiation Dose) approach to compute organ and whole body doses.

For ^{11}C-DG and ^{18}F-FDG, the distribution of activity in various organs were determined in rats and dogs respectively. [8] This information allowed the biological half-life of DG in various organs to be calculated.

Radiation dosimetry calculations according to MIRD model were done on the basis of the following assumptions [8]:

- after an intravenous injection of 1 mCi of FDG, kidneys, lungs, liver, brain, heart, spleen, ovaries and bladder uniformly and instantaneously take up the amounts of activity determined by the tissue distribution at 60 min in dogs,
- the remainder of activity is instantaneously and uniformly distributed throughout the whole body,
- the effective clearance half-life is 1.83 h for all the organs.

The calculated absorbed radiation doses to these organs in humans are presented in Table 2.3. [8]

Table 2.3 Radiation Dosimetry for ^{18}F-FDG in Man.

Organ	Dose (mrad/mCi)
Whole body	43
Ovaries	63
Liver	67
Kidneys	77
Lungs	67
Brain	66
Heart	147
Spleen	185
Bladder	289

For the short-lived isotopes ^{15}O, ^{13}N and ^{11}C, internal organ and whole body doses tend to be small. To estimate radiation doses for the brain and bladder wall, human biodistribution data for ^{18}F-FDG were used.

Table 2.4 summarizes the radiation doses for various PET studies. [9]

Table 2.4 Radiation Doses for Various Positron Emission Tomography Studies.

Radiotracer	Typical dose (mCi)	Critical organs	Critical organs dose (mrad/mCi)	Whole body dose (mrad/mCi)
^{18}F - FDG*	10	Bladder	440	39
$H_2{}^{15}O$*	50	Blood, Kidneys, Liver, Lungs	10	1.6
$C^{15}O$**	50	Spleen, Lung, Intestine	15, 11, 14	1.6
$CO^{15}O$**	50	Lung	4.9	1.6
^{11}CO**	20	Spleen, Lung, Intestine	50 - 60	19
^{82}Rb*	50	Heart, Kidneys	13, 19	1.6
^{15}OO**	50	Tracheal mucosa, Lungs, Blood	20 7.5, 10	1.6

*bolus injection, **bolus inhalation

The short half-lives of these radionuclides used in PET offer a great advantage over these of typical radionuclides used in nuclear medicine, because even an initially very active tracer decays away quickly. In addition, almost all positron emitters are decaying into stable isotopes. These characteristics makes it possible to administer a high activity tracer and then to measure the compound distribution by PET while the counting rates are still high, in order to obtain images of good statistical quality.

An important consideration when using short-lived isotopes is the dose to technical personnel. For administration by injection, the hand dose received by the technician can be significant since 511 KeV photons cannot be easily shielded. Measurements using finger ring dosimeters give values of 10-20 mrads to both hands, for a single administration of ^{15}O or ^{18}F labeled tracers. [9]

For inhalation studies, it is important to prevent leakage of the radioactive gas to avoid hazard to personnel.

2.1.2 The electronic coincidence collimation.

Positron Emission Tomography (PET) is a nuclear medicine imaging modality which yields transverse tomographic images of the distribution of positron-emitting radionuclides administered to the subject under study. In PET, as in all nuclear medicine techniques, the image-forming variable is the distribution of the radionuclide. The data required for the generation of the image is supplied by the detection of the radiation emitted as a result of the annihilation of positrons in matter.

A. Positron Annihilation Radiation.

The positron is the anti-particle of the electron. Certain radionuclides which contain an excess of protons with respect to a stable configuration of nucleons, decay by the emission of a positron and electron neutrino:

$$Z \longrightarrow (Z - 1) + \beta^{+} + \nu_{e}$$

The positron energy spectrum is smooth and approximately bell shaped with a maximum positron energy, the *end point*. The end points of the energy spectrum vary from some tenth of a MeV to several MeV from one nucleus to another one.

After its emission by a radionuclide, the positron looses its energy in a manner similar to that of a negatively charged electron.

Table 2.5 presents the most common positron emitting isotopes used in PET, their end point energies and the range in water. [10]

Table 2.5 The isotope of interest in PET.

Isotope	E_{β^+} (MeV)	Effective range* (FWHM mm)
^{11}C	Ø.97	2.Ø6
^{13}N	1.19	3.Ø
^{15}O	1.7Ø	4.5
^{18}F	Ø.635	1.4
^{68}Ga	1.88	5.4
^{75}Br	1.7; 1.1; Ø.65	
^{82}Rb	3.15	13.8

*"Effective" FWHM of the intrinsic line spread function is defined such that 75% of all annihilations occur within that diameter.

Usually, after the positron loses most of its kinetic energy, it interacts (as a form of antimatter) with a negatively charged electron and for a short period of time the two particles form an atom called "positronium". Positronium has a very brief existence and the two particles undergo the process called annihilation, in which their masses are converted predominately into two photons, each carrying an energy of Ø.511 MeV corresponding to the rest mass of each one of the annihilated particles, and traveling nearly colinearly in opposite directions, in order to conserve linear momentum, (Fig. 2.2).

A 511 KeV photon will travel an average of 1Ø cm water before interacting. The highest probability of interaction in water, at this energy is by Compton effect. This process reduces its energy and randomly changes its direction. Since the human head or chest is approximately two interaction length thick, the probability that annihilation photons leave the body unscattered is only about 2Ø%.

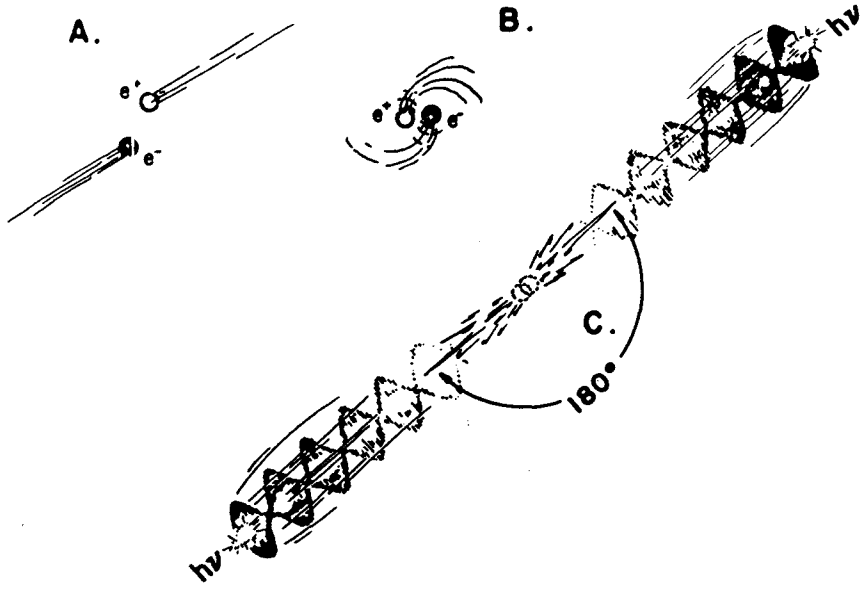

Fig. 2.2 *Diagram illustrating the annihilation of a positron in matter as a result of an interaction with a negatively charged electron. The masses of the two particles are annihilated and the energy thus made available is converted into two photons, each with an energy of* 511 KeV, *traveling nearly colinearly.*

B. The electronic coincidence collimation.

The colinearity of the travel of the two annihilation photons in opposite directions permits the collimation of this radiation by electronic means.

Two radiation detectors sensitive to the annihilation photons are placed on opposite sides of the object containing the positron emitter (Fig. 2.3), and connected to an electronic circuit operating in coincidence. Under these circumstances, the annihilation process will be localized in space to a volume circumscribed by straight lines joining the sensitive areas of the two detector system. Annihilation events occurring outside this volume will not be recorded.

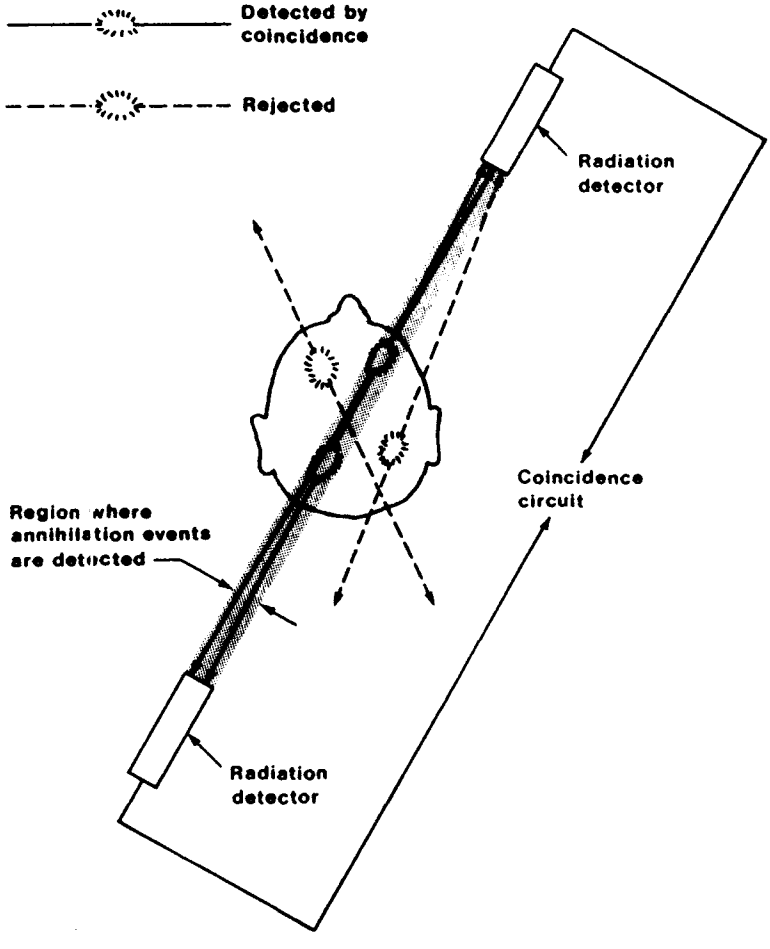

Fig. 2.3 *Diagram of the electronic collimation of the annihilation radiation by means of two detectors operated in the coincidence mode.*

The isocounts curves for the detection of the annihilation radiation for two detectors operated in coincidence exhibits a region where the cross section and the shape of the isocounts curves do not vary appreciably (Fig. 2.4). The width of this region is approximately equal to one half the diameter of the detectors used [11, 12], (Fig. 2.5).

The existence of this region of uniform response is particularly useful in PET. In contrast, the resolution of detectors with a typical absorbing collimator used for single photon detection varies substantially with the distance between the detector and the source.

Another important feature of coincident detection of the annihilation radiation is that it permits the detection of radionuclides in absorbing medium with sensivity independent of depth in the absorber. Indeed, for a source of positrons immersed in an absorbing medium, the two 511 KeV annihilation photons must always cross almost the same total path length to be detected in coincidence. The probability of detection is:

$$P \approx e^{\mu x_1} \quad e^{\mu x_2} = e^{\mu(x_1 + x_2)} = e^{\mu x} \qquad (2.3)$$

where μ is the linear attenuation coefficient and $x_1 + x_2 = x$ is the total thickness of the absorber.

This is not the case for single-photon detection where sensivity decreases with depth due to the increasing path length through the object and the corresponding increasing attenuation.

The electronic collimation permits a higher overall radiation detection efficiency when multiple detector system are employed.

This properties of the coincident detection of the annihilation radiation are particularly valuable in the tomographic reconstruction of the distribution of a source of positron-emitting radionuclides in vivo for PET imaging.

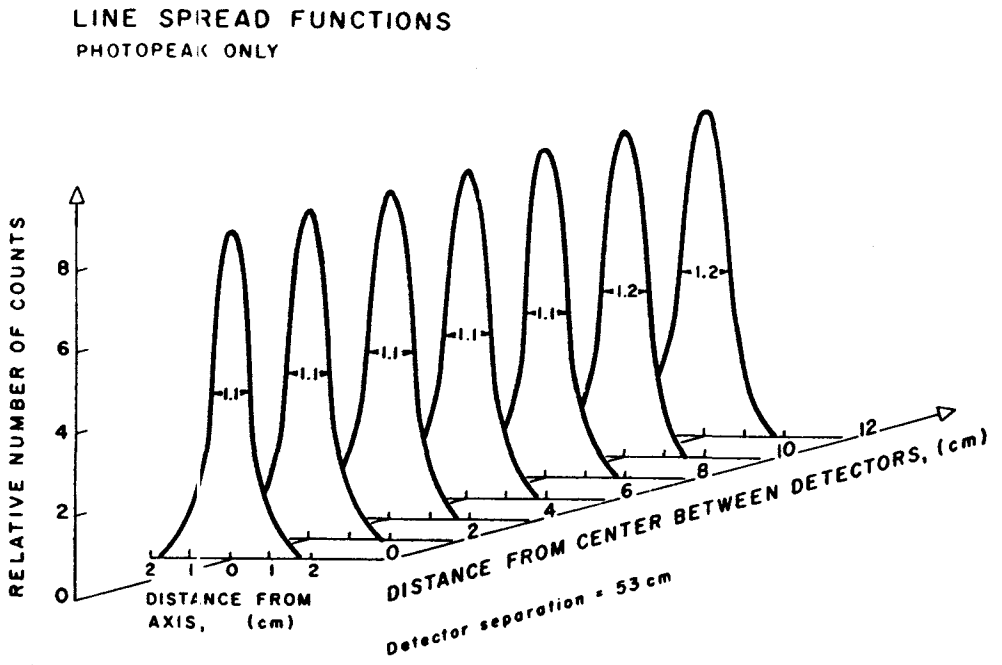

Fig. 2.4 *Isocount curves showing the uniformity of depth response for the electronic collimation of the annihilation radiation.*

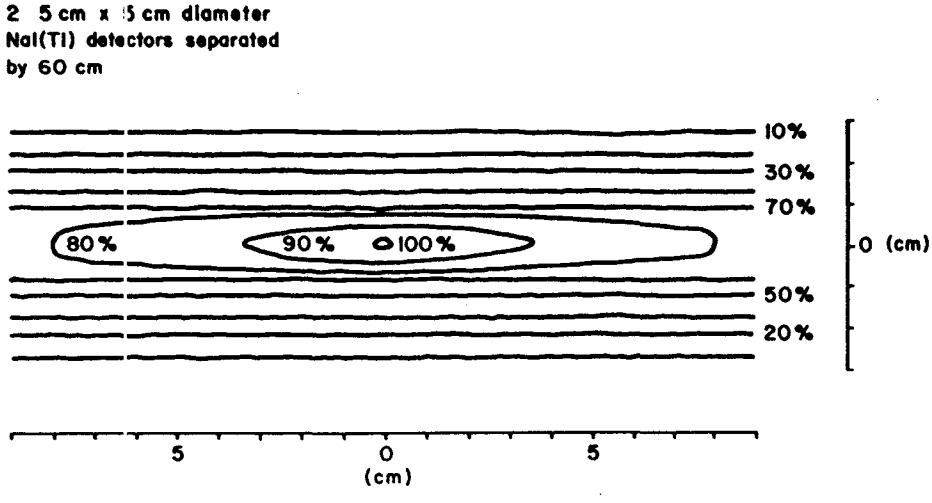

Fig. 2.5 *Isocount curves illustrating the relatively uniform field of view obtained with two scintillation detectors operated in the coincidence mode, for the detection of the annihilation radiation.*

2.2 Design Concepts of a Positron Emission Tomograph.

The goal of all tomograph design is the accurate and rapid measurement of tracer concentration in defined volume elements in an organ such as the brain or the heart.

A Positron Emission Tomograph embodies a gantry with suitable electronic circuits designed to acquire the projection data necessary for reconstruction of an image, a computer interfaced with the data acquisition system, and peripherals, the purpose of which is to store the acquired data, to reconstruct the image displayed and provide interactive capabilities for quantitative studies (Fig. 2.6). [11, 12]

2.2.1 The Gantry.

The essential purpose of the gantry of a PET device is to support the radiation detectors. The configuration of the gantry was designed to achieve proper sampling with the highest sensivity. These qualities can be obtained with a circular ring of photon detectors with side shielding and associated electronics.

The first PET gantries were provided with a detection system capable of a translational and rotational motion to achieve proper linear and angular sampling, (Fig. 2.7). Later, PET devices were designed with a sufficiently large number of detectors, so as to obviate the need of any motion.

Many units allow a certain amount of angulation of the scanning plane relative to the horizontal axes or table bed (Fig. 2.8).

Modern systems embody multislice capabilities through the use of detectors placed in different planes and through the utilization of coincidence across planes.

The side shielding prevents annihilation photons outside the plane of interest from entering the detectors. For a fixed overall diameter, a larger shielding depth reduces the accidental and scattered event rate, but reduces the diameter of the patient port.

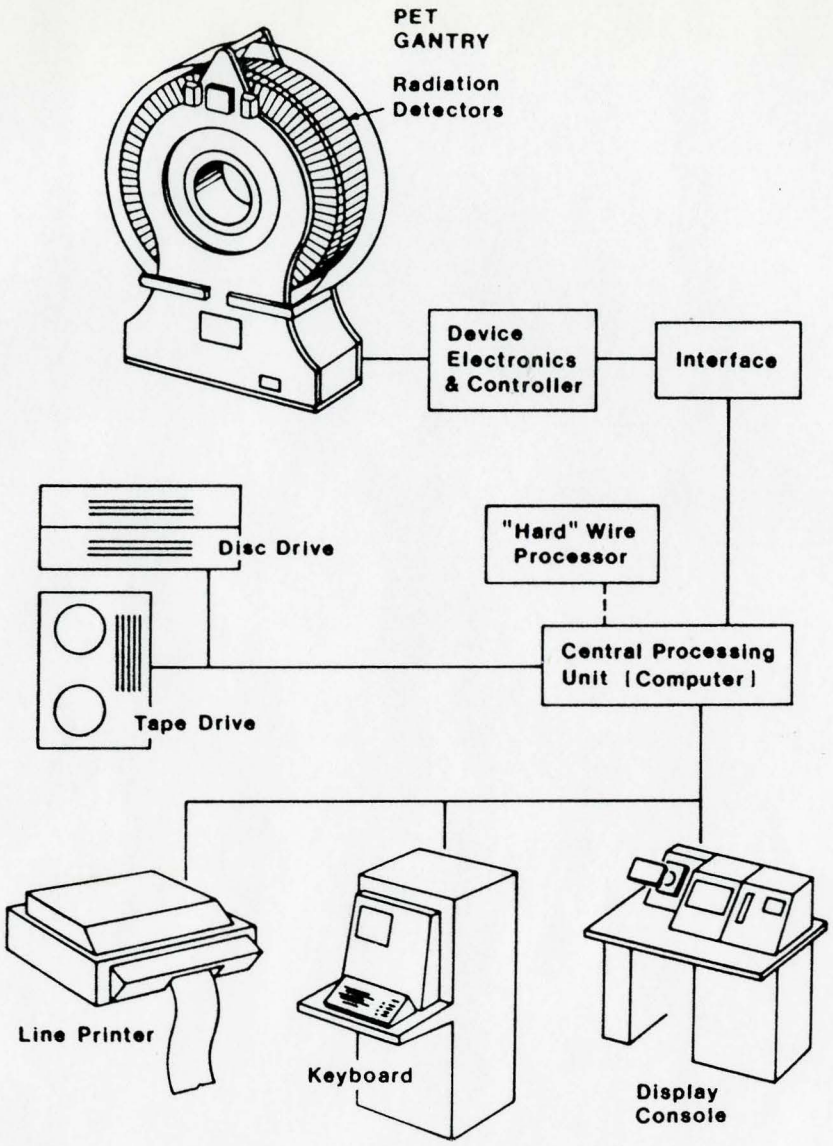

Fig. 2.6 *Block diagram of the components of a typical* PET *system.*

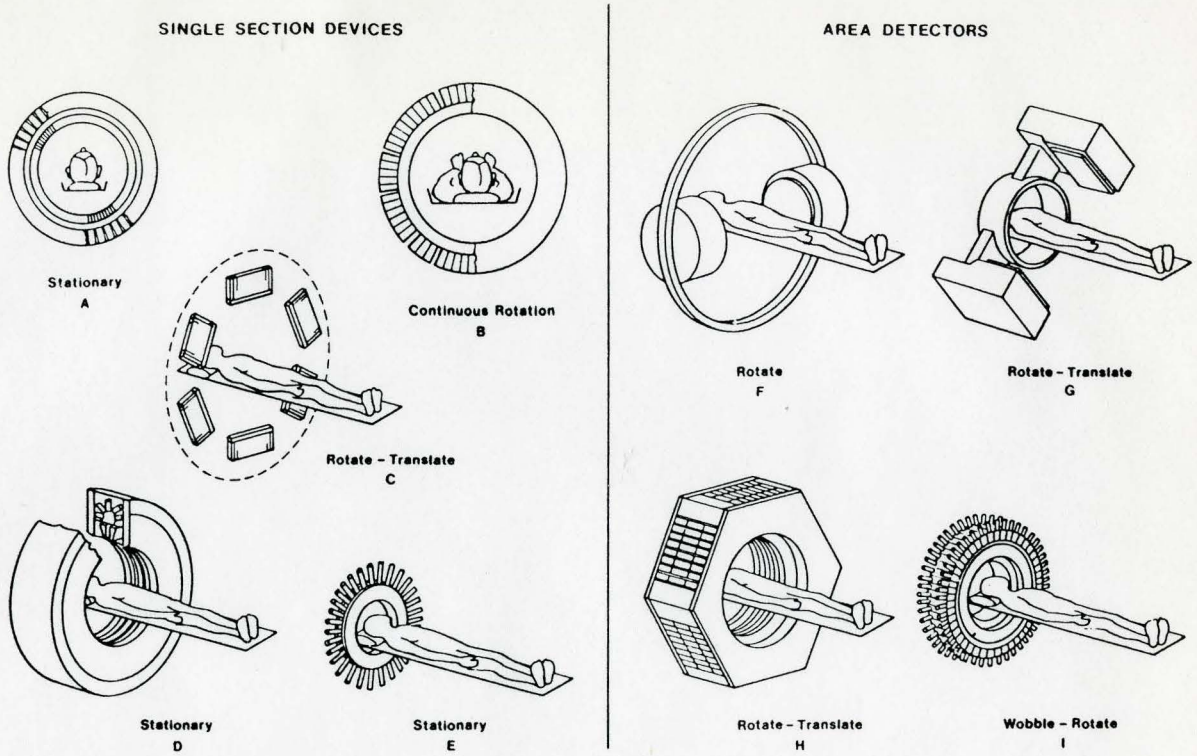

Fig. 2.7 *Diagrams of various configurations which have been used for* PET *gantries.*

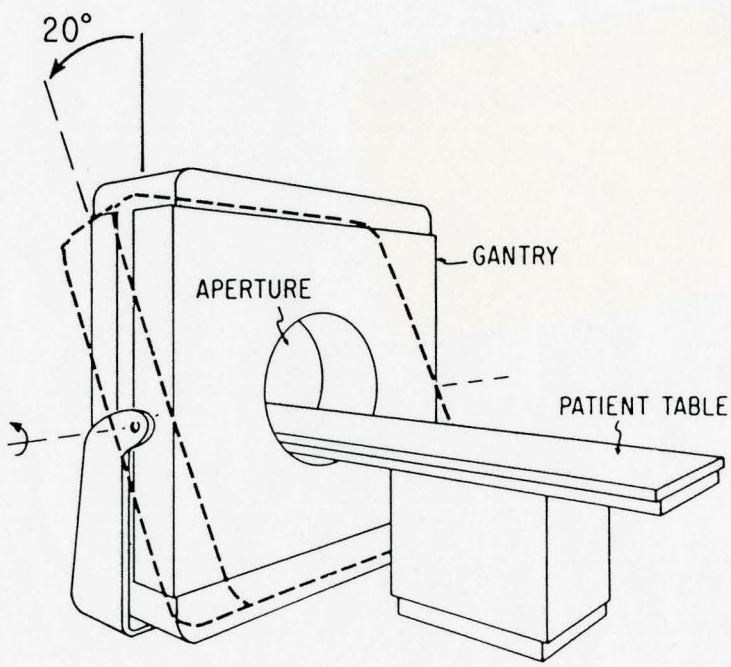

Fig. 2.8 *The capability of tilting the gantry to examine oblique cross-sections.*

2.2.2 The Detection System

A. Detectors for PET

Another distinguishing feature of PET is the detector system.

PET images are obtained through the detection in coincidence of the annihilation radiation. Therefore, the most important physical characteristics of radiation detectors for PET applications are:

- high efficiency for the detection of annihilation photons (511 KeV),
- short coincidence resolving time,
- ability to provide high spatial resolution,
- stability,
- reliability
- low cost.

Various radiation detectors have been proposed, tested and used for PET. They include scintillation detectors from different types of crystals, multiwire proportional counters and various types of solid state detectors.

Initially, NaI(Tl) was the detector material used because of its availability and low price. However, its moderate stopping power for 511 KeV gamma-rays [10], made it less than ideal (Table 2.6). [13, 14]

A detector material, bismuth germanate (BGO) was introduced which had three times the stopping power as NaI(Tl), the highest density and the highest effective atomic number. In addition, BGO is nonhygroscopic, can be handled easily and in conjunction with stopping power, allows designs with small packed crystals which give both high efficiency and high spatial resolution.

In contrast to BGO, CsF has good timing properties but stopping power similar to NaI(Tl). BaF_2 has replaced CsF for time of flight positron instrumentation being the highest speed inorganic scintillator known. BaF_2 is not hygroscopic and the crystals do not have to be sealed in bulky cans, which improves the detection efficiency.

Table 2.6 Properties of Scintillation Materials for PET.

Material	Sodium iodide NaI(Tl)	Bismuth* germanate $Bi_4Ge_3O_{12}$	Cesium fluoride CsF	Barium fluoride BaF_2	Gadolinium** ortho-silicate $Gd_2SiO_5(Ce)$
Density (g/cm^3)	3.67	7.13	4.64	4.89	6.71
Effective atomic number	50	72	52	52	48
Linear attenuation coefficient (cm^{-1})	0.34	0.92	0.44	0.46	
Emission λ (nm)	410	480	390	310;225	430
Index of refraction	1.85	2.15	1.48	1.6;1.5	1.9
Photoelectric yield	3000	400	200	800;200	600
Scintillation decay time (nsec)	230	300	2.5	620;0.8	60
Time resolution (FWHM nsec)	1.5	0.2		5	
Hygroscopic	Yes	No	Very	No	No

Interaction probabilities for 511 KeV photons (cm^{-1})

Photoelectric	0.06	0.393		0.085	
Compton	0.268	0.51		0.353	
Total	0.328	0.903		0.438	

*BGO; **GSO

The new material, GSO [14] has speed advantages over BGO but a lower detection efficiency.

Taking in consideration the large number of detectors used in PET, the low cost is an important advantage in choosing the detector's material.

There is the possibility of utilizing multiwire proportional counters with a wire gird system that enables the counter to localize in two dimensions the position of an ionizing event. The advantages of such a detector for PET include the very high spatial resolution, the relatively low cost. The main disadvantage of multiwire proportional counters for PET applications lies in their relatively poor efficiency in detecting energetic photons. Another disadvantage of these detectors is that they exhibit a relatively long coincidence resolving time, typically several tens of nanoseconds.

The purpose of the scintillation crystal is to stop the photon and convert its energy into a brief scintillation of visible light. The annihilation photons can interact in the scintillator in two ways:

- by photoelectric effect, whereby the entire 511 KeV is given to an electron,
- by Compton scattering, where only a portion of the full energy is given to a recoil electron, and the initial photon is reduced in energy and scattered into a random angle.

A successful event requires that both annihilation photons pass the pulse height requirements in the opposing detectors. The *detection efficiency* is the fraction of annihilation photons reaching the scintillator that produce an acceptable pulse.

The recoil electrons and the photoelectrons produce ionizations and excited atomic electrons in the scintillation crystal. Some of the excited electrons return to their ground states by the emission of scintillation light. The *luminous efficiency* (number of scintillation photons per KeV loss) and the speed of emission vary from crystal to crystal (Table 2.6).

Light in the scintillator can be trapped by total internal reflection, absorbed by internal impurities and imperfections, absorbed by external reflectors, or collected by the photodetector (photomultiplier). The light *collection efficiency* represents the fraction of light reaching the photodetector.

B. The photomultiplier.

The photomultiplier (photodetector) converts collected incident light photons (optical energy) into a useful electric pulse (electrical energy). The *quantum efficiency* is defined as the probability that an incident photon will produce a photoelectron in the photodetector. (Four different efficiencies appear above: detection efficiency, luminous efficiency, light collection efficiency and quantum efficiency).

Two different kinds of photodetectors can be used in PET designs: photomultiplier tubes and photodiodes.

The photomultiplier tube (Fig. 2.9) is a vacuum tube containing a photocatode and a series of dynodes. As light scintillation photons enter the tube, they immediately encounter the photocatode, a thin film on the inside face of the tube, usually consisting of an alloy of Cesium (Cs) and Antimony (Sb) in which the outer orbital electrons are loosely bound. Some fraction of the light photons interacts with electrons in the photocatode causing them to be ejected from their orbits as photoelectrons. As each photoelectron strikes the dynode (charged at +300 V) it dislodges several secondary electrons from the dynode surface which is coated with a material similar to that of the photocatode. These secondary electrons are in turn accelerated toward the second dynode which is about 100 V more positive than the first dynode, and additional secondary electrons are produced. This process continues over a total of 6-14 dynode stages. The result is an overall gain from 10^5 to 10^8 electrons produced per photoelectron.

The photodiodes are solid state analogues of photomultiplier tubes. A photodiode converts the light signal from a scintillation crystal into an electrical signal.

In solid state photodetectors the electrons are multiplied in high field regions within the photodiode material. The band structure of the complete detector unbiased and under bias is shown in Fig. 2.10. Each stage of the band diagram of the grade gap multilayer material, is linearly graded in composition from a low (E_{g_1}) to a high (E_{g_2}) band-gap.

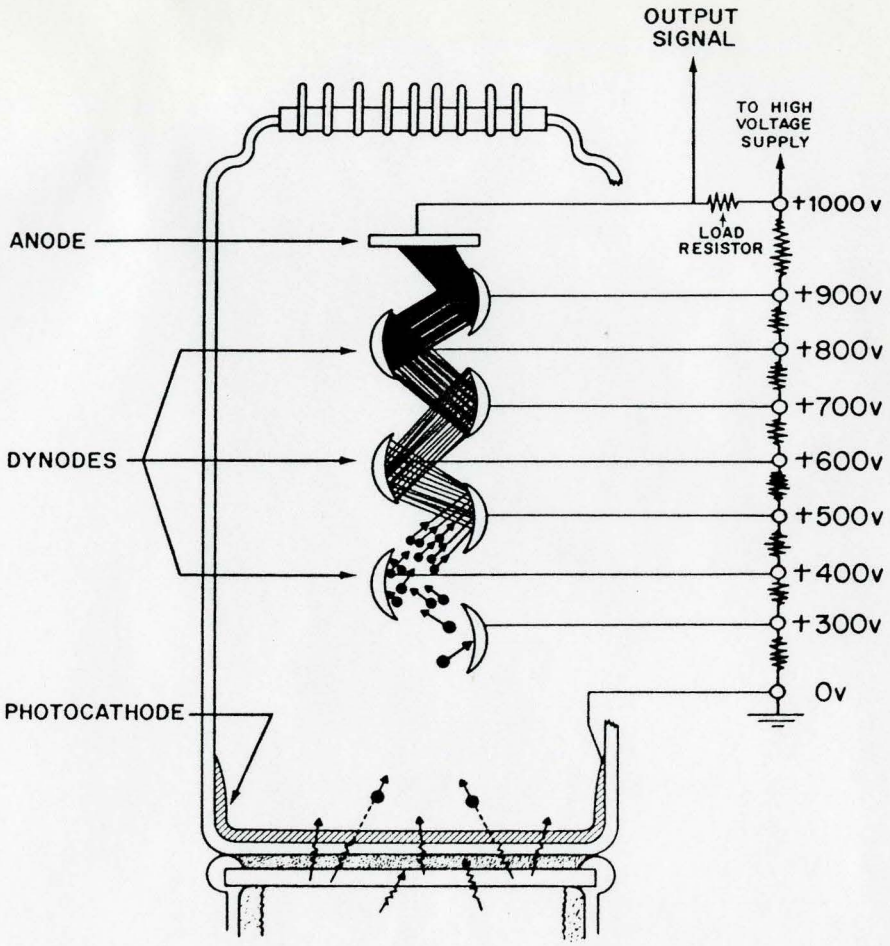

Fig. 2.9 *Operation of a photomultiplier tube.*

The materials are chosen for a conduction band discontinuity comparable to or greater than the electron ionization energy (E_i) in the low gap material following the step.

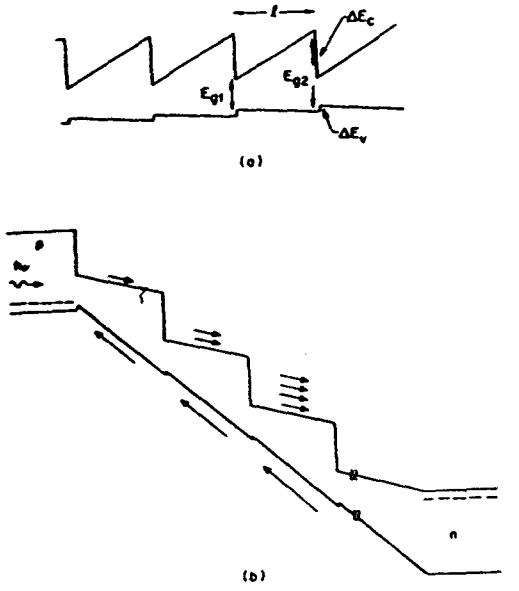

Fig. 2.10 *Band diagram of:*
a) *unbiased graded multilayer region, and* b) *the complete staircase detector under bias. The arrows in the valence band indicate that holes do not ionize.*

An electron generated near p^+ contact cannot ionize in the graded region before the conduction band step because the effective field is too low. At the step however, the electron ionizes since $\Delta E_c > E_i$ and the process is repeated at every stage. These steps correspond to the dynodes of a phototube.

Solid state photodetectors such as Si, GaAs and HgI_2 have quantum efficiencies in excess of 60% higher than that of photomultiplier tubes. [15] In addition, solid state devices can be made much smaller than phototubes and in a variety of shapes which represents big advantages for the tomograph design. The problem is that, at present time, these devices are considerably more expensive than glass phototubes and have poorer timing resolution. [16]

2.2.3 The electronic processing unit.

The functions of the electronic processing unit are to amplify and shape the voltage pulse at the output of the photodetectors, to determine whether or not the pulse represents an acceptable photon, and if it is acceptable to record it.

The voltage pulse at the output of the photomultiplier has an amplitude that is proportional to the number of electrons leaving the photomultiplier tube and hence to the energy that original photon (γ-ray) transfers to the crystal. Since the pulse amplitude is too small to be measured accurately, a preamplifier connected to the phototube output may be used to make the signal large enough to pass through the cable.

A pulse shaping circuit is inserted before the main amplifier to cut off pulse tails abruptly.

The next step is the pulse-height analyzer which makes the distinction between events on the basis of pulse amplitude. [16] The pulse height analyzer consist of two discriminators and an anticoincidence circuit (Fig. 2.11). The discriminators operate in tandem. The lower level discriminator is set to minimum height of an acceptable pulse, whereas the upper level discriminator is set to the maximum acceptable height. Signals from both discriminators are fed into the anticoincidence circuit in which signals produced by the latter discriminator serve to block passage of signals produced by the former one. Thus, the only pulses accepted are those with heights falling between the sittings of the two discriminators. The setting of the lower level discriminator is referred to as E setting, the lower level baseline, or threshold, and the separation between the lower and upper level discriminator settings is referred to as the window or ΔE setting.

The accepted signals from discriminators are introduced in a coincidence system which is designed to accept twin photons related to the same annihilation event. The pulse is recorded only if the two signals arrive in a period of time called the coincidence resolving time. Typically, in PET devices this coincidence resolving time covers a range from less than 15 nsec to tens of nanoseconds. [12]

The detected events are recorded by incrementing appropriate locations in a computer memory.

An overall block diagram of the electronic system of a multiring positron system for emission tomography of the brain is presented in Fig. 2.12. [17]

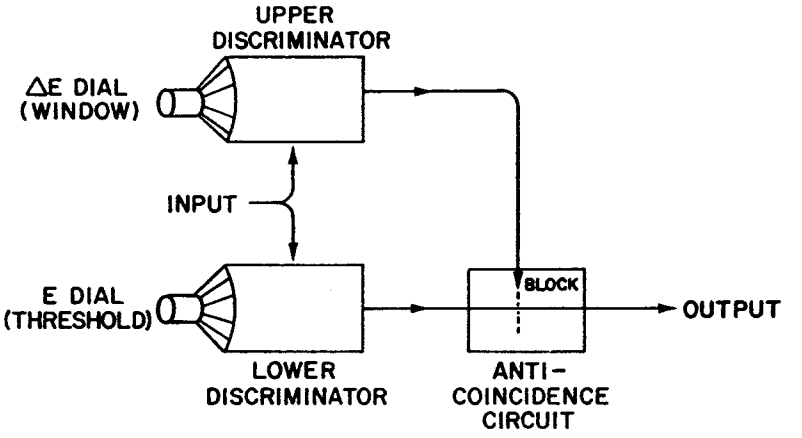

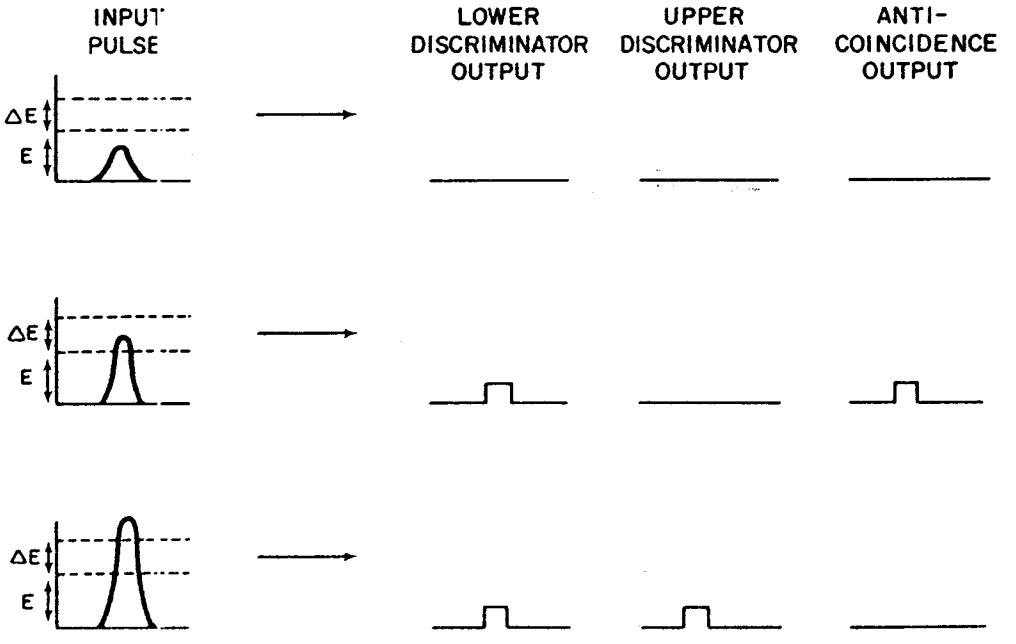

Fig. 2.11 *Pulse height analyzer. E is the lower level baseline and ΔE is the window.*

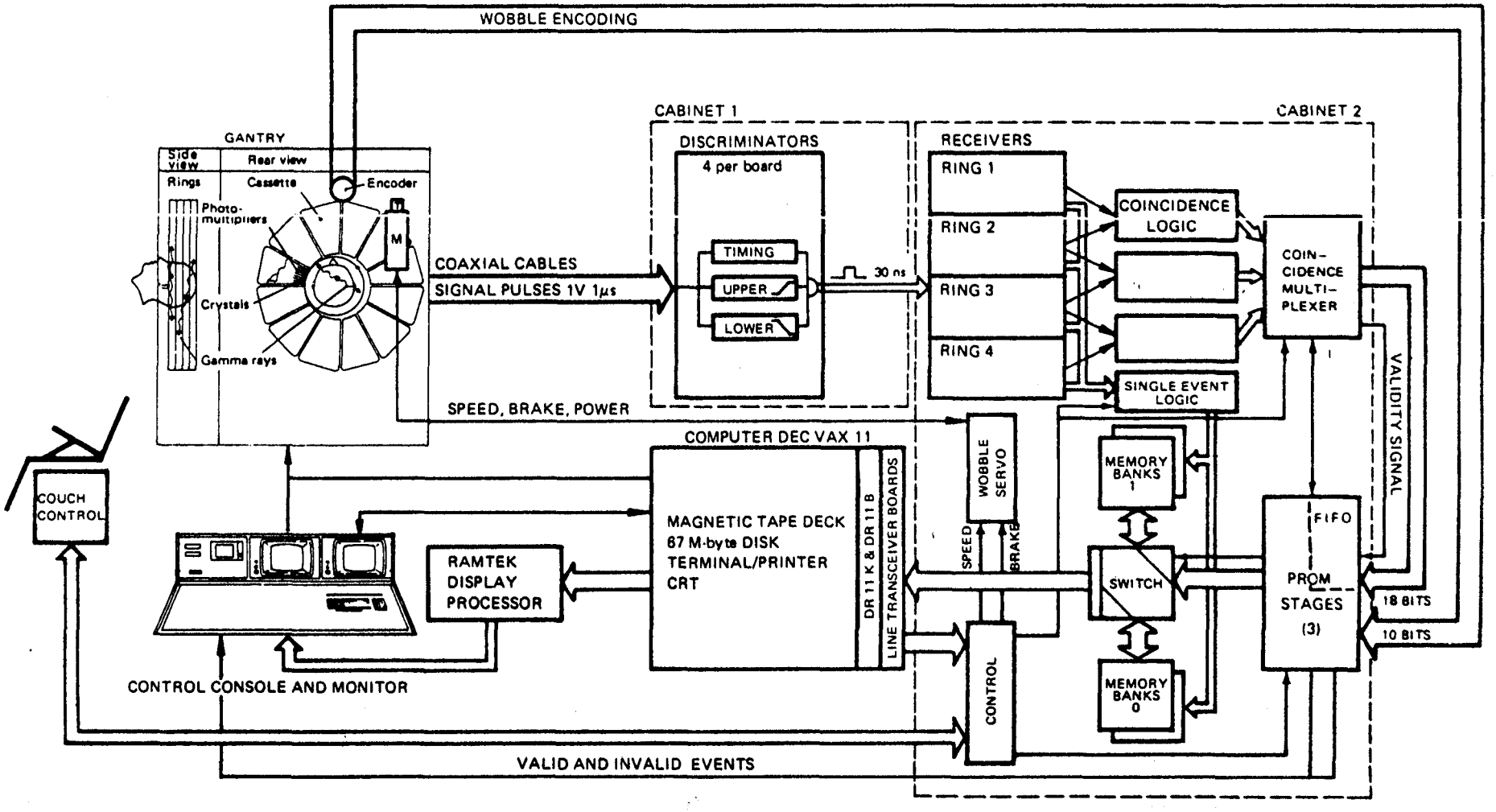

Fig. 2.12 *Overall block diagram of the electronic system associated to a multiring tomograph.*

3. THE TOMOGRAPHIC RECONSTRUCTION FROM PROJECTIONS.

Computed tomography is the technique of computer assisted image reconstruction of anatomical cross-sections.

Every point of an object within a section to be reconstructed can be defined by its (x,y) coordinates in a Cartesian system (Fig. 3.1). The contribution of every point to a detected signal is given by the density function f(x,y). For X-ray computed tomography, f(x,y) represents the linear attenuation coefficient $\mu(x,y)$. For radioisotope imaging, in particular emission computed tomography, f(x,y) is proportional to the density of emission of radionuclides.

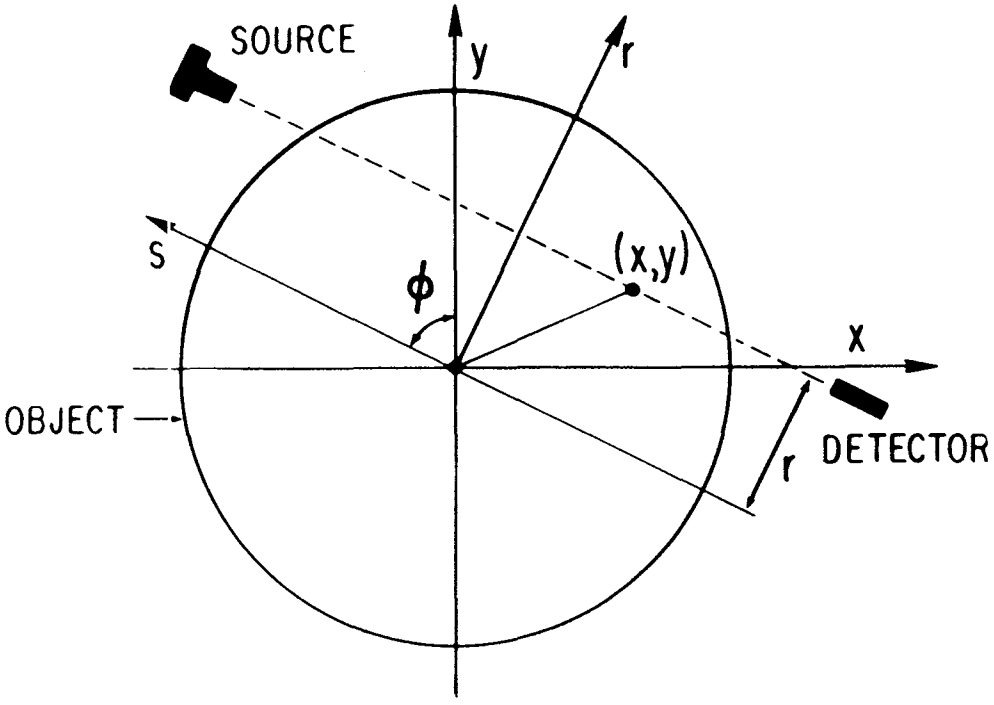

Fig. 3.1 *Coordinate systems. A point is designed by its coordinates (x,y) in a fixed Cartesian coordinate system. A ray, as indicated by a dashed line, is described by its angle ϕ, with respect to the y-axis and its distance, r, from the origin. The coordinate s indicate the distance along the ray.*

Each individual ray (a straight line path through an object) is best specified in terms of its own coordinate (r,ϕ), (Fig. 3.1). The ray coordinate system is superimposed over the object's Cartesian system so that ϕ is the angle of the ray with respect to the y axis, and r is its distance from the origin. The s coordinate illustrated in Fig. 3.1 represents the distance along the ray.

The x-ray coordinate system may be related to the object Cartesian coordinate system by:

$$r = x \cos \phi + y \sin \phi \qquad (3.1)$$

The integral of $f(x,y)$ along a ray (r,ϕ) is called the ray-sum p:

$$p(r,\phi) = \int f(x,y)\, ds \qquad (3.2)$$

The mathematical problem in image reconstruction is to find the solution of equation (3.2), given a complete set of ray-sums (projection lines) $p(r,\phi)$.

In computed tomography, data are registered per projection line, at discrete angle, which means that in practice, $f(x,y)$ is calculated for a finite number of discrete points, from a limited number of projections.

If reconstruction is limited to a circular region or domain of diameter d, and the points are regularly separated by a distance w, there are $n = d/w$ points along the diameter. (Fig. 3.2). The section may be divided squares, each of dimension w. The individual square are picture elements (pixels) for reconstruction. The value of a line integral $p(r,\phi)$ is assigned to all pixels that fall on the path along which that line integral was obtained.

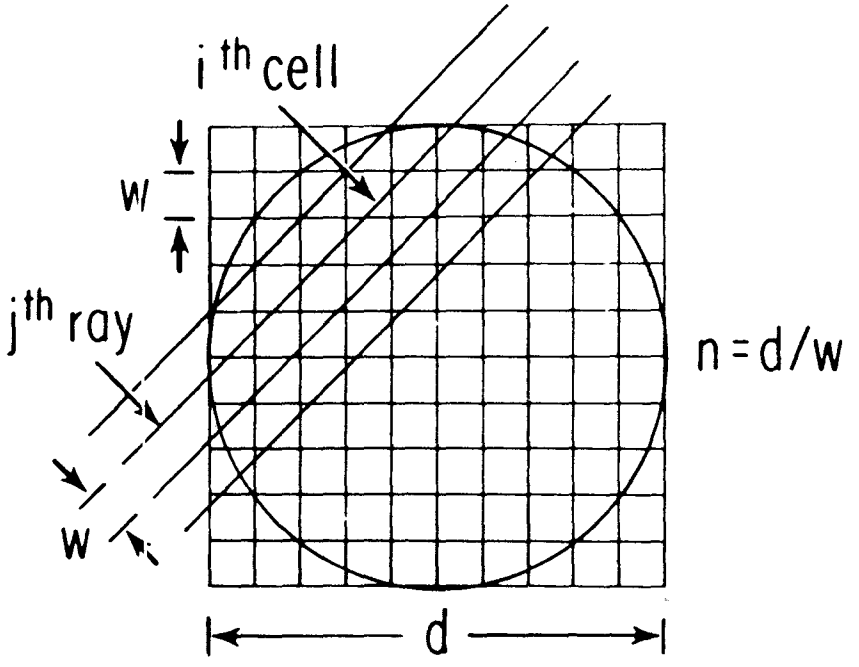

Fig. 3.2 *A diagram of the cellular array used in reconstruction.*

Several conceptually distinct methods of image reconstruction have been developed, characterized by different mathematical theories and computational techniques. Each different approach is referred to as an algorithm, which may be regarded as a mathematical recipe for image reconstruction.

The principal methods of analyzing the projection data and synthesis of the reconstructed image, involve:

1. back-projection or summation
2. iteration,
3. analytic methods.

3.1 Simple back-projection method.

Back-projection, also referred to as the summation method, is the simplest method of image reconstruction.

In this technique, the core of tissue through which a ray has passed is assumed to be homogeneous. The ray sum is then projected back into the core of tissue through which the ray passed, where it is equally distributed throughout all elements in the path of the ray. This is illustrated in Fig. 3.3 A, where a single dense point is taken as the only object in the field of view to be reconstructed. In this example the density function represents the linear attenuation coefficient.

For a single ray, the dense point appears to be localized with an equal probability within a strip within the slice in the reconstructed image. Following an angular rotation, this is done for multiple projections (Fig. 3.3 B) and each time a new back projection is formed.

Finally, the back projections are summed giving rise to a starlike image (Fig. 3.3 C). The region of highest density corresponds to the location of the dense point. However, spokes appear to radiate from the region of highest density to the periphery.

Mathematically, the relative reconstructed density, f(x,y) for any particular image point is the sum of all ray-sums passing through it. This is described by:

$$\hat{f}(x,y) = \sum_{j=1}^{m} p(r_j,\phi_j)\ \Delta\phi \qquad (3.3)$$

where ϕ_j is the j-th projection angle, $\Delta\phi$ is the angular distance between projections , and the summation is performed over all m projections. The symbol $\hat{f}$ denotes the relative value of the density function, not its absolute or true value.

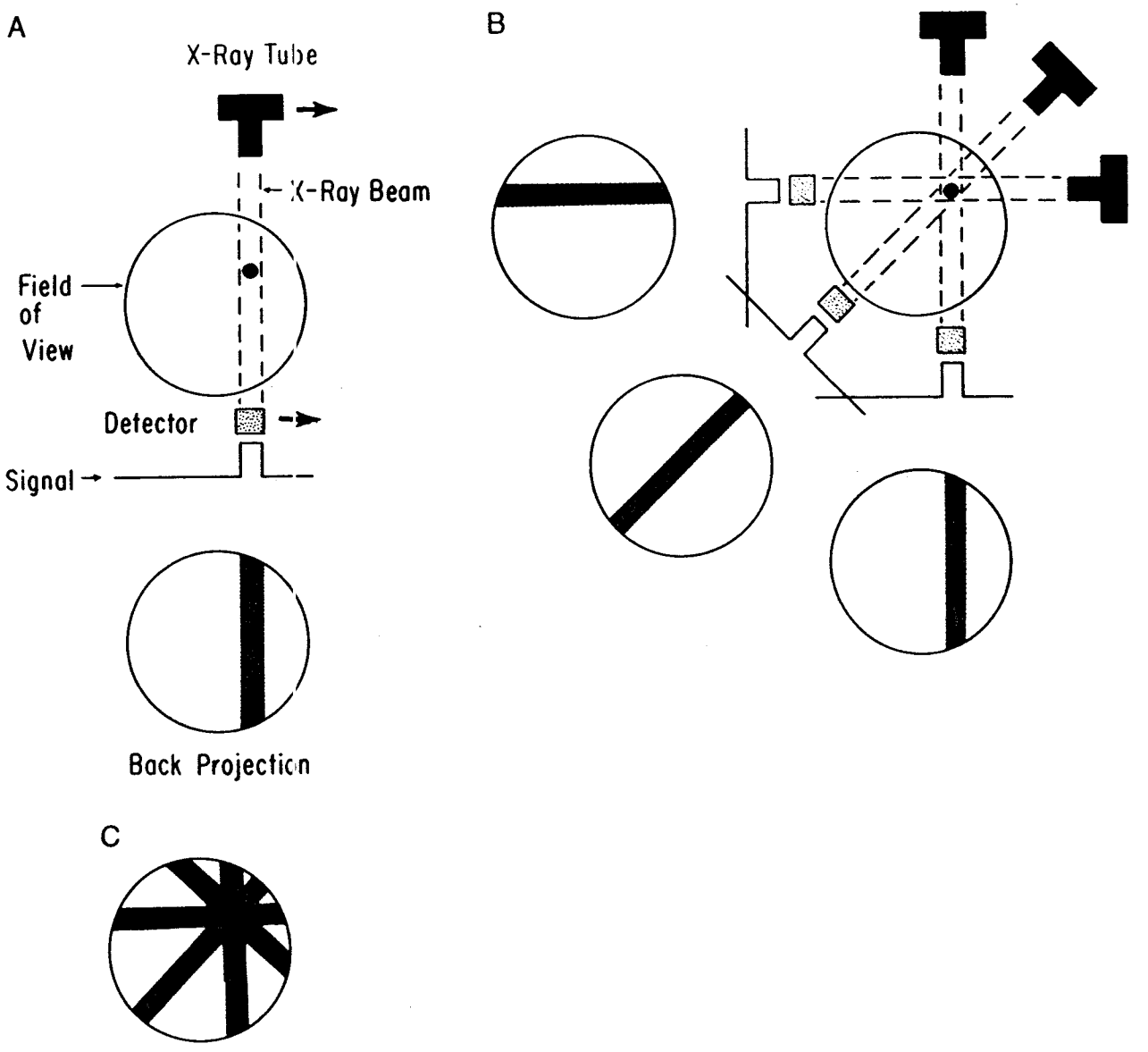

Fig. 3.3 *Simple back-projection method.*

A) *The ray sum obtained from a single dense object is back-projected.*

B) *Different projections are performed.*

C) *The individual back-projections are summed.*

Using equation (3.1):

$$\hat{f}(x,y) = \sum_{j=1}^{n} p(x \cos \phi_j + y \sin \phi_j, \phi_j) \Delta\phi \qquad (3.4)$$

The factor $(x \cos \phi_j + y \sin \phi_j)$ selects only those rays passing through the point (x,y) so that the back projected value of $\hat{f}(x,y)$ at each point is simply the sum of all ray-sums passing through the point. This is why back projection is also called the summation method.

In this method, the point has been imaged as a star. Any structure can be taken as a collection of points of varying density. The process of back-projection and summation leads to each individual point being reconstructed as a starlike image. The presence of these unwanted spokes associated with each reconstructed image point results in blurring of the composite synthesized image. Thus, there is a background density which exist as noise, generated by the fact that each ray-sum is back-projected to all points along the ray. This effect is additive and reduces the contrast.

A modified form of this technique, filtered back-projection, is presently the most widely used analytical algorithm.

3.2 Iterative methods.

The iterative techniques are based on the principle of successive approximations. An arbitrary set of values for the density functions of an initial image is assumed for a first approximation, and several corrections are made until the calculated ray-sums or projections from the reconstructed image are in agreement with the measured values.

The contribution of the i-th cell to the j-th ray (Fig. 3.2) is the weighing factor w_{ij}. Therefore, eq. (3.2) becomes:

$$p_j = \sum_{i=1}^{N} w_{ij} f_i \qquad (3.5)$$

where p_j is the j-th ray sum and f_i is the density function. Most of the weighing factors in eq. (3.5) are zero, since only a small number of cells contribute to a particular ray.

The procedure of correction in this method is applied to the initial arbitrary set of values for the density function. The ray-sums are calculated and compared to the measured values. The density of each cell within a ray is modified until a satisfactory agreement with the experimental data is reached. The process is described by:

$$f_i^t = f_i^{t-1} + \sum_{j=1}^{M} \Delta f_{ij}^t \qquad (3.6)$$

where f_i^{t-1} is the i-th coefficient before the iteration, f_i^t is the coefficient after iteration and Δf_{ij}^t is the correction applied to the i-th cell from the j-th ray.

The difference between this method and that of the simple back-projection is that the quantitaties being back-projected are correction terms derived from the projection, not the projections themselves, and these corrections are added to the previous values. If the initial set of density functions is made equal 0, that is, a blank screen, the first iteration is identical to the simple back-projection.

The iterative methods are classified by the sequence in which corrections are made and incorporated into an iteration.

In *simultaneous correction*, all the projections for the entire matrix are calculated at the beginning of each iteration, and corrections are made simultaneously for each element or pixel in the matrix at the end of the iteration. Each element is corrected once and only once during each iteration.

This approach unfortunately leads to overcorrection, since each element in the matrix is recorrected for every ray passing through it, so that the successive iterations actually oscillate around the correct solution. Thus, there may be a lack of convergence to a final solution.

In the *ray-by-ray correction*, a ray sum is calculated at the beginning of each iteration and corrections are made for each element or point in the ray. This is done sequentially for each ray in each projection, always incorporating corrections made in previous rays into each new calculation. After this has been done for all rays in all projections in that iteration, a new iteration begins. The process will be repeated until the calculated and the measured ray-sums for all rays were equal or until the difference were sufficiently small that no further calculations were needed.

In *point-by-point correction*, each iteration initially corrects a single pixel or element for all rays passing through it. The process is repeated sequentially for all pixels or elements in the matrix, but with the incorporation of the successive corrections made during the iteration.

Iterative techniques are well established in the solution of multiple simultaneous equations. The details of programming computers to solve simultaneous equations by iterations are not difficult. Finally quite adequate images can frequently be obtained with this approach.

Iterative methods have three significant limitations:

- the relatively long time required to perform the iterations,
- the possible lack of convergence of the calculated results to the true values of the density functions, and
- the inability to define stopping rules.

Of the different methods, the ray-by-ray correction is the most efficient of the iterative technique because it incorporates corrections during the iteration without a significant increase in computation time.

Clinically, the reconstruction time required by these iterative methods is too long. The computer is often not capable of simultaneously performing scans, taking new data and calculating the old data from the previous scan. Because of these unacceptable time delays in reconstructing the data, most units now utilize one of the analytical methods for reconstruction.

3.3 Analytical methods.

Analytical reconstruction is based on an exact solution of equation (3.2).

3.3.1 Basic concepts.

A. Sampling.

Radionuclide distributions in patients and alteration in the distribution with time are continuous functions. In order to represent them for processing with a digital computer it is necessary that these functions to be digitized. That is, the functions must be sampled so that a set of discrete elements results. Typically, the image area is divided into a 64 X 64, 128 X 128 or 256 X 256 matrix of discrete pixels. The size of the matrix is specified at reconstruction time.

Temporal sampling is performed by determining the length of time each image is to be required and how many images are to be required for a study.

B. Object and frequency domain.

Nuclear medicine data usually represents images in terms of counts at given spatial coordinates (x,y). This representation of data in terms of spatial (or temporal) functions is called the *object domain* representation.

The basic concept of Fourier analysis is that any function or variation of a quantity in space (or time) can be expressed as a sum of sine and cosine waves, each of different frequencies with appropriate amplitudes assigned to each frequency component. This description in terms of spatial (or temporal) frequencies is termed the *frequency domain* representation. Thus, data can be represented in terms of counts and spatial coordinates in the object domain, or amplitudes and frequencies in the frequency domain.

C. Sampling in the two dimensions.

Five quantities are associated with the sampling process:

1. the number of samples, N,
2. the spatial sampling interval or pixel size, Δx,
3. the spatial period or camera field size, X,
4. the sampling interval in the frequency domain, Δf,
5. the period in the frequency domain or the range over which the frequencies are sampled, F.

These quantities are related by three independent equations:

$$X = N \Delta x \tag{3.7}$$

$$\Delta x = 1/F \tag{3.8}$$

$$\Delta f = 1/X \tag{3.9}$$

Once any two of the quantities are defined, the other three are determined by these equations. For example, if an image with 25 cm field of view is recorded as a 128 X 128 matrix, then the pixel dimension is 0.2 cm , and the sample period in the frequency domain is 5.12 cm^{-1}.

3.3.2 Fourier reconstruction.

The starting point for an analytical reconstruction is to express the dersity function as a two-dimensional Fourier transform [13]:

$$f(x,y) = \int_{-\infty}^{\infty} \int_{-\infty}^{\infty} F(k_x,k_y) \exp [2\pi i(k_x x + k_y y)] \, dk_x \, dk_y \tag{3.10}$$

In this form, f(x,y) is expressed as a superimposition of sinusoidal and cosinusoidal wave, represented by the complex exponential. The Fourier transform is a way of transforming the representation of data from one domain to the other domain.

The Fourier coefficients $F(k_x,k_y)$ are defined by the Fourier transform:

$$F(k_x,k_y) = \int_{-\infty}^{\infty}\int_{-\infty}^{\infty} f(x,y)\ \exp\left[-2\pi i(k_x x + k_y y)\right]\ dx\ dy \qquad (3.11)$$

Rotating the (x,y) axes to new axes (r,s) shown in Fig. 3.1, where the angle of rotation is:

$$\phi = \text{arctg}\ (k_x/k_y) \qquad (3.12)$$

and

$$k = (k_x^2 + k_y^2)^{1/2} \qquad (3.13)$$

$$k_x = k\cos\phi \qquad k_y = k\sin\phi \qquad (3.14)$$

then,

$$F(k_x,k_y) = \int_{-\infty}^{\infty}\int_{-\infty}^{\infty} f(x,y)\ \exp\left(-2\pi ikr\right)\ dr\ ds \qquad (3.15)$$

Exchanging the order of integration, it can be seen that the s integral is just the ray sum $p(r,\phi)$ given by eq. (3.2), so that:

$$F(k_x,k_y) = \int_{-\infty}^{\infty} p(r,\phi)\ \exp\left(-2\pi ikr\right)\ dr = P(k,\phi) \qquad (3.16)$$

where $P(k,\phi)$ is the Fourier transform of $p(r,\phi)$ with respect to r.

The equation (3.16) states that each Fourier coefficient (or wave amplitude) of the density function is equal to a corresponding Fourier coefficient of the projection, taken at the same angle as the Fourier wave. In words, the one dimensional Fourier transform of the projection at an angle corresponds to a slice taken at an angle through the two-dimensional Fourier transform of the original function.

This is the *projection slice theorem* that relates the Fourier transform of the density function f(x,y) to the Fourier transform of the projection $p(t,\phi)$. [20]

Therefore, the mathematical basis of Fourier reconstruction is that the Fourier coefficients of the image can be expressed in terms of the Fourier coefficients of the projections. This allows the Fourier coefficients of the image to be derived from those of the projections. The picture image is then synthesized from its Fourier coefficients. This is illustrated in Fig. 3.4 for a homogeneous rectangle in two projections.

The approximate reconstruction from simple back-projection may be related to the true image.

Equation (3.4) may be converted from a summation to an integral:

$$\hat{f}(x,y) = \int_0^{\pi} p(x \cos \phi + y \sin \phi, \phi)\, d\phi \qquad (3.17)$$

Replacing $p(x \cos \phi + y \sin \phi, \phi) = p(r,\phi)$ by its Fourier representation,

$$p(r,\phi) = \int_{-\infty}^{\infty} P(k,\phi) \exp(2\pi i k r)\, dk \qquad (3.18)$$

gives:

$$\hat{f}(x,y) = \int_0^{\pi} \int_{-\infty}^{\infty} \frac{P(k,\phi)}{|k|} \exp(2\pi i k r)\, |k|\, dk\, d\phi \qquad (3.19)$$

where the integrant has been multiplied and divided by $|k|$, so that the right side is expressed in the form of a two-dimensional Fourier integral in polar coordinates:

$$dk_x\, dk_y = k\, dk\, d\phi \qquad (3.20)$$

The Fourier coefficients of the simple back-projection $\hat{F}(k_x,k_y)$ are then:

$$\hat{F}(k_x,k_y) = \frac{P(k,\phi)}{|k|} \qquad (3.21)$$

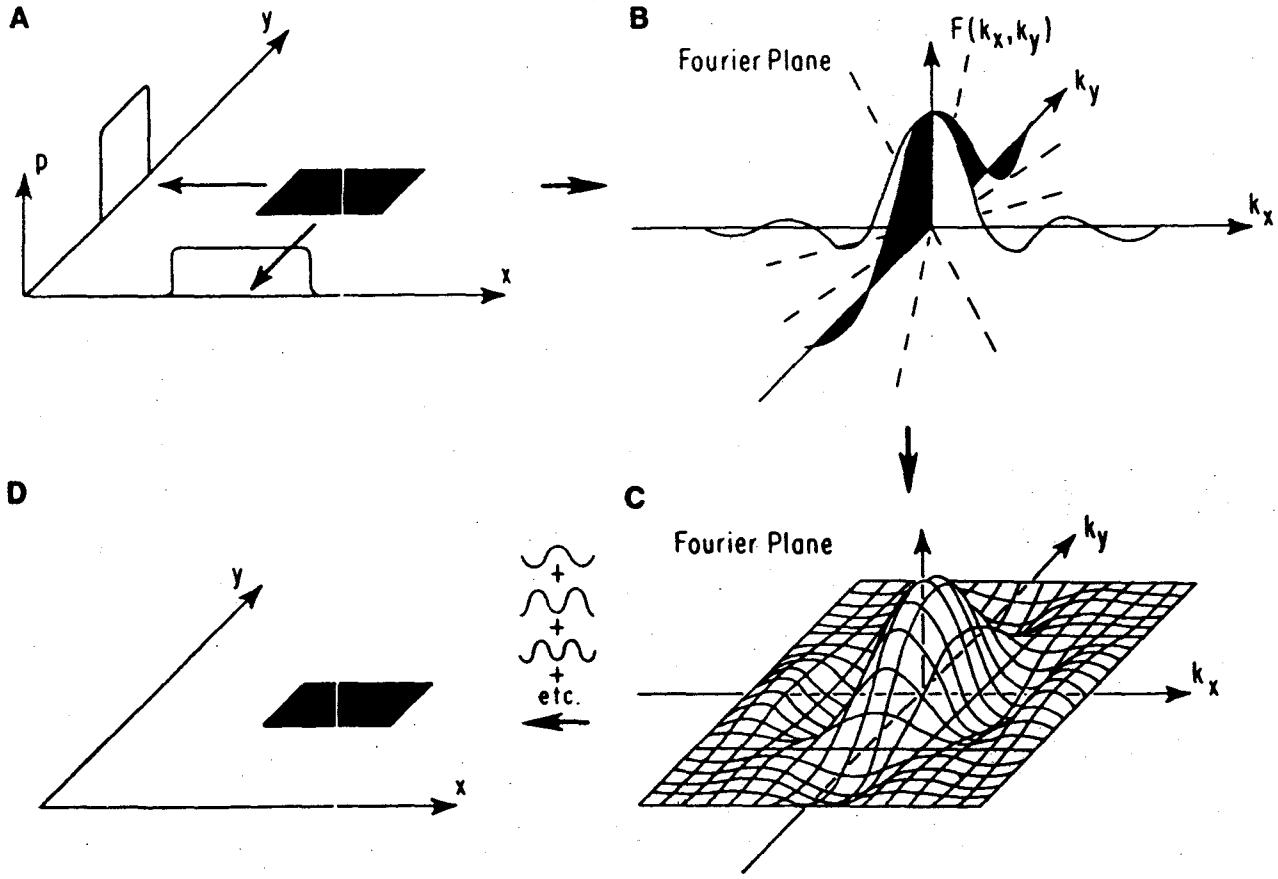

Fig. 3.4 *Fourier reconstruction.*

A) *Projections of a rectangular object.*

B) *Amplitudes (Fourier coefficients) of the Fourier transform of the rectangular projections, in the frequency plane. Dashed lines suggest the presence of other transformed projections.*

C) *The sinusoidal waves with amplitude given by Fourier coefficients.*

D) *The reconstructed image obtained adding together the sinusoidal waves.*

Using eq. (3.16),

$$\hat{F}(k_x,k_y) = \frac{P(k,\phi)}{|k|} = \frac{F(k_x,k_y)}{|k|} \qquad (3.22)$$

That is, the Fourier coefficients of the simple back-projection are equal to the exact Fourier coefficients $F(k_x,k_y)$ of the true image, divided by the magnitude of the spatial frequency $|k|$.

A significant implication of equation (3.22) is that back projection may be feasible if the projections are modified appropriately, or filtered priori to being back-projected.

3.3.3 Filtered back-projection.

In filtered back-projection, the profiles obtained in simple back-projection are modified or filtered priori to being back-projected. This is done to correct for the background density that occurs in simple back-projection.

The basic problem is to find a mathematical function called a convolving or convolutional function, which can be used to operate on, or filter the different projection so that when these adjusted or corrected projections are back-projected and then summated, the background density will be eliminated. This is accomplished by using a convolutional function, which applied to the original projections, results in filtered projections with positive and negative components. When back-projected, these components of different polarity should average out to zero at all points outside the original object.

It can be seen in Fig. 3.5 that the filtering function has negative and positive lobes. The purpose of these lobes is to eliminate from the image the background noise or density arising from the unwanted spokes generated in a simple back-projection.

Following back-projection and summation, the contours and density variations of the original object should be accurately reproduced.

Different, but mathematically equivalent filter formula have been used for filtered back-projection.

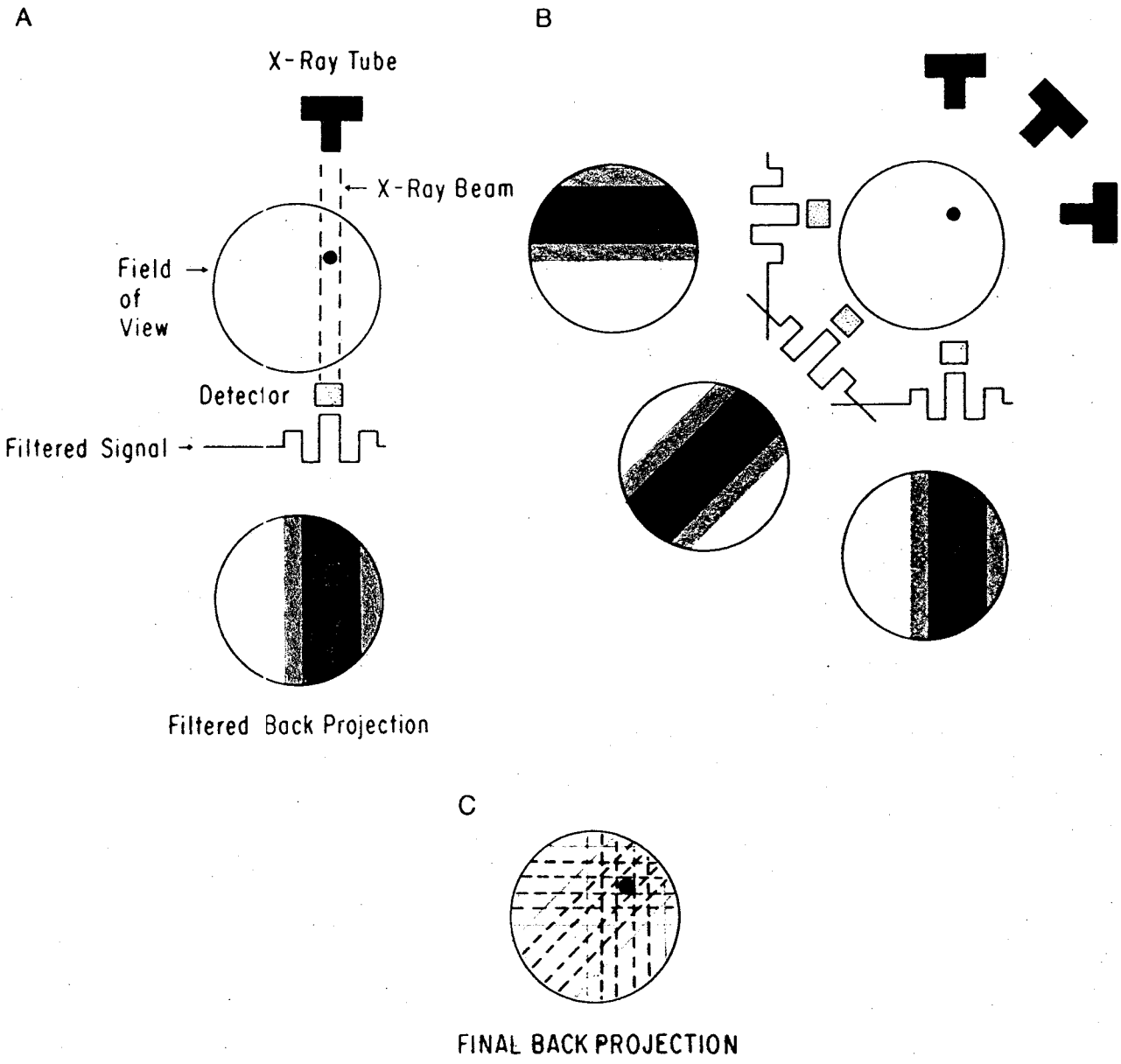

Fig. 3.5 *Filtered back-projection method.*

A) *The ray sum from a single dense object is first filtered by a function with negative and positive components. The filtered ray-sum is then back-projected.*

B) *Each different projection is sequentially filtered and back-projected.*

C) *The summation is performed and the effect of the positive and negative components is to cancel out.*

A. Fourier filtering.

Equation (3.10) is written in polar coordinates as:

$$\hat{f}(x,y) = \int_{0}^{\pi} \int_{-\infty}^{\infty} F(k_x,k_y) \exp [2\pi i k (x \cos \phi + y \sin \phi)] |k| \, dk \, d\phi \tag{3.23}$$

where ϕ and k have been defined in equations (3.12) and (3.13) respectively.

The value of k is allowed to range from $-\infty$ to $+\infty$ so that the inner integral takes the form of a one dimensional Fourier transform; ϕ must have integration limits 0 to π.

Using eq. (3.16) which gives $F(k_x,k_y) = P(k,\phi)$ and eq. (3.20) the density function (3.23) is changing in:

$$\hat{f}(x,y) = \int_{0}^{\pi} p^*(x \cos \phi + y \sin \phi, \phi) \, d\phi \tag{3.24}$$

where:

$$p^*(r,\phi) = \int_{-\infty}^{\infty} |k| \, P(k,\phi) \exp (2\pi i k r) \, dk \tag{3.25}$$

In practice, a summation is used:

$$\hat{f}(x,y) = \sum_{j=1}^{m} p^*(x \cos \phi + y \sin \phi, \phi) \, \Delta\phi \tag{3.26}$$

where m is equal to the number of projections and $\Delta\phi$ is the interval between projections.

Equation (3.26) is similar to the eq. 3.4) obtained in simple back-projection except that p^* not p is being projected. The use of p^* rather than p represent a filtering process. However, p^* unlike p is not spatially bounded.

Two approximations are needed to implement this method. One is the substitution of a discrete sum for the integral over ϕ, that is going from eq. (3.25) to (3.26). The other one occurs because, for a specific projection angles, p^* is only calculated at a finite number of discrete points, not all along r.

B. The convolution reconstruction methods.

Basic concepts.

The convolution of two functions f(x) and g(x) is defined as:

$$h(x) = \int_{-\infty}^{\infty} f(u)\, g(x-u)\, du \qquad (3.27)$$

or briefly,

$$h(x) = f(x) * g(x) \qquad (3.28)$$

where the symbol * denotes convolution (Fig. 3.6). [19]

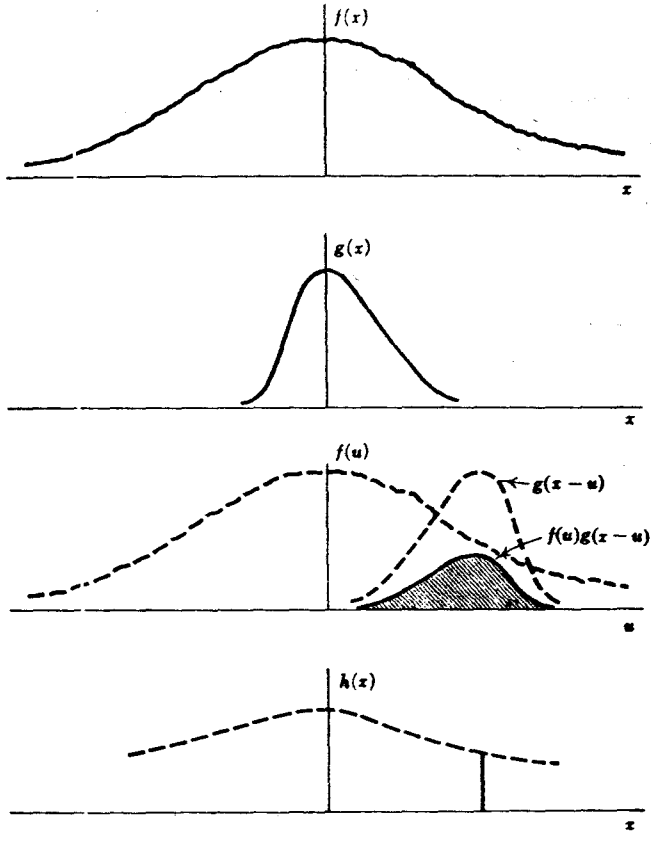

Fig. 3.6 *The convolution integral* h(x) = f(x) * g(x) *represented by a shaded area.*

For sampled function, the convolution sum is formed by centering one function at the desired point of the second function, multiplying the corresponding terms and then obtaining the sum. This can be expressed mathematically, for one dimension as:

$$h(x) = f(x) * g(x) = \sum_{n=-1}^{n=1} f(u)\, g(x-u) \qquad (3.29)$$

The convolution theorem states that, convolving two functions in one domain is exactly equivalent to multiplying their Fourier transform in the other domain. This is an important theorem because it allows one to work in either domain.

Thus, the convolution sum (3.29) can be expressed:

$$H(f) = F(f)\, G(f) \qquad (3.30)$$

where capital letters are used to indicate Fourier transform, and f is the frequency. (In nuclear medicine the magnitude of F(f) is commonly called the modulation transfer function (MTF)).

The convolution theorem explains the reason why sampling in one domain (multiplying by a series of Dirac delta functions) makes the Fourier transform periodic in the other domain. This is because the function is convolved with a series of Dirac delta functions which replicate the transform at spacing of $1/\Delta x$.

By the convolution theorem, filtering can be carried out in either domain. We could either convolve an object domain filter (eq. (3.27)) with an image, or by using eq. (3.30) we could Fourier transform both the image and filter, multiply them and inverse Fourier transform the result. The results of processing in the two domains are not always identical since there are some pitfalls which can occur.

The first potential problem is that of *aliasing*, [19, 21], which occurs when the data is not sampled finely enough to prevent the overlap of its periodic form in the frequency domain (high frequencies masquerade lower frequencies in sampled data). This results because it is not possible to define a frequency unless it has been sampled at least twice during its period in the object domain.

Thus, the maximum frequency (smallest bar) which could be recorded in a sampled image is given by:

$$f_N = 1/(2\ \Delta x) \tag{3.31}$$

This is called the Nyquist or folding frequency.

The Nyquist sampling theorem states that an adequate reproduction or imaging of an object can be achieved if the spacing between data samples is less than half that associated with the highest spatial frequency contained in the object, that is, the spatial sampling frequency must be more than twice the highest spatial frequency in the data being measured.

The aliasing effect can be avoided by sampling the image such that F(f) of the system will have made vanishingly small any amplitude of frequencies greater than the Nyquist frequency f_N.

Leakage is a frequency domain problem which occurs at abrupt edges. This "windowing" of the data is equivalent to multiplying the image by a rectangular function. By the convolution theorem this is equivalent to convolving the Fourier transform of the rectangular function which is a sinc function (Fig. 3.7) with the Fourier transform of the image. Since the sinc function:

$$\text{sinc } x = \frac{\sin \pi x}{\pi x} \tag{3.32}$$

has rather large "sidelobs", the result is the spreading or leaking of frequencies from one region to another (Gibbs phenomena). This artifact can be reduced by smoothing the edge of the window (i.e. using a different window function) to reduce the side lobes.

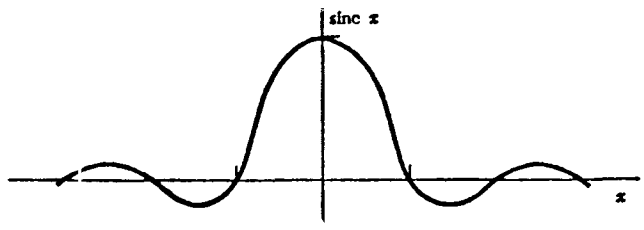

Fig. 3.7 *The function* sinc x.

Radon filtering.

Equation (3.25) which gives the modified projections p^*, represents the Fourier transform of the product of two functions $|k|$ and $P(k,\phi)$. Applying the convolution theorem to eq. (3.25), one obtains:

$$p^*(r,\phi) = -\frac{1}{2\pi^2}\int_{-\infty}^{\infty}\frac{p(r',\phi)}{(r-r')^2}\,dr' \qquad (3.33)$$

where $p(r.\phi)$ is the Fourier transform of $P(k,\phi)$, and $-\frac{1}{2\pi^2 r^2}$ is the Fourier transform of $|k|$. The equation (3.31) can be transformed into:

$$p^*(r,\phi) = \frac{1}{2\pi^2}\int_{-\infty}^{\infty}\frac{\partial p(r',\phi)/\partial r'}{r-r'}\,dr' \qquad (3.34)$$

This equation describes the filtering process as a single convolutional integral in which the derivatives of p weighted by the inverse distance from the point at which the filtered value is derived, are added together.

Convolution filtering.

There is a divergence in eq. (3.25) caused by the factor $|k|$. This divergence can be avoid if $|k|$ is replaced by a function:

$$|k| = \begin{cases} |k_m| & \text{for } |k| \le k_m \\ 0 & \text{elsewhere} \end{cases} \qquad (3.35)$$

where k_m is the greatest spatial wave number or frequency present in the projection (Nyquist frequency). In this case, the integrant in eq. (3.25) contains only frequencies up to k_m.

There are three consequences of band limiting:

- the image can be reconstructed on an array of cells spacing w:

$$w = k_m/2 \qquad (3.36)$$

- the projections may be sampled at the same interval w,
- the Fourier transform may be replaced by discrete Fourier series.

The Fourier transform of the cutoff version of $|k|$ is: [18]

$$\int_{-\infty}^{\infty} |k| \exp(2\pi i k r)\, dk = \frac{k_m}{\pi r} \sin(2\pi k_m r) - \frac{\sin^2(\pi k_m r)}{\pi^2 r^2} \tag{3.37}$$

Replacing $|k|$ in eq.(3.25) by its cutoff version and applying the convolution theorem,

$$p^*(r,\phi) = \int_{-\infty}^{\infty} p(r,\phi) \left\{ \frac{k_m \sin[2\pi k_m (r - r')]}{\pi(r - r')} - \frac{\sin^2[\pi k_m (r - r')]}{\pi^2 (r - r')^2} \right\} dr' \tag{3.38}$$

This may be simplified to:

$$p^*(r,\phi) = k_m\, p(r,\phi) - \int_{-\infty}^{\infty} p(r',\phi) \frac{\sin^2[\pi k_m (r - r')]}{\pi^2 (r - r')^2}\, dr' \tag{3.39}$$

Here the $p(r,\phi)$ is the measured projection, $p^*(r,\phi)$ is the modified projection.

Equation (3.39) has the form of a convolution integral. It can be simplified for implementation.

The integrand can be replaced by a summation. Also, the $\sin^2$ term is either 0 or 1, depending upon whether $k_m(r - r')$ is an even or odd multiple of w (eq. (3.36)).

Therefore equation (3.39) can be rewritten as:

$$p^*(r_j) = \frac{p(r_j)}{4w} - \frac{1}{\pi^2 w} \sum_{j=1,\ \text{odd}} \frac{p(r_j)}{(i - j)^2} \tag{3.40}$$

This result is a relatively simple and fast programm.

C. Filter functions.

The filtered back-projection algorithm performs the following sequences of operations:

- the discrete Fourier transform of the projection data vector, $\mathcal{F}_1(p)$,
- multiply the complex values by a filter function G,
- the inverse discrete Fourier transform of these modified frequencies $\mathcal{F}_1^{-1}[G\ \mathcal{F}_1(p)]$ giving the convolved projections, and
- these convolved projection data are back-projected to give the reconstruction:

$$X = \text{backproject}\left\{ \mathcal{F}_1^{-1}\left[G\ \mathcal{F}_1(p)\right] \right\} \qquad (3.41)$$

where X is the transverse section, $\mathcal{F}_1$ denotes one-dimensional Fourier transformation.

The filter function G(f) is the Fourier transform of the convolution function G(d). In other words, a digital filtering can be defined as the Fourier space implementation of the real space convolution equation:

$$q_n = \sum_k g_{n-k} * p_k \qquad (3.42)$$

Real space convolution and frequency filtering are equivalent operations.

In practice, the filter function G(f) is equal to the product of a window W(f) and the absolute value of the frequency |f| (ramp function), [7]:

$$G(f) = |f|\ W(f) \qquad (3.43)$$

Then, symbolically, equation (3.41) can be written:

Modified projection =

$$= \mathcal{F}_1^{-1}\left[|f|\ W(f)\ \mathcal{F}_1(\text{projection data})\right] \qquad (3.44)$$

From the convolution theorem, the equivalent result can be obtained as:

Modified projection =

$$= \left\{ \mathcal{F}_1^{-1} \left[|f| \, W(f) \right] \right\} * \text{projection data} \qquad (3.45)$$

where the convolver $\mathcal{F}^{-1}\left[|f| \, W(f) \right]$ is determined by the window function W(f). A desirable window W(f) should have the following properties:

a) $W(0) = 1$ so that the behaviour near the origin is retinued,

b) $W(f) = 0$ for any $|f| > 1/(2\,w)$ so that the proper cutoff frequency is maintained,

c) $W(f) \leq 1$ for $|f| \leq 1/(2\,w)$. Violation of this condition would result in an overemphasis of those frequencies for which $|W(f)| > 1$,

d) W(f) is real and even, so that the resulting convolving function is real and even.

There are different kinds of windows and filters respectively. The most used filter functions were classified in five general classes: ramp, Hann, Hamming Parzen, and Butterworth.

Rectangular window and ramp filter.

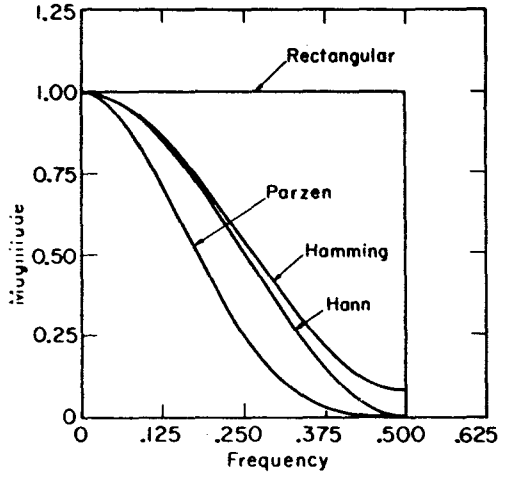

Fig. 3.8 *Window functions.*

The rectangular window (Fig. 3.8) is defined by:

$$W(f) = \begin{cases} 1 & \text{if } |f| \leq f_m \\ 0 & \text{if } |f| > f_m \end{cases} \qquad (3.46)$$

Multiplying the rectangular window by the ramp function in frequency space gives the ramp filter (Fig. 3.9 a):

$$G(f) = \begin{cases} |f| & \text{if } |f| \leq f_m \\ 0 & \text{if } |f| > f_m \end{cases} \qquad (3.47)$$

The inverse Fourier transform of the ramp filter gives the convolution function, (Fig. 3.9 b)

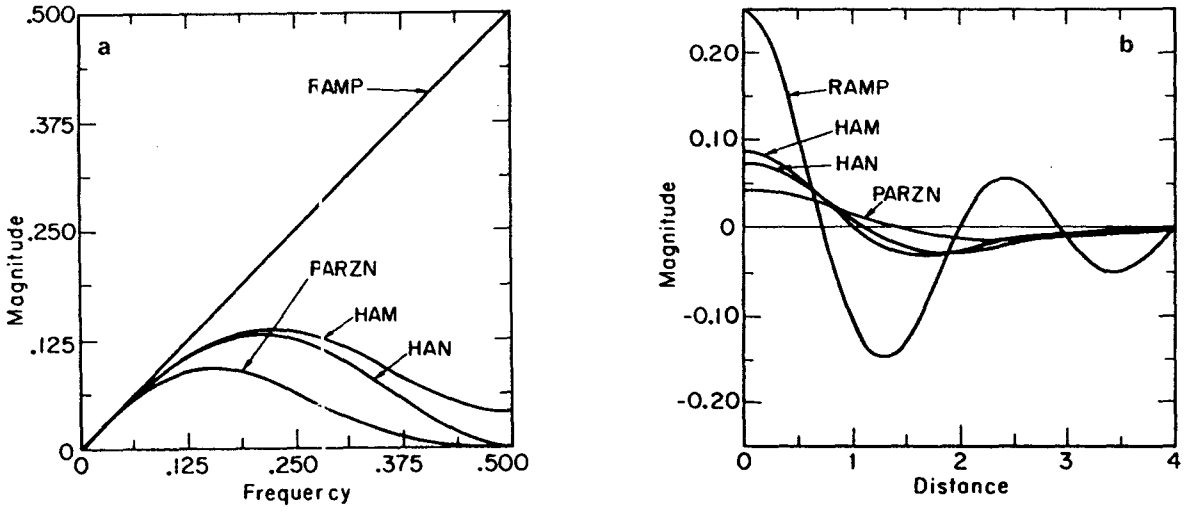

Fig. 3.9 *Filter functions.*
a) *in frequency domain,*
b) *in object domain (the real space convolution function).*

The ramp filter gives the best resolution in the reconstructed image for perfect data, but amplifies noise for data with statistical fluctuations. The sharp frequency cutoff gives rise to oscillations at sharp boundaries in the image of the object and thus generates artifacts in the reconstructed image. This effect can be reduced by using other types of windows in which the frequency cutoff is rolled off and not cutoff sharply.

Hann window and Hann filter.

The Hann window (Fig. 3.8) is defined by the equation:

$$W(f) = \begin{cases} 0.5 + 0.5 \cos \dfrac{\pi f}{f_m} & \text{if } |f| \leq f_m \\ 0 & \text{if } |f| > f_m \end{cases} \qquad (3.48)$$

Multiplying the Hann window by the ramp function gives the Hann filter (Fig. 3.9 a):

$$G(f) = \begin{cases} 0.5\,|f| + 0.5\,|f| \cos \dfrac{\pi f}{f_m} & \text{if } |f| \leq f_m \\ 0 & \text{if } |f| > f_m \end{cases} \qquad (3.49)$$

The convolved function, the filter in the object space, is presented in Fig. 3.9 b.

For the Hann filter, the image has a smother texture with a loss in resolutior.

Hamming window and Hamming filter.

The Hamming window (Fig. 3.8) is defined by:

$$W(f) = \begin{cases} A + (1 - A) \cos \dfrac{\pi f}{f_m} & \text{if } |f| \leq f_m \\ 0 & \text{if } |f| > f_m \end{cases} \qquad (3.50)$$

where A can take any values between 0 and 1. For A = 1 the window reduces to the rectangular window; for A = 0 the Hamming window is a cosine window.

The filter in the frequency space is (Fig. 3.9):

$$G(f) = \begin{cases} A\,|f| + (1 - A)\,|f| \cos \dfrac{\pi f}{f_m} & \text{if } |f| \leq f_m \\ 0 & \text{if } |f| > f_m \end{cases} \qquad (3.51)$$

Parzen window and Parzen filter.

The Parzen window is defined by the equation (Fig. 3.8):

$$W(f) = \begin{cases} 1 - 6\,(|f|/f_m)^2\,(1 - |f|/f_m) & \text{if } |f| \le f_m/2 \\ 2\,(1 - |f|/f_m)^3 & \text{if } f_m/2 < |f| \le f_m \\ 0 & \text{if } |f| > f_m \end{cases} \tag{3.52}$$

where f_m is the cutoff frequency.

Similarly, the Parzen filter is defined by (Fig. 3.9):

$$G(f) = \begin{cases} |f| - 6\,|f|\,(|f|/f_m)^2\,(1 - |f|/f_m) & \text{if } |f| \le f_m/2 \\ 2\,|f|\,(1 - |f|/f_m)^3 & \text{if } f_m/2 < |f| \le f_m \\ 0 & \text{if } |f| > f_m \end{cases} \tag{3.53}$$

The reconstructed image resolution will be less than can be achieved with the Hann or Hamm filters. On the other hand the Parzen filter suppresses noise.

Butterworth window and Butterworth filter.

The major advantage of this filter is that it can be modified according to the amount of noise in the projection data.

The Butterworth window function is:

$$W(f) = \frac{1}{1 + (|f|/f_m)^{2n}} \tag{3.54}$$

where f_m is a frequency parameter and n is the order of filter.

This is multiplied by the ramp function giving the Butterworth filter:

$$G(f) = \frac{|f|}{1 + (|f|/f_m)^{2n}} \tag{3.55}$$

The shape of the filter is designed by declaring values for f_m and n. The order n of a Butterworth filter can be an integer or any real value.

A filter is obtained by calculating the appropriate window width between 0 and f_p and the stop-band frequency f_s as illustrated in Fig. 3.10.

If the values of ε, A, f_p and f_s are known for a particular window, then the parameters n and f_m of the Butterworth filter are determined by:

$$n = \frac{\log \left[\varepsilon / \left(A^2 - 1\right)^{1/2}\right]}{\log \left(f_p / f_s\right)} \tag{3.56}$$

$$f_m = \frac{f_p}{(\varepsilon)^{1/n}} \tag{3.57}$$

The window defined by the Butterworth filter can be designed so that it has a narrow transition band between f_p and f_s, and thus approaches a rectangular window, or can be designed so that it has a wide transition band such as the Hann or Hamming window (Fig. 3.11 a).

The Butterworth filter (Fig. 3.11 b) gives the possibility to realize a compromise between a good resolution in the reconstructed image but amplifying noise and a poorer resolution with reduced noise amplification.

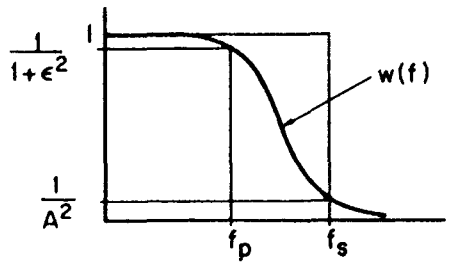

Fig. 3.10 *Method of designating a Butterworth filter. The parameters ε and A are calculated from ordinates at the selected pass frequency f_p and stop frequency f_s.*

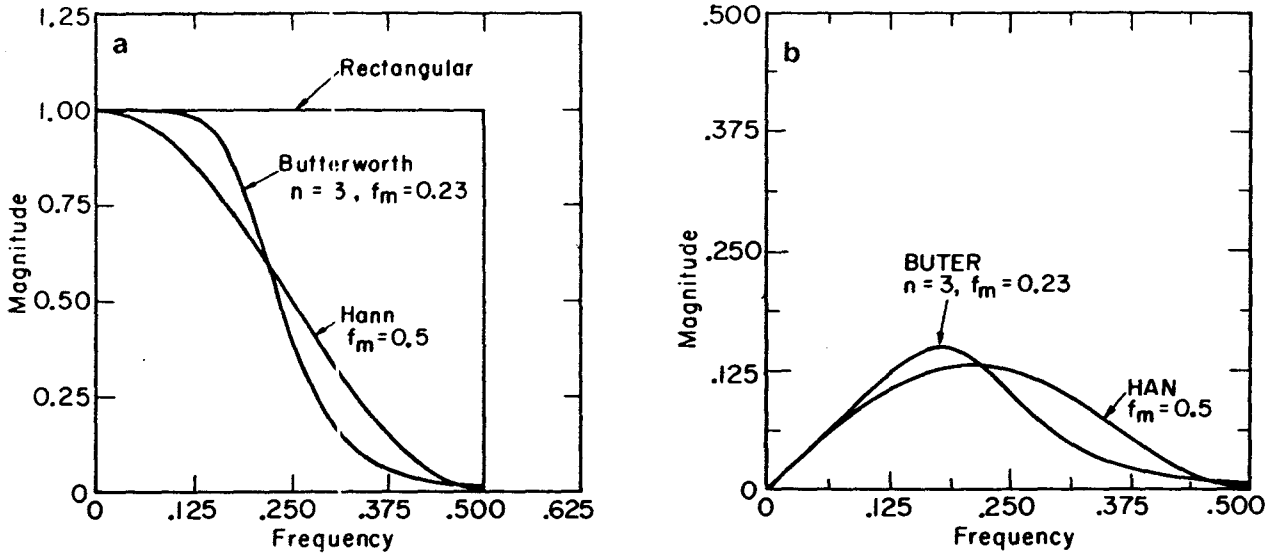

Fig. 3.11 *The Hann filter and the Butterworth filter.*

a) *The Hann window with a cutoff frequency* $f_m = 0.5$ *and the Butterworth window with* $n = 3$ *and* $f_m = 0.23$.

b) *Hann filter and Butterworth filter obtained with those parameters.*

Analytical methods are generally significantly faster than iterative techniques. A complete analytical reconstruction can be performed in the time that it would take to do a single iteration in an iterative approach. Furthermore, with analytical methods, data can be processed for one patient while the other patient data still being collected.

4. QUANTITATIVE AND QUALITATIVE ACCURACY IN PET IMAGES.

The major goal of radionuclide imaging is the three-dimensional spatial and temporal quantitative description of isotope distribution. The quantitative capabilities of a PET system are in the limits imposed by finite resolution and counting statistics. However, as with any nuclear medicine measuring device, PET images are seriously affected by other factors as: scattering and accidental coincidences, system dead time, etc. An understanding of these limitations is essential to a rational interpretation of data.

4.1 The resolution of the image.

4.1.1 The spatial resolution.

The *spatial resolution* is defined as the ability of the system to separate adjacent structures under optimal conditions. The spatial resolution or resolving capability of the system is usually defined in terms of the minimum distance between the two high contrast objects at which they may be detected or identified as separate objects in the image. [18]

The detector aperture size is typically the most significant of the geometric factors determining spatial resolution. The measurements of spatial variation of a physical parameter (activity) is limited by the size of the detector used in measurement.

Appropriate test objects for the purpose of measuring the spatial resolution of a nuclear medicine system are a point and a line source.

The *point spread function* is the width of the point spread function at half its maximum value (FWHM). In ideal systems the point spread function is isotropic (spatially symmetrical) and independent of position. For a PET system, the point source must be of infinitesimal dimensions. The image of this point like object will then approximate the point response of the tomograph.

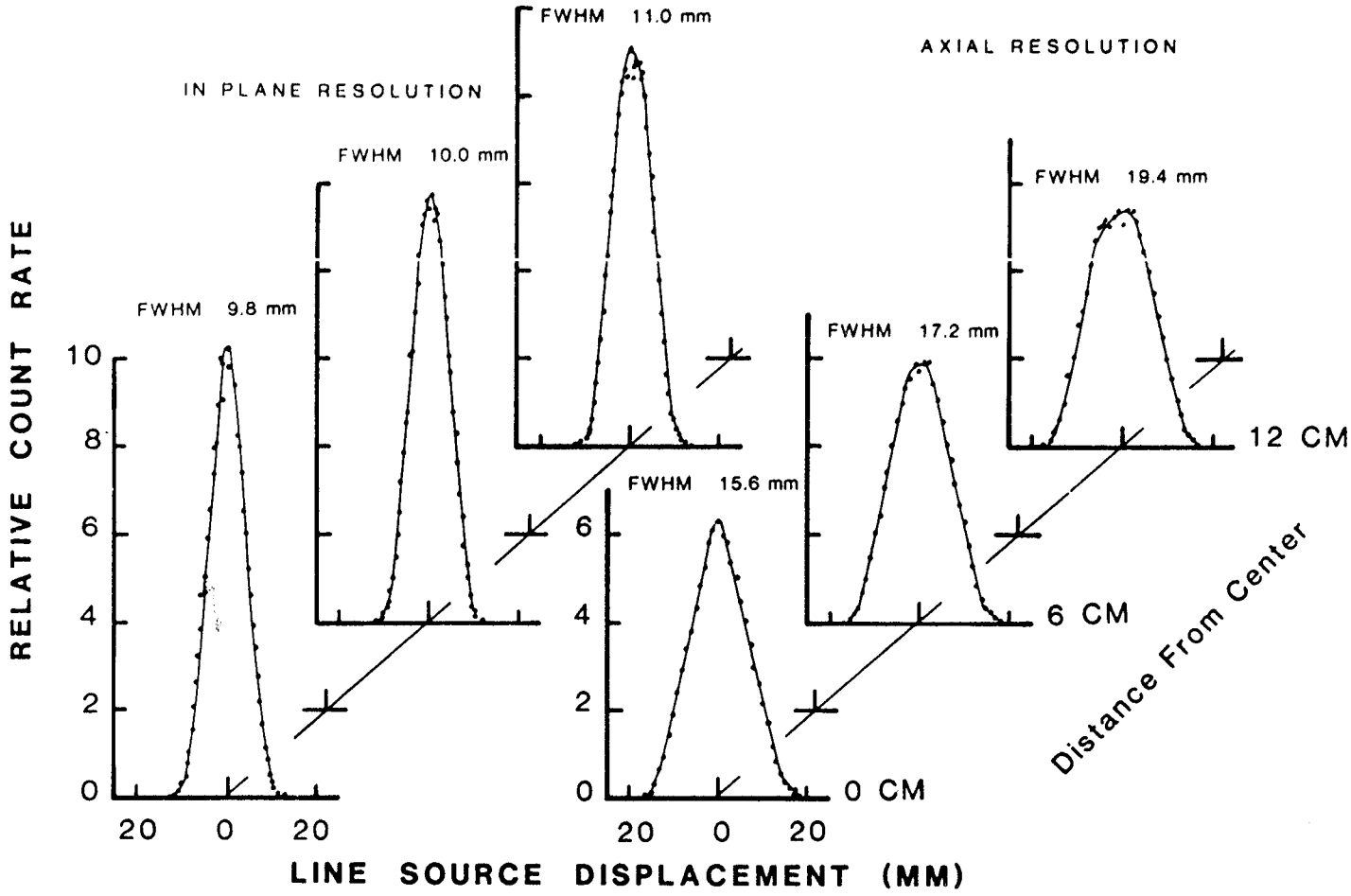

Fig. 4.1 *Line Spread Function. In plane and axial* LSFs *for the* Neuro ECAT, *as a function of source position.*

The *line spread function* is a description of the distribution of radiation intensity that results from imaging a straight line object of infinitesimal width by an imaging system that creates two-dimensional images.

The line spread function may be measured directly by scanning a phantom in the form of a thin object in a water bath. The object must be thin compared to the resolution of the tomograph.

Fig. 4.1 [9] presents the line spread function in plane and axial as a function of source position for "NeuroECAT" tomograph. The intrinsic resolution, both transverse and axial in the centre of the tomograph has FWHM smaller than at larger distances. These variations within both planar and axial resolution could cause image artifacts and loss in quantitation.

Fig. 4.2 shows that any point in the Field of View (FOV) is viewed by a number of detector-pairs. The axial composite point spread function is the average over all the detector pairs resolution.

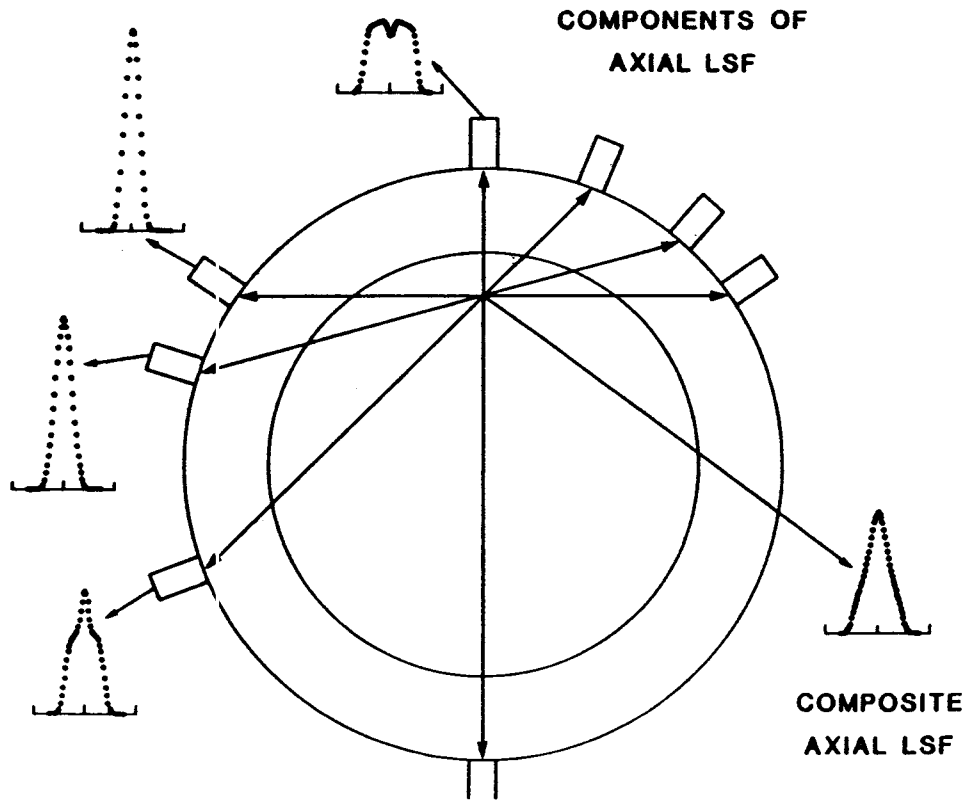

Fig. 4.2 *The composite Point Spread Function* (PSF) *is the average over the all axial PSF corresponding to all detectors pairs.*

4.1.2 The contrast resolution.

Contrast resolution refers to the capability of the PET system to detect an object with a small difference in activity distribution, in relation to a homogeneous background. Contrast is one of the most important characteristics defining an image.

Phantoms designed to measure contrast resolution usually employ circular objects, either spheres or cylinders.

Contrast resolution is typically expressed in one of two ways: as the smallest difference in the concentration activity that can be discriminated for an object of a particular diameter, or as the smallest diameter of an object with a particular contrast that can be detected.

The primary limitation in detecting a small difference between an object and its background is determined by noise.

4.1.3 The temporal resolution.

Temporal resolution refers to the ability of an instrument to register events occurring within a very small time interval, as separate events.

The temporal resolution is physically related to the system's ability to record data fast. This requires a good detection efficiency, a low dead time for whole system and high maximum data rates.

Improved spatial, contrast and temporal resolutions in positron tomography results in more accurate quantitation, reducing smearing from one region to another and discriminating activities in closely adjacent structures with differing physiological functions.

4.1.4 The image noise.

The spatial resolution and the contrast resolution are degraded by noise which often represents the ultimate factor to image quality.

Noise represent that portion of the signal that contains no information. Its presence marks the information-containing of the signal. There are several sources of noise which may originates at any point in the chain of processes that comprise the total PET system.

Statistical noise (quantum noise).

The response of any detector depends upon the number of γ rays that it intercepts. Statistical noise occurs because of inherent statistical fluctuations that arise from the detection of a random number of gamma quanta.

The amount of statistical noise follows a Poisson distribution and is proportional to the standard deviation:

$$\sigma = \frac{\sqrt{N}}{N} = \frac{1}{\sqrt{N}} \tag{3.58}$$

where N is the average number of counts registered.

A reduction in statistical noise will necessitate an increase in statistics which can be attend by a lengthening of the examination time or increasing the dose delivered to a patient.

Electronic noise.

Each of the electronic circuits associated with PET system is capable of introducing some noise into the system but analog electronics are sufficiently well designed that the electronic noise contribution is only a fraction of that of the statistical noise.

Round off errors.

Digital computers generally do not introduce electronic noise into the system, however they may introduce noise in the process of reconstruction through round off errors. These errors may be reduced by using a larger memory (a larger number of bits per word) or through programming.

Artifactual noise.

An artifact (leakage, aliasing effect) may be considered as a type of noise, since it represents a part of the signal or image that contains no information and obscure the true information present in the image. Artifacts affect overall image quality and detail including contrast and spatial resolution. [36]

Filter noise (reconstruction algorithm)

The initial purpose of filtration was to eliminate the blur artifact associated with simple back-projection. The filter function can have an important effect on image quality.

The application of the appropriate convolution kernel can introduce either smoothing or edge enhancement. In the case of a smoothing filter, both high frequency signal components and high frequency noise can be reduced. This modifies not only the appearance of the image but the quality of the noise as well. In this case, the higher frequency components of the noise become selectively attenuated compared to lower frequency components. In contrast, a filter for edge enhancement will retain and even emphasize the high frequency components of both the signal and the noise. Therefore, the reconstruction filter is the main parameter determining the image signal-to-noise ratio.

4.2 Factors affecting quantitative measurements with PET.

As in all types of nuclear emission imaging, accuracy in PET is determined by statistics factors and limited by systematic factors.

4.2.1 Statistical factors.

Statistical accuracy depends on the number of coincident events that are collected within the available time. This is determined both by the available positron activity and the sensivity of the tomograph to detect these events.

A. The positron activity.

The activity delivered to a patient, or the number of detectable events is limited by the dose rates acceptable for human use. To provide some perspective on the problem, data from brain studies with ^{18}F labeled 2-fluoro-2-deoxy-D-glucose (^{18}FDG) and ^{13}N labeled ammonia ($^{13}NH_3$) are presented in Table 4.1. [23]

Table 4.1 Count rates available for PET in human brain studies with ^{18}FDG and $^{13}NH_3$

Radiopharmaceutical	^{18} FDG	$^{13}NH_3$
Injected dose	10 mCi	30 mCi
Average activity per cm^3 in brain at start of scan	4 μCi	9 mCi
Total available count rate	48 Kcps	108 Kcps
Available counts 10 min scan	$2.9\ 10^7$	$4.4\ 10^7$

From the activity per cm^3 in the brain, the total available count rate calculated for 1 cm slice thickness, assuming a perfect detection system is 30-40 million detectable events for 10 mCi ^{18}FDG injection. In practice less than 50% of these events are detected. This translates into a maximum of 15-30 million accumulated events for 10 min scans for 1 cm slice thickness.

Image quality must be adequate to accurately define the spatial extent of the organ of interest as well as provide sufficient count density to measure isotope concentration. In practice, ^{18}FDG images obtained by PET systems with intrinsic resolution of 0.75 cm still requires smoothing to a final image resolution of 1.0 cm FWHM at 3-6 million counts in order to give a final image without obvious statistical mottle. [23]

B. The tomograph sensivity.

The tomograph sensivity is a measure of the efficiency for coincidence detection of positron annihilation radiation in all the system. The sensivity of the tomograph is essential to minimize patient dose and obtain statistically high-quality scans in short time periods. Therefore, the goal of the tomograph designs is to assure the best spatial, contrast and temporal resolution with highest sensivity technically achievable.

In plane and axial coverage.

To achieve a high spatial resolution, the tomograph design has to have a gooc in plane and axial coverage. This can be realized using small detectors in a small diameter of the gantry, to increase the solid angle for detection, and using multiple plane designs that increase efficiency of detection.

The detector size is the most important factor determining the spatial resolution in PET. A small detector will measure and record the distribution of the radiotracer over small distances and it is able to identify more rapidly spatial changes.

From the dimensions of a detector, its width sets limits on the transverse resolution, but does not substantially affect ring efficiency. Using very narrow detectors, the localization of information along the data profile is improved. That is, the high frequency component (small objects) of the signal are amplified because they are detected much more clearly with narrow detectors. (Signal Amplification Technique (SAT)). [24, 25] The detectors that are employed are much narrower than the expected resolution of the final image. The high resolution tomograph designs utilize detectors 5-10 mm wide.

The detector depth must represent several interaction lengths for 511 KeV gamma rays for a good efficiency. For BGO crystals, the depth is typically 30 mm. A greater scintillation depth (especially for materials of greater interaction length such as CsF and BaF_2) increases angulation errors and causes deterioration of spatial resolution.

The detector height determines the thickness of the tomographic slice, affects the efficiency of the ring, and limits the axial resolution. Detector height is typically about 20 mm giving an axial resolution of about 11 mm.

A good solid angle and axial coverage can be achieved using multiple rings of small closely packed detectors that encircle the patient. Cross-ring coincidences realize the full available solid angle and the multiple detector rings cover a large volume of tissue, thus providing a higher event rate for a given administered tracer activity.

The detector's material.

The ideal detector material for a high sensitive tomograph has to fulfill some conditions:

- a high efficiency detection for 511 KeV gamma rays,
- short coincidence resolving time,
- the ability to provide high spatial resolution (to be small),
- stability,
- reliability,
- low cost.

None of the scintillators available today satisfy all of these criteria.

The most important characteristics is the efficiency of detection, because in coincidence experiments the coincidence efficiency is:

$$\varepsilon = \varepsilon_1 \varepsilon_2 \qquad (4.1)$$

where ε_1, ε_2 represent the individual efficiency of each detector. Therefore, the coincidence efficiency is approximately the square of the individual one.

From this point of view, bismuth germanate (BGO) crystals are the best (Table 2.6), but their inferior time resolution causes larger accidental rates and great dead times. Cesium fluoride CsF and barium fluoride BaF_2 are much lower in efficiency but are fast enough even for time of flight (TOF) measurements. Cerium gadolinium orthosilicate(GSO) is a new material that is 5 times faster than BGO with almost its efficiency and it has twice its light output.

Time of flight (TOF) information.

The time of flight technique improves the sensivity of the tomograph and data quality by improving the localization of information along the line between detectors.

For the positioning of the annihilation event, the coincidence detection of the annihilation radiation utilizes only one property of the annihilation radiation, namely the colinearity of the travel of the two annihilation photons. The coincidence line is established with the assumption that the two annihilation photors reach the detector in the same time.

Another property of the annihilation event can be utilized in PET: the fact that the two annihilation photons are emitted simultaneously as annihilation occurs. Under these circumstances, the two photons arrive in the same time at the detectors only if the annihilation event is equidistant from the two detectors. The difference between the time of arrivals of the two photons gives the position of the event relative to the centre of the coincident line joinig the two detectors (Fig. 4.3)

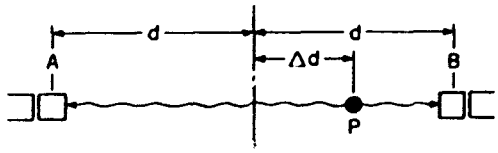

Fig. 4.3 *Diagram illustrating the principle of time of flight* (TOF) *method.*

The distances from the point of the annihilation event to the detectors are:

$$PA = d + \Delta d \tag{4.2}$$

$$PB = d - \Delta d \tag{4.3}$$

That means:

$$PA - PB = 2\ \Delta d \tag{4.4}$$

The difference in time between the arrival of the two photons at A and B is:

$$\Delta t = \frac{2\ \Delta d}{c} \tag{4.5}$$

where c is light speed.

If the time of arrival is measured, then additional information can be derived, the position of the annihilation event between the two detectors.

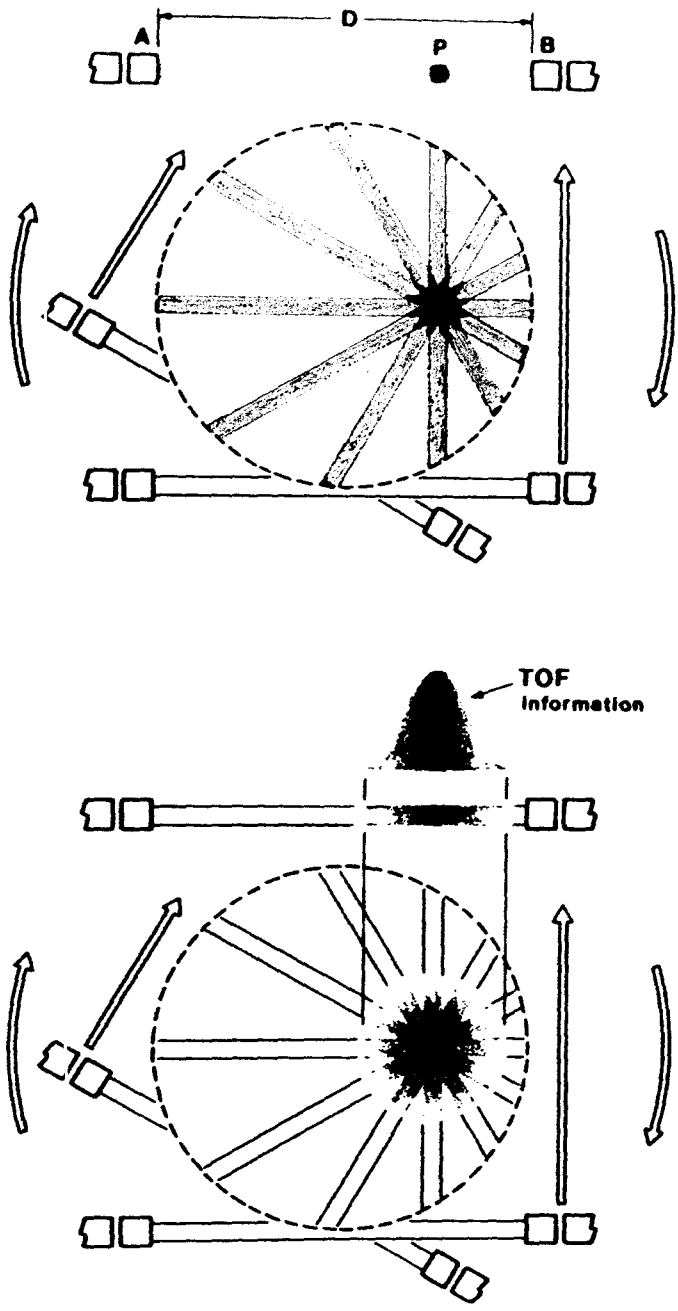

Fig. 4.4 *Qualitative illustration of signal-to-noise gain achieved through the incorporation of photon TOF information.*

For an annihilation event distant by 15 cm from the centre, the difference in time of arrival is approximately 1 nsec. In PET devices, this difference in time of arrival is usually much smaller than the coincidence window. With modern fast electronics and detectors such as CsF and BaF_2, the timing resolution which can be achieved is typically of the order of 400 psec, which corresponds roughly to a positioning accuracy of about 6 cm FWHM.

Although this poor resolution might appear to be of little use in PET imaging, it should be noted that "a priori" information as localization of the annihilation event, increases substantially the signal-to-noise ratio in the reconstructed image (Fig. 4.4). [26] Typically, for an object approximately 30 cm in diameter and a timing resolution of 500 psec, the gain in signal-to-noise ratio is approximately a factor of three.

4.2.2 Systematical factors.

Positron Emission Tomography data are subject to a few major systematic errors.

A. Attenuation of the annihilation photons in tissue.

The correction for attenuation of PET data are important when quantitative evaluations should be made. [27] The correction methods that are in practical use are:

- direct measurements of attenuation with external positron sources,
- calculations from simple geometric shapes that approximate the attenuation medium,
- delineation of the object's extent from the reconstruction image and using weighing factors proportional to path length of γ-ray.

The measured projection values $p_m(r,\phi)$ are related to unattenuated projection $p(r,\phi)$ (eq. (3.2)) by the following equation:

$$p_m(r,\phi) = p(r,\phi)\ p_\mu(r,\phi) \tag{4.6}$$

where,

$$p_\mu(r,\phi) = \exp\left(-\int_{r,\phi} \mu(x,y)\ ds \right) \tag{4.7}$$

and $\mu(x,y)$ is the attenuation coefficient. This $p_\mu(r,\phi)$ term is called the attenuation correction factor.

If the value of $p_\mu(r,\phi)$ or $\mu(x,y)$ is known, $p(r,\phi)$ can be calculated in terms of the attenuated projections as:

$$p(r,\phi) = \frac{p_m(r,\phi)}{p_\mu(r,\phi)} \qquad (4.8)$$

and the distribution f(x,y) can be reconstructed accurately.

Since a large number of combinations of isotope distributions and attenuation conditions are encountered in PET, it is very difficult to evaluate all the different errors in the application of eq. (4.8) for attenuation corrections.

B. Background events due to accidental coincidences.

The PET detection system registers a "coincident" event if both detectors are triggered within the coincidence resolving time. Since there will be many unrelated photons striking the detectors, there will be pulses giving false or accidental coincidences (Fig. 4.5).

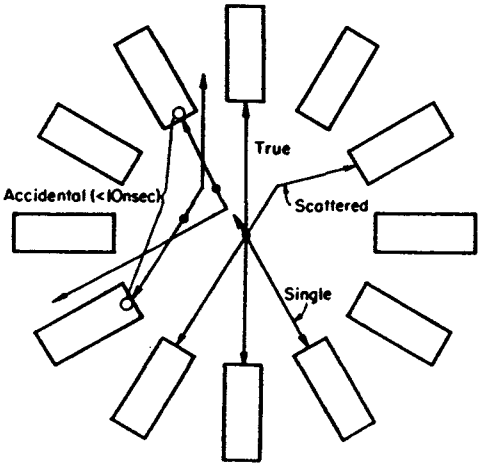

Fig. 4.5 *Types of positron annihilation events:*
- *true coincident events,*
- *scattered coincident events,*
- *accidental events.*

The accidental count rate is given by:

$$R_A = 2\tau R_1 R_2 \qquad (4.9)$$

where 2τ is the resolving time and R_1 and R_2 are the singles count rates on the two detectors. It should be noted from the above equation that, while the number of true coincidences recorded increases linearly with the amount of radioactivity, the number of accidental coincidences increases as the square of that value.

The number of single events sensed by detectors operated in coincidence is, in most PET examinations, at least two orders of magnitude greater than the number of "true" coincidences. It is because of this preponderance of single counts compared to coincidence events that the presence of random coincidences represent a troublesome source of noise.

Three methods are generally used to minimize the influence of random coincidences:

- operation of the coincidence system at relatively low counting rates R_1 and R_2,
- reduction of coincidence resolving time (2τ). The resolving time cannot be made arbitrarily small. It must bear some relation to the intrinsic time jitter of electronics and detectors or there will be a loss of true coincidence events if 2τ is too small, or too many accidental events if 2τ is too large.
- subtraction of the contribution of random coincidences obtained by the measurement of the single rates in each of the detectors operated in coincidence, or by direct measurement of the contribution of accidental counts to the detected events. Delaying the system by a time greater than 2τ, the count rate observed is due to accidental coincidences. [28]

C. Background events due to prompt scatter.

Scatter and accidental coincidences are the two primary sources of background counts in PET imaging.

Scatter coincidences occur when one or both of the annihilation gamma rays is scattered. A scatter coincidence will occur when both of these gamma rays strike detectors connected in coincidence, because the scattered gammas are still in true time coincidence with each other (Fig. 4.5). After scatter, the spatial information of the point of annihilation gamma-ray emission is "misplaced" and the resulting background is uncorelated with the isotope distribution in the cross section.

At 511 KeV, the most probable scatter is a small angle scatter and in terms of system geometry the gamma rays that are most likely to be detected are scattered less than 30^{o}.

A 511 KeV gamma rays is reduced only to 450 KeV after a 30^{o} scatter. Therefore, unlike low energy gamma ray imaging, energy discrimination is not effective in greatly reducing the number of unwanted scatter coincidences. In addition, scatter background can come from off plane activity.

However, most of the scattered events represent true coincident events caring information. In order to detect them, in the PET devices each detector operates in coincidence with a number of detectors on the opposite side (Fig. 4.6).

The ratio of scatter to true coincidences depends on the activity distribution, thickness of the imaged cross section and the geometry of the PET system.

The correction for unwanted scattered events in PET is difficult. It is possible to get an accurate measure of scatter that can be used as a data base for scatter corrections. [22, 29]

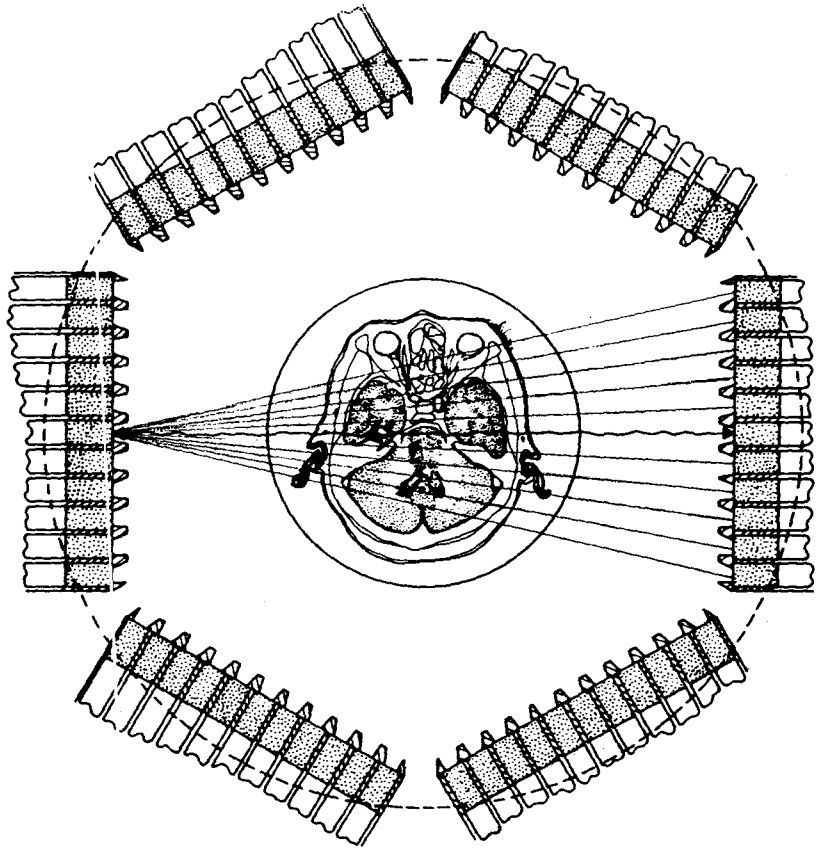

Fig. 4.6 *Ray path indicating possible coincidences between opposed detectors.*

Using a line source of a positron emitter placed in the scattering medium, the scatter is determined from the scan profiles, not the image. The scatter is the tail of activity on each side of the peak (Fig. 4.7). Relative to the peak of line source, the scatter is less than one procent at any single point, but integrated over the Field of View (FOV) the amount of scatter becomes significant.

The average value of the scatter fraction obtained can be used to correct the data. [22] In another ways, the shape of the scatter may be expressed analytically, and consequently subtracted from the image, or to deconvolve the scatter. [29] Deconvolution procedure for scattering uses the line spread function in the raw projection as the basis for a scatter filter which operates on the patient data set prior to back-projected.

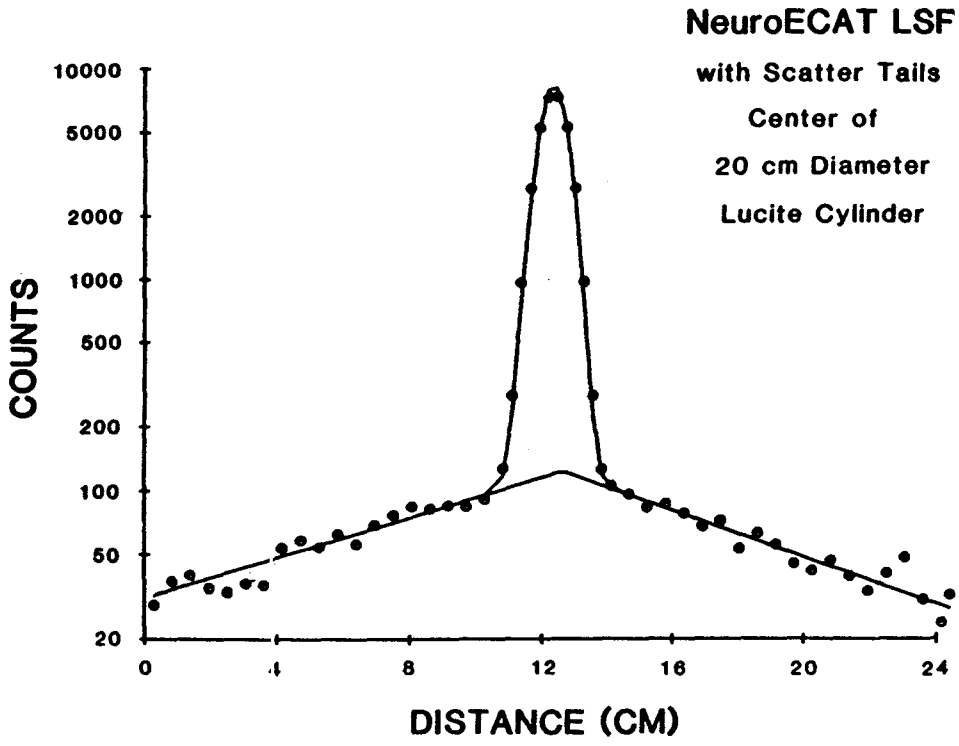

Fig. 4.7 *The distribution of the events versus distance for a line source in a scattering medium.*

D. Limited resolution.

Effect of object size on quantitation.

In PET, spatial resolution can affect the capability of quantitatively measuring isotope concentration when the object of interest is smaller than the FWHM of the system. [30] In this case there is no longer a linear relation between the image and the true isotope concentration.

The problem of detectability with size is obvious as the smallest cylinder in Fig. 4.8 is not visible in the image, the second smallest is just barely detectable. The isotope concentration in each cylinder in the phantom was identical and the apparent concentrations in the image of the smaller cylinders are obvious different from the larger cylinders.

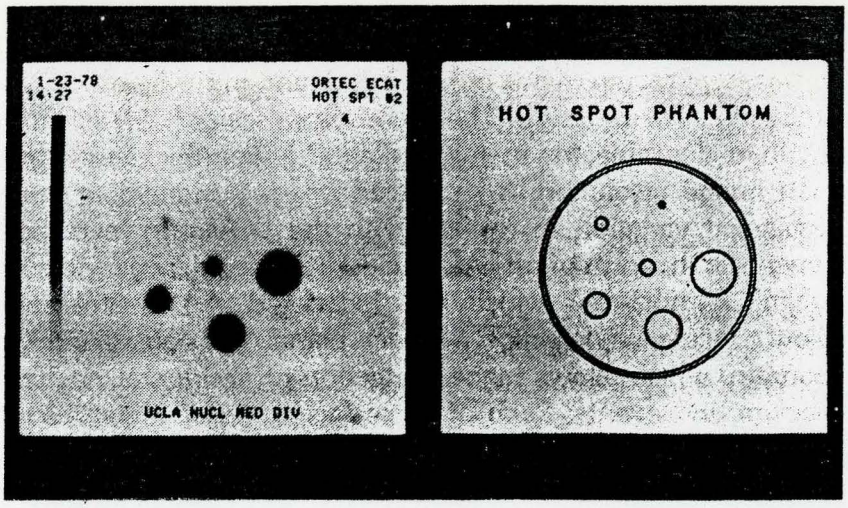

Fig. 4.8 *Effect of object size on quantitation in* PET. *Image to the left is of phantom presented on the right. Each inside cylinder contains identical concentration of positron emitter. The image demonstrates the loss of information due to the limited resolution of* PET.

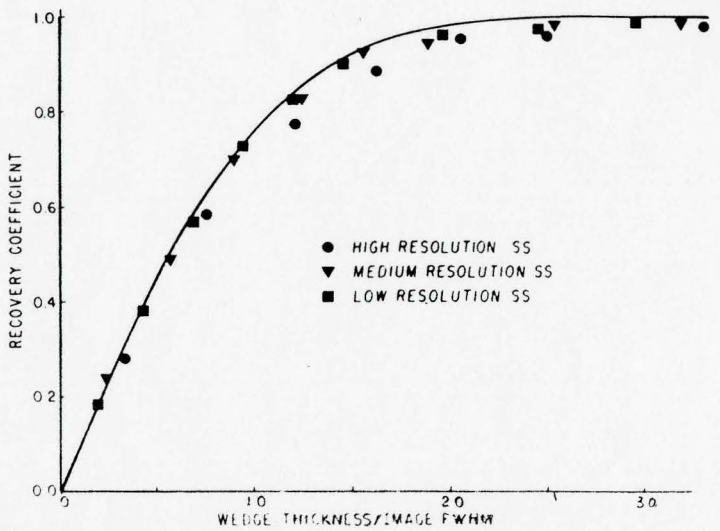

Fig. 4.9 *Plot of recovery coefficient versus bar thickness. The bar thickness is given in multiples of the system resolution.*

The magnitude of the errors in quantitation can be appreciated from the graph presented in Fig. 4.9. [30] This figure shows a plot of the *recovery coefficient* RC versus bar phantoms of various thickness. The recovery coefficient RC is defined as the ratio of the isotope concentration observed in the image and the true isotope concentration. If the RC = 1.0 the system is quantitative for an object of these size. The solid line in the graph assumes a Gaussian line spread function (LSF) and is the theoretical response of an ideal system.

Partial volume effect.

The partial volume effect is the loss of contrast in an image because the axial dimension of the object is smaller than the axial resolution of the imaging system. [30] This source of error can be eliminated by using objects that are larger than the axial resolution of the system.

The obvious solution to improving the difficulties of suboptimal resolution is to build a higher resolution PET system.

Non-uniform resolution.

One of the primary reasons that coincidence detection of annihilation radiation is so well suited for emission computed tomography is its relatively constant resolution as a function of depth. The uniform resolution and constant sensivity as a function of depth of annihilation coincidence detection provide a data set uniquely consistent with the assumptions of the reconstruction mathematics.

As the field of PET developed, many investigators found that the system exhibit variations in resolution as a function of position in FOV (Fig. 4.2). [31]

There are several sources for these nonuniformities. The intrinsic variation of resolution of a coincident detector pair is a primary source of resolution nonuniformity. Experiments [31] show that the variation in resolution is more serious when the detectors are brought too close together. Consequently, the use of the large system diameter is the primary factor in producing good uniformity in the axial resolution, but in the same time the sensivity of the tomograph decreases.

Another source of nonuniformity is the penetration of a detector by a γ-ray and its detection by a neighboring detector.

This causes an error in the apparent position of the source and a broadening of the line spread function. This effect is important for PET systems with small detectors.

Nonuniform resolution is primarily concern to the physicist who is attempting to do quantitative measurements.

E. Losses due to dead time.

There are multiple sources of dead time losses in a device as complex as a Positron Emission Tomograph system.

First of all, dead time losses include the time constant of the detector and analog electronics for timing and energy discrimination.

Dead time losses in single events in detectors will reduce the number of coincident events since a fraction of these losses have been true coincidences. Typically, the net dead time per event per detector is determined assuming a nonparalizable dead time for the system:

$$\tau_d = \frac{1}{R_o} - \frac{1}{R} \qquad (4.10)$$

where R_o and R are the observed and true counting rates respectively. The effective dead time τ_d of the system is obtained by averaging the data for a number of individual detectors.

Since the two detectors must be ready to take data for a coincidence, the probability that both detectors are live is:

$$P = 1.0 - \tau_d \qquad (4.11)$$

In processing coincident events, a PET system requires that only events occurring simultaneously within the coincidence resolving time of the system are accepted.

When multiple events are detected within that time window, the data are usually rejected to avoid the wrong location of the event. This loss of data occurs both in the true and accidental coincident events.

All PET systems have some dead time due to the requirement of placing the data on a temporary storage device during the scan. The correction for this data loss depends on the details of the system design.

Although each type of dead time becomes significant at high rates, they are somewhat independent and the total dead time depend on the combination of count rate, system design, source distribution and scatter geometry of each set of image data. [32]

4.2.3 Limitations in spatial resolution.

It may appear that the spatial resolution achievable by means of electronic coincidence collimation would depend only on the dimensions of the detectors used. In fact, the spatial resolution of this method of detection is limited by physical factors and even design factors.

A. Positron range.

As mentioned before, often positron undergo annihilation only after losing most of their kinetic energy in matter. Thus, the position of the annihilation event is not coincidental with the position of the nucleus undergoing radioactive decay. This uncertainty depends on the energy of the positrons and on the density of the matter where the annihilation event takes place.

The accurate measurements of the positron annihilation distributions show a bright centre and extensive tails. The resulting FWHM are very small (<1 mm) and 90% of the annihilations lie beyond this distance. [14]

A method for mathematically removing this blurring factor from the image is given in [33].

B. Deviation from 180^{o} emission.

The two annihilation photons are usually not emitted collinearly. The positron-electron pair (positronium) has a random energy of typically 10 eV at the instant of the annihilation.

The divergence from colinearity results from momentum conservation requirements. This divergence depends on physical characteristics of the absorber while the annihilation event takes place.

Measurements of the angular distribution of annihilation photons in water at 20^{o} show a nearly a Gaussian distribution with a FWHM of 0.5^{o} (5.7 mrad). [10, 14] This contributes 0.9 mm FWHM at the centre of a 60 cm diameter ring.

This blurring factor is not easily removed mathematically and represents the most important physical limitation to spatial resolution in PET.

C. Crystal-photomultipliers coupling.

The primary difficulty in designing a tomograph with a good spatial resolution (at least 2 mm FWHM) lies not in the range of the positrons, nor the deviation from 180^{o} emission, nor the detection properties of small BGO crystals, but in the size of available photomultipliers.

Several approaches to achieve a spatial resolution finer than the size of the photomultiplier include:

- choosing a detector configuration which allows that each BGO crystal being individually coupled to a phototube (Fig. 4.10). [34] The BGO crystals have three different shapes, depending on the orientation of the associated phototube. Since the phototube is coupled to 3 sides of the crystal array, this approach is limited to a single ring geometry.
- incorporating many small electron multipliers and anodes within a single glass envelope. This is a solution to the problem of dead space taken by the glass walls.
- coupling small, close-packed crystals to larger phototubes (Fig. 4.11). [24]

  In this case, each photomultiplier is optically coupled to three crystals, sharing the outside crystals with the neighboring photomultipliers and viewing the central crystal alone. The crystal of interaction is identified by a simple coding scheme in which the central detector is identified by signals from single photomultipliers and the shared or outside crystals identified by signals from two adjacent photomultipliers.

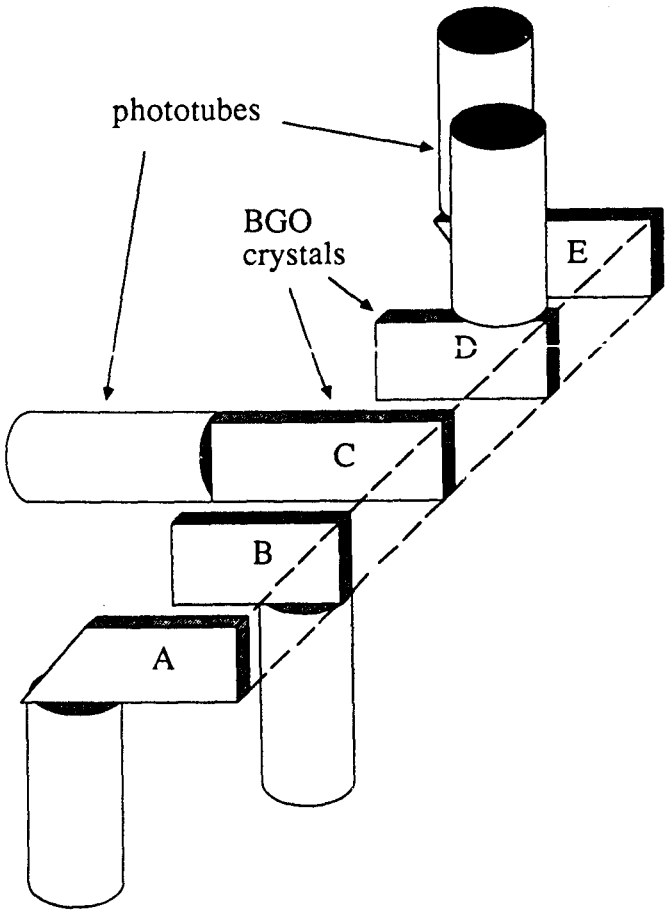

Fig. 4.10 *Sketch of a detector-phototube possible configuration.*

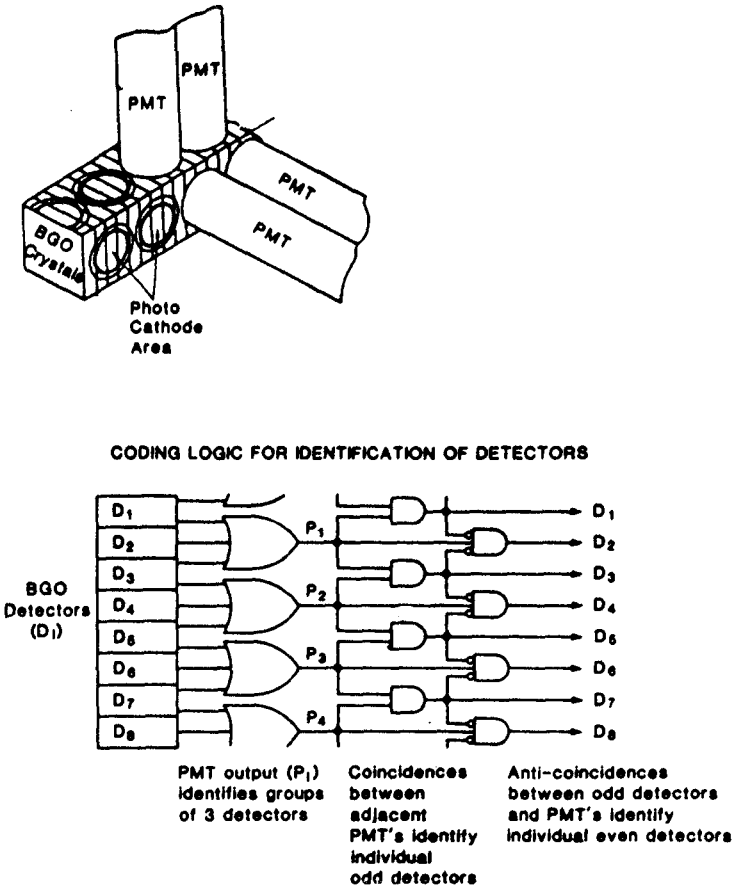

Fig. 4.11 *Diagram of another possible coupling crystal-phototube. The possible physical arrangement and possible logic scheme to identify the crystal, are indicated.*

Modern PET designs employ many small BGO crystals closely packed and coupled to a position-sensitive photomultiplier tube. [35-38] For this system, the dead time and are of special concern.

- using small solid state photodetectors, promising results were obtained with HgI_2 crystals and Si photodiodes. [15, 39] These small photodiodes gave a good pulse height resolution (up to 7.2% FWHM for 662 KeV photopeak at -150^{o}) but with a poor timing accuracy. To overcome this limitations, one promising approach uses:
- a photomultiplier combined with solid state photodetectors (Fig. 4.12). [10, 13, 39, 40]

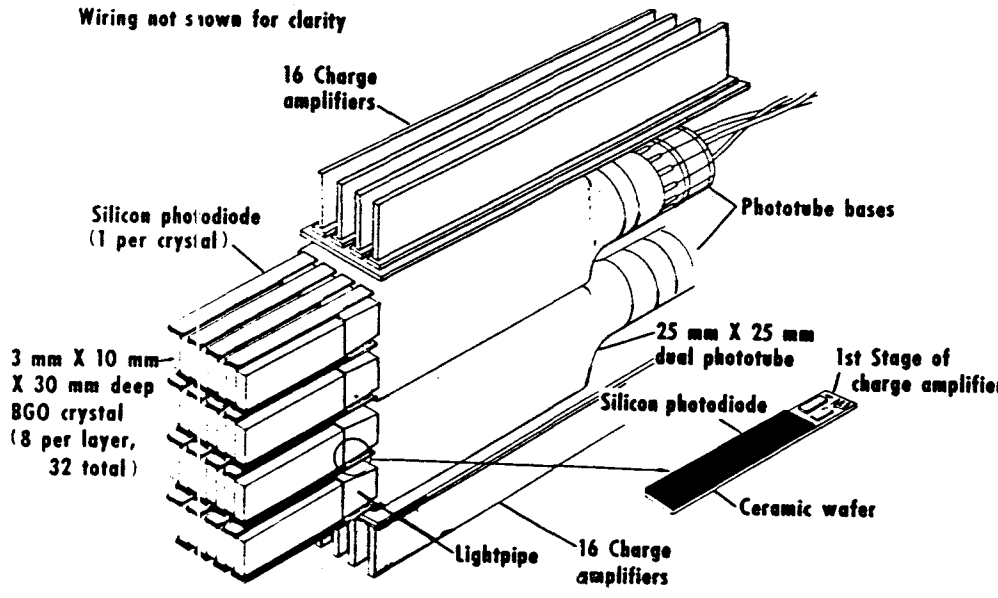

Fig. 4.12 *Multiring detector array where groups of 8 crystals are coupled to a common phototube for timing information and coupled individually to silicon photodiodes for the identification of the crystal of interaction.*

A group of crystals is coupled to a relatively large photomultiplier tube which determines the timing for the group The solid state photodiodes are coupled individually to each crystal to determine the identity of the scintillating BGO crystal.

D. Other factors.

Between the spatial resolution limitations, the motion of the organ under study has to be taken in consideration. The motion of the head can be kept to within 1 mm during a short ($\approx$ 1 min) imaging time in favorable cases. The motion of the heart is far greater and a blur of 2 mm is possible even when gutting for both the beating of the heart and the motion of the breathing.

Finally, in the reconstruction procedure, the filter used has to be determined by the system resolution not by statistical fluctuations to avoid the deterioration of the spatial resolution of the system.

4.3 Statistical properties of the reconstructed image.

The qualitative as well as quantitative ability of PET is critically dependent on the statistical uncertainty (i.e. noise) in the reconstructed image. Unfortunately, such uncertainty is far grater than if it were distributed according to Poisson statistics expected from simple considerations of the number of events recorded from each resolution cell (eq. (3.58)).

Based on the results of 60 experiments, the authors [42] derived the root mean square (rms) uncertainty in the number of events for an uniform source as:

$$\begin{aligned} &\text{rms\% uncertainty} = \\ &= 120 \times (\text{nr. resol. cells})^{3/4} \times N^{-1/2} \end{aligned} \tag{4.12}$$

where N is the total number of events measured. The value 120 in eq. (4.12) may be altered by the convolution kernel used.

The increased statistical fluctuation is due to the propagation of errors in the reconstruction process. [42] For example, if the average number of reconstructed events is 400 per resolution cell, one might expect the rms uncertainty to be 5%. However, the rms uncertainty is about 44% for a circular region of uniform activity (Fig. 4.13).

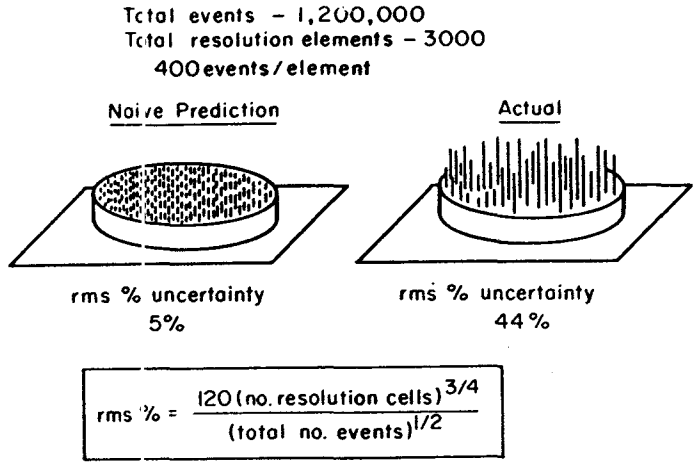

Fig. 4.13 *Calculations of root mean square (rms) statistical uncertainty in the number of events for an uniform disc of activity.*

Fig. 4.14 presents the relation between the total number of counts required to be detected and the number of resolution cells per different rms uncertainty. [42]

For 10 mm resolution imaging, we should require about 200000 events for images of the head (20 cm diameter) to achieve a diagnostic quantitative accuracy for rms uncertainty of 10%.

Equation (4.12) does not hold for situation of nonuniform distribution of activity, when most of the activity lies in 20- 30% of the resolution elements. A reduction of the expected errors occurs in this case because the rms uncertainty decreases as the fraction of the image occupied by the object decreases. In addition, uncertainty decreases as the contrast increases.

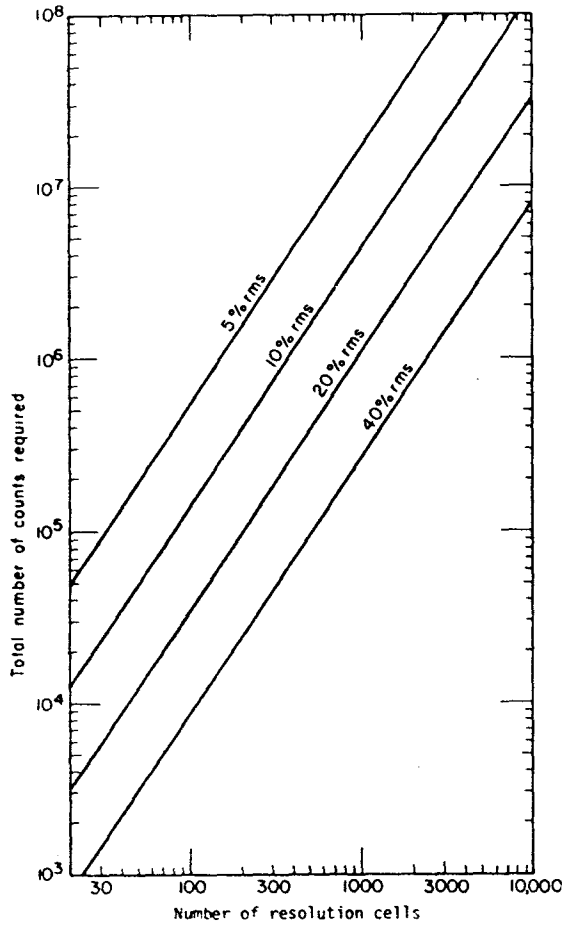

Fig. 4.14 *Predicted statistical uncertainty as a function of effective number of resolution cells and total number of detected events.*

To predict regional uncertainties under various conditions of contrast (signal-to-noise ratio) and distribution of activity, the strategy applied in [42] is to reduce the effective number of resolution cells, M_e:

$$\text{rms\% uncertainty in } n = \approx 120 \times (M_e)^{3/4} \times N^{-1/2} \tag{4.13}$$

where n_t is the number of events per target resolution cell, N is the total number of events measured and M_e is related both to the contrast and to the percent of the total image occupied by the object.

The effective number of resolution cells, M_e will be the number of cells in the target plus some contribution from the cells in the background. The background contribution is estimated by weighing the number of background cells by the ratio of the background concentration to the target event concentration:

$$M_e = M_t + \frac{n_b M_b}{n_t} = M_t + \frac{M_b}{C} = \frac{M_t n_t + n_b M_b}{n_t} = \frac{N}{n_t} \qquad (4.14)$$

where M_t is the number of target cells, M_b is the number of background cells, n_b is the number of events per background resolution cell and $C = n_t/n_b$ is the contrast. Then:

$$\text{rms\% uncertainty in } n_t = 120 \left(M_t + M_b/C\right)^{3/4} N^{-1/2} \qquad (4.15)$$

or,

$$\text{rms\% uncertainty in } n_t = 120\, N^{1/4} n_t^{-3/4} \qquad (4.16)$$

Equations (4.15) and (4.16) give the required number of events to obtain an image in the limits of a desired uncertainty:

$$N = \left\{ \frac{120}{\text{\% uncertainty}} \right\}^2 \left(M_t + M_b/C\right)^{3/2} \qquad (4.17)$$

For example, assume that a transverse section of the heart occupies $M_t = 70$ cells from the total of 700 cells, and the contrast is 4 : 1. To achieve an uncertainty of 20%, the required number of events is:

$$N = (120/20)^2 \times (70 + 630/4)^{3/2} = 124000 \text{ events} \qquad (4.18)$$

4.4 Quantitative evaluations with PET.

There are three general categories of imaging associated to emission computed tomography: static imaging, equilibrium imaging and dynamic imagirg, and three models correspondingly. [44]

4.4.1 Static models.

A static imaging situation is available when a steady state (constant concentration) is reached. In static imaging, the constant (more or less) distribution of a radiotracer accumulated in tissue is examined.

This method is applied to imagine the accumulation of a radiotracer in an organ or in a tumour.

Specific physiological properties such as flow and glucose utilization can be deduced from the quantitative data of static images using tracer kinetics models. These tracer kinetics mathematical models are necessary to derive numerical values of physiological processes from the PET data, that is, to translate measured concentrations of radiopharmaceuticals into biologically significant values. A prototype of this approach is the FDG method for estimating the rate of cerebral glucose utilization. [43]

The brain utilizes glucose almost exclusively as its energy source under normal conditions. Measuring the rate of glucose utilization in the brain therefore provides an index of brain function.

The most direct PET approach to this measurement is to label glucose with a positron emitter as ^{11}C. One problem with this technique is the rapid metabolic degradation of glucose, resulting in labeled glycolytic intermediates that are different to model kinetically.

The deoxyglucose (DG) method does not suffer from this limitation and is now the most widely utilized method of measuring glucose utilization in vivo. First ^{11}CDG was used and then ^{18}FDG.

Fluorodeoxyglucose and DG are transported from blood to brain across the blood-brain barrier (BBB) analogously to glucose and both are phosphorylated by hexokinase (the first step in glycolysis) to deoxyglucose-6-phosphate (DG-6-PO_4) and fluorodeoxyglucose-6-phosphate (FDG-6-PO_4), respectively. Neither DG-6-PO_4 nor FDG-6-PO_4 is metabolized further through the glycolitic pathway to any significant degree, and they are trapped in the tissue because they cannot diffuse through cell membranes. This metabolic trapping facilitates imaging with PET and simplifies the tracer kinetic model.

The enzyme that probably catalyzes the dephosphorylation of FDG-6-PO_4 and DG-6-PO_4 as well as glucose-6-PO_4 (glucose-6-phosphotase) is present in low but measurable quantitaties in the normal brain. In humans, where scanning is performed over long time intervals, the dephosphorylation reaction should be taken into account in the model.

The FDG model is composed of three compartments (Fig. 4.15): FDG in plasma, FDG in tissue, and FDG-6-PO_4 in tissue. The first order rate constants k_1^* and k_2^* describe forward and reverse transport of FDG from plasma to the brain across the BBB and k_3^* and k_4^* describe phosphoarylation and dephosphorylation of FDG and FDG-6-PO_4 respectively. The rate constants k_1, k_2, k_3 and k_4 are the corresponding terms for glucose and glucose-6-PO_4.

Under steady state conditions (i.e. constant rate of glucose utilization) the rate of phosphorylation of glucose is equal to the glycolitic rate (i.e. in a steady state, the rate of any one step in a process is equal to the rate of the overall process).

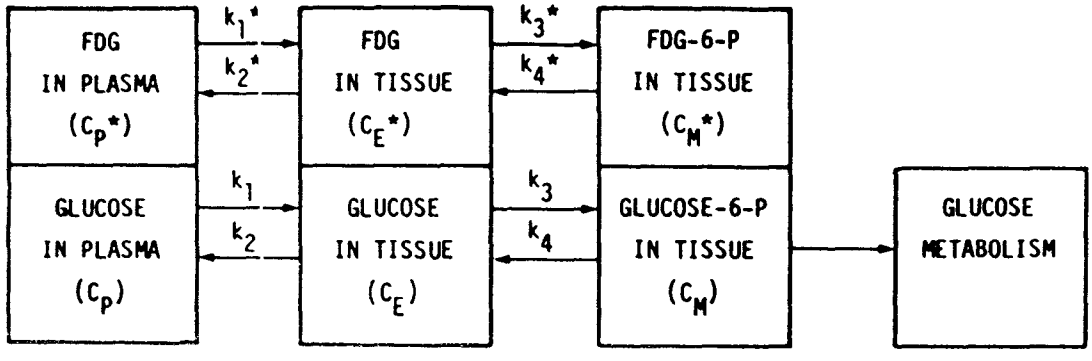

Fig. 4.15 *Three compartment* FDG *model.*

The operational equation for the four rate constant model is, [43]:

$$LCMRGlc = \frac{c_p}{(LC)} \frac{\left\{c_i(T) - \left[k_1^*/(\alpha_1-\alpha_2)\right]\left[(k_4^* - \alpha_1)e^{-\alpha_1 t} + (\alpha_2 - k_4^*)e^{-\alpha_2 t}\right\} * c_p^*(t)}{\left[(k_2^* + k_3^*)/(\alpha_2 - \alpha_1)\right]\left(e^{-\alpha_1 t} - e^{-\alpha_2 t}\right) * c_p^*(t)} \quad (4.19)$$

$$\alpha_1 = \left\{k_2^* + k_3^* + k_4^* - \left[(k_2^* + k_3^* + k_4^*)^2 - 4k_2^*k_4^*\right]^{1/2}\right\} / 2$$

$$\alpha_2 = \left\{k_2^* + k_3^* + k_4^* + \left[(k_2^* + k_3^* + k_4^*)^2 - 4k_2^*k_4^*\right]^{1/2}\right\} / 2 \quad (4.20)$$

where: LCMRGlc, or CMRGlc when referring to a global as compared to a local value, is the cerebral metabolic rate of glucose, usually given in milligrams or micromoles per minute per 100 g,

c_p is the plasma concentration of glucose,

$c_i(T)$ is the tissue concentration of FDG + FDG-6-PO_4 at time of measuring T (the means counts in a given region of interest on the image),

k_1^*, k_2^*, k_3^* and k_4^* are the rate constants,

$c_p^*(t)$ is the plasma FDG concentration as a function of time after injection of FDG,

LC, the lumped constant corrects for the difference between FDG and glucose for transport and phosphorylation.

The symbol * denotes the operation of convolution.

In words, the FDG model may be expressed as:

$$\left\{\begin{matrix}\text{Local glucose} \\ \text{metabolic rate}\end{matrix}\right\} = \left\{\frac{\text{Plasma glucose}}{\text{Lumped constant}}\right\} \times \frac{\left\{\begin{matrix}\text{Total } ^{18}\text{F} \\ \text{in region}\end{matrix}\right\} - \left\{\begin{matrix}\text{Free } ^{18}\text{F-FDG} \\ \text{in region}\end{matrix}\right\}}{\left\{\begin{matrix}\text{Total } ^{18}\text{F-FDG concentration} \\ \text{transported to the region}\end{matrix}\right\}}$$

The performance of an FDG study requires the administration of 5-10 mCi FDG intravenously and the measurements of tissue activity $c_i(T)$, the plasma concentrations of FDG and glucose as well as knowledge of the rate constants k_1^*, k_2^*, k_3^* and k_4^* and lumped constant.

To implement the model, predetermined values for these rate constants from normal subjects were used giving reliable estimates of CMRGlc within a wide range of metabolic rates. In extremes of metabolism (hyper or hypo metabolic rates) these predetermined rate constants can lead to errors.

4.4.2 Equilibrium models.

In the equilibrium imaging, a radionuclide is injected or inhaled at a constant rate until a steady state is reached in the volume of interest.

An interesting relation between perfusion and detected activity can be derived for the case of constant administration of short-lived radionuclides until steady state or equilibrium is reached. In this case, the rapid decay of tracers effectively removes the activity from recirculation and the method is applicable to determine the flow. The equation relating the change in amount of activity to input, output and decay is:

$$\frac{dq(t)}{dt} = F\ A(t) - \frac{F}{V}\ q(t) - \lambda\ q(t) \qquad (4.21)$$

where q is the amcunt of activity in the region of interest, F is the flow into that region, A(t) is the concentration of tracer input to q(t), F/V is the specific volume flow out of the region and λ is the physical decay rate constant.

At equilibrium:

$$F\ A - \frac{F}{V}\ q - \lambda\ q = 0 \qquad (4.22)$$

and

$$q = \frac{F\ A}{F/V + \lambda} \tag{4.23}$$

where A and q are the values of A(t) and q(t) at equilibrium.

If the half life is very short compared to the mean transit time τ, i.e:

$$\lambda >> F/V = 1/\tau \tag{4.24}$$

then,

$$q = F\ A/\lambda \tag{4.25}$$

and

$$F = \lambda\ q/A \tag{4.26}$$

There are two kinds of tracers, diffusible tracers for which the tissue permeability is great, and extractable tracers which are extracted from perfusate.

For diffusable tracers like $H_2{}^{15}O$, the eq. (4.22) can be written:

$$F\ (A - q/V) = \lambda\ q \tag{4.27}$$

Noting that q = C x V, where C is the tissue concentration:

$$F = \lambda\ C\ V/(A - C) \tag{4.28}$$

or,

$$F/V = \lambda\ (A/C - 1) \tag{4.29}$$

Thus, flow can be determined if we have a means of measuring the input concentration A and the tissue concentration C.

For an extractable tracer, the condition of steady state (eq. (4.22)) becomes more complicated. It is assumed that the tissue of interest has two kinetic components: a rapidly perfusing component and a more slowly exchanging component represented by the fractional loss of tracer from the intracellular pool.

For example, the amount of ^{82}Rb injected into the coronary capillaries which is available for rapid perfusion is (1-E) where E is the extraction ratio (E is assumed to be constant). Then, eq. (4.21) is modified in:

$$\frac{dq(t)}{dt} = F\,A(t) - F\,A(t)(1 - E) - \gamma\,q(t) - \lambda\,q(t) \qquad (4.30)$$

where γ is the slow turnover of the extracted ^{82}Rb from the system per unit time. At equilibrium:

$$F = (\gamma + \lambda)\,q/(E\,A) \qquad (4.31)$$

But the fractional loss of potassium analogues as ^{82}Rb is very small relative to the rate of decay $\lambda = 0.55\ min^{-1}$ thus,

$$F = \lambda\,q/(E\,A) \qquad (4.32)$$

which is similar to eq. (4.26) except of the presence of the extraction ratio E.

For estimating myocardial flow, quantitative information from volume of interest must be obtained using PET.

4.4.3 Dynamic models.

The positron emission tomography method gives the possibility to measure the moment-to-moment change in the distribution of tracers in the organs of interest after an impulse (bolus) injection.

Examples of medical studies are rapid intravenous injection of radionuclide such as ^{82}Rb or ^{68}Ga or inhalation of a gas such as ^{77}Kr or $C^{15}O_2$. In the case of inhalation, the tracer which arrives in the carotid arteries on its way to the brain has an activity distribution versus arterial time that is not a simple impulse response but a variable arterial input. The same is true for rapid intravenous injection as the bolus traverses through the venous system to the right heart, the lungs and back to the left heart before entering the body's vascular system. If we know this distribution and assume a simple wash-out model, then the flow and the permeability can be deduced.

The principle of conservation of material gives:

$$\frac{dq(t)}{dt} = F\ [A(t) - B(t)] \tag{4.33}$$

where dq/dt is the change of quantity in the organ or tissue in time, F is the flow and A(t) and B(t) is the concentration activity of the input and output respectively. Equation (4.33) is known as the Fick Principle.

If we define a partition coefficient:

$$p = \frac{q(t)/V}{B(t)} \tag{4.34}$$

which is the ratic of concentration of a substance in tissue q(t)/V to the concentration of the substance in blood B(t), then the equation (4.33) can be expressed:

$$\frac{dq(t)}{V\ dt} = \frac{F}{V}\ [A(t) - B(t)] \tag{4.35}$$

$$\frac{dq(t)}{dt} = \frac{F}{V}\ \left[A(t) - \frac{q(t)}{V\ p}\right] = \frac{F}{V\ p}\ \left[p\ A(t) - \frac{q(t)}{V}\right] \tag{4.36}$$

The solution of this differential equation is:

$$\frac{q(t)}{V} = \frac{F}{V}\ \exp\left(-F/(p)\right) \int_o^t A(t)\ \exp\left(\frac{F}{V\ p}\ \tau\right)\ d\tau =$$

$$= p\ K \int_o^t A(\tau)\ \exp\left(-K\ (t - \tau)\right)\ d\tau \tag{4.37}$$

where K = F/(pV)

This equation can be used to determine the flow if the concentration on the arterial input side is a measursble variable and there is no recirculation. An example of application is injection of a diffusible substance into left atrium of heart.

Then, the aortic concentration of the tracer is the input function A(t). Measuring $A(\tau)$ in time one can find which flow value best matches the tissue uptake q(t)/V at a particular time.

For measured arterial concentration curve, we can calculate the expected tissue concentration as a function of time and specific volume flow by finding the best fit to the measured data.

Dynamic imaging has the possibility to determine the membrane ion transport and kinetic rate constants required for accurate understanding of metabolism and other biological functions of humans.

5. EXPERIMENTAL PROCEDURE.

5.1 McMaster Tomograph.

The McMaster Positron Emission Tomograph [45] was designed in a circular geometry. It is used for brain studies.

The 53.5 cm diameter gantry supports 160 Bismuth Germanate (BGO) crystals, each coupled to a 12.7 mm photomultiplier tube, and the associated electronics. The gantry can be tilted ± 20^{o} for a favorable imaging. The individual crystal dimensions are 10 mm wide, 25 mm high and 45 mm deep. Adjacent crystals are not separated by high atomic number inserts. Each crystal is coated with reflective paint, providing a typical separation between crystals of 0.5 mm and a packing fraction of 95%.

An annular collimator, 32 cm inside diameter, 52 cm outside diameter, is placed between the face of the crystals and the patient's head to reduce the number of accidental coincidences. The detected signals are then discriminated, events below 350 KeV are rejected. Adcitional circuitry determines the addresses of the two crystals whenever a valid coincidence occurs and sends them to a PDP 11/45 computer.

From all possible coincident rays, or line integrals of activity, 160 divergent projections are arranged each containing 61 rays, the other rays falling outside of field of view. Each line integral is corrected for relative efficiency of the detector pair and it is weighted by a factor proportional to its path length in the object, which represents an attenuation correction.

The filter used in the reconstruction is a Butterworth filter and the data are back-projected onto a 128 X 128 matrix, each pixel being 2 mm wide.

The spatial resolution obtained is 8 mm (FWHM) for the slice thickness of 10 mm.

The number of random coincidences was calculated with equation (4.9) using the total number of single events per detector and a resolving time of 13 nsec.

The sensivity of the tomograph was measured using a cylindrical lucite phantom 20 cm diameter and 20 cm long, filled with 1 μCi/ml solution of ^{68}Ge-^{68}Ga. The total number of coincident events was 18200 c/s for 1cm slice from which 2200 c/s were random coincidences, and 46500 cps for 2 cm slice from which 9100 cps were random coincidences. That is, at 6.3 mCi total activity, 12% and 20% random coincidences were registered for 1 cm and 2 cm thickness of slice, respectively. [45]

5.2 The phantom.

Since the accuracy is a measure of the difference between the observed value and the true value, the accuracy of a technique can only be determined in those cases in which the true value is determined by some independent method. Thus, the accuracy of a PET scanner method should be determined by measurements with test objects of known geometry and isotope concentration. The accuracy of in vivo data should be inferred from such measurements.

In this study, a cylindrical lucite phantom 25 cm diameter with a small cylinder inside (1.8 cm or 4.8 cm diameter) filled with water or a radioactive solution, simulates the brain tissue containing a tumour. Radioactive solution of different activity concentrations are used.

The experiments are done with hot tumours with, or without activity in nontumour region. Different tumour-to-nontumour activity ratios are studied in order to determine the accuracy of this new method of absolute quantitation in PET. A cold tumour, pure water in the tumour cylinder and radioactive solution in the phantom, is tested as well.

5.3 The positron emitters used.

Two kinds of β^+ positron emitters are used. The first one, ^{68}Ge-^{68}Ga has the advantage of a constant activity. These two isotopes are in secular equilibrium, the half life of the parent being much longer than the half life of the daughter. Most of the results are obtained using this solution.

Different measurements in human brain with PET use short lived isotopes. Particularly at McMaster Hospital, the studies using the tomograph are concentrated on brain abnormalities which were evidenced using ^{18}F labeled radiopharmaceuticals. [46, 47] Consequently, this method for absolute quantitation is tested for short lived isotope such as ^{18}F ($T_{1/2}$ = 110 min) and ^{64}Cu ($T_{1/2}$ = 12.7 h).

6. THE EXPERIMENTAL RESULTS IN TUMOUR'S DETECTION.

A tumour is an abnormal mass of tissue, the growth of which exceeds and is unconditioned with that of the normal tissues. It persists in the same excessive manner after cessation of the stimuli which evoked the change. [48]

To increase the understanding of cancer and to improve cancer treatment on a rational basis, the qualitative and quantitative differences between normal and neoplastic tissue must be identified. Positron Emission Tomography method should provide the quantitative information about the anomalous behaviour of tumour tissue.

One of the most important factors affecting the quantitative evaluations in PET is the statistics, that is, the total number of events detected per slice image. The short lived isotopes used in PET, the necessity of a minimum dose delivered to a subject under investigation and a total short time of measurement to the comfort of the patient, requires the knowledge of the minimum number of events per image that generates a reconstructed image reflecting the reality.

6.1 The distribution of the events in the image of a hot tumour without surrounding activity.

The simplest experiment consists of a hot tumour in a phantom filled with water. The 1 μCi/ml $^{68}Ge - ^{68}Ga$ solution in 1.8 cm and 4.8 cm diameter cylinders simulates the hot tumour. To study the effect of the number of events accumulated on the reconstructed image, different times of acquisition between 2 sec and 640 sec are chosen.

The reconstructed images of these two hot tumours show a circular form at high statistics measurements. As the time of acquisition is shortened, the image dimension of the tumour slightly diminishes and at very low statistics measurements ($t < 10$ sec), the image is deformed and presents star artifacts.

A horizontal line of one pixel thickness in the tumour region gives the distritution of counts as a function of distance expressed in numter of pixel (Fig. 6.1 and Fig. 6.2). The distribution of ccunts in the image of a small tumour (1.8 cm diameter) has Gaussian form (Fig. 6.1), unlike that of a bigger tumour (4.8 cm diameter) (Fig. 6.2). In both cases, the high statistics images are presented (640 sec time of acquisition).

When time of acquisition is 4 sec (Fig. 6.3) the tumour image is more difficult to separate from the star artifact background and its shape is deformed from the circular image.

The distribution of events in the image of the 4.8 cm diameter tumour, Fig. 6.2, presents a fall in the plateau region, giving an error $\leq$ 10% in the maximum number of counts evaluation. This effect is due to the attenuation correction introduced by a simple (weighing factors proportional to path length of γ rays) but very fast computational method.

In the reconstruction process the filter is the main factor responsible for the image background. To analyze the background, three regions of interest are chosen: 10 X 10 pixels, 20 X 20 pixels and 40 X 40 pixels. The average number of counts per pixel obtained from these three ROI agreed in the statistical limits. Usually, the value from 40 X 40 pixels ROI is used to minimize the statistical errors.

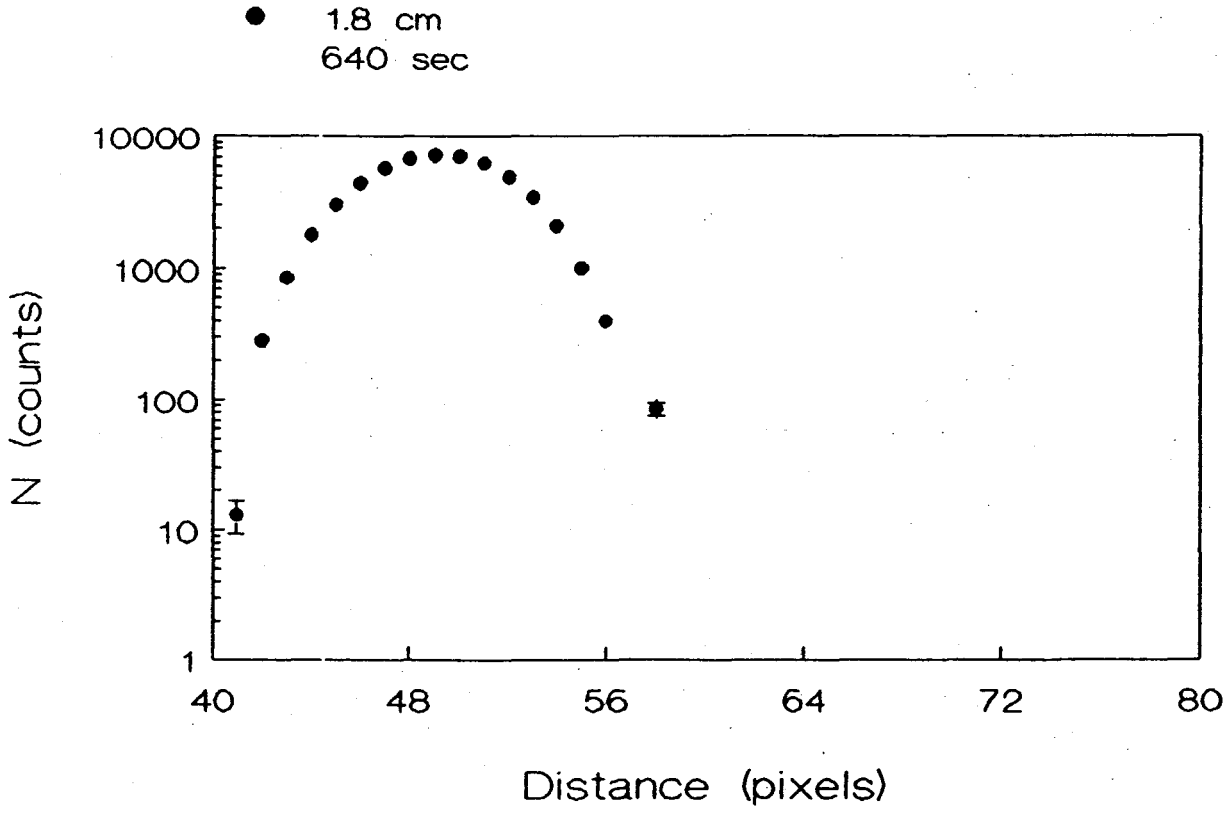

Fig. 6.1 *The distribution of events as a function of distance (number of pixel) in the image of the* 1.8 cm *diameter tumour containing* 1 μCi/ml *concentration activity and no background activity. The time of acquisition is* 640 sec.

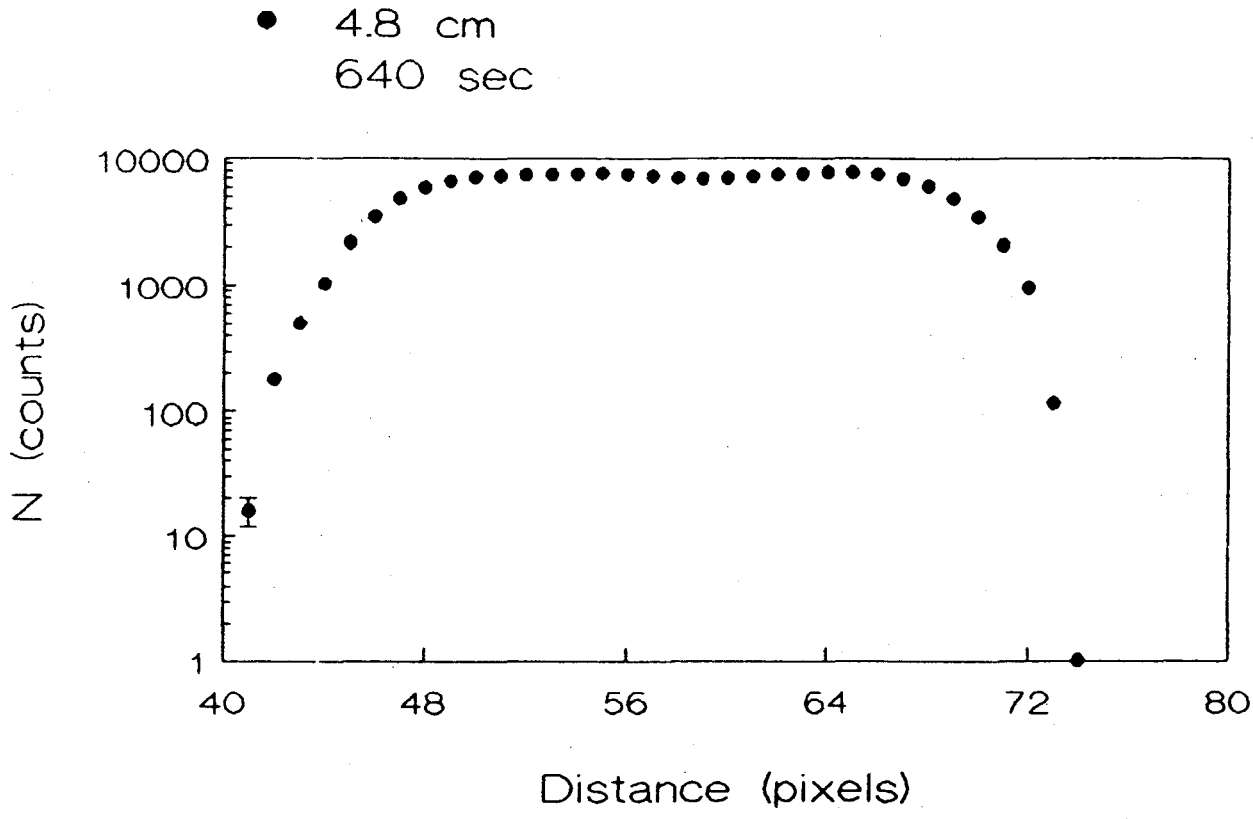

Fig. 6.2 *The distribution of events as a function of distance (number of pixel) in the image of the* 4.8 cm *diameter tumour containing* 1 μCi/ml *concentration activity and no background activity. The time of acquisition is* 640 sec.

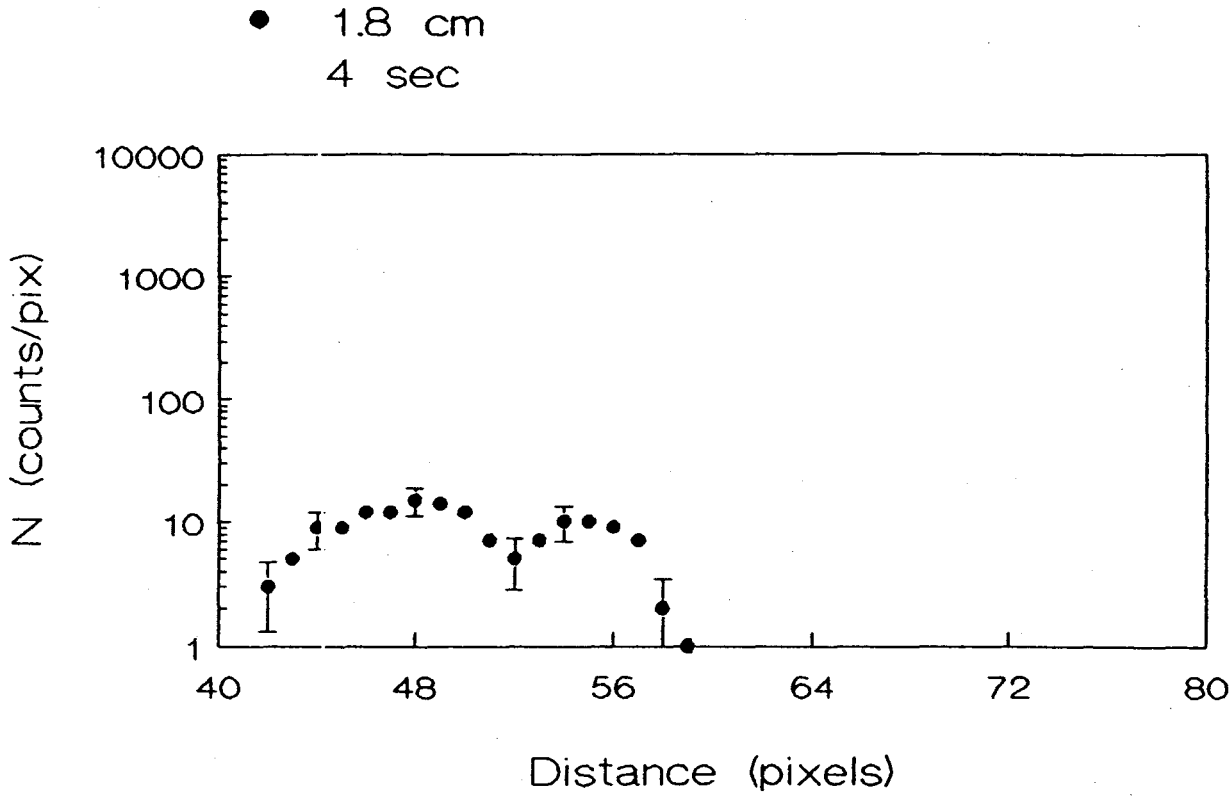

Fig. 6.3 *The distribution of events as a function of distance (number of pixel) in the image of the* 1.8 cm *diameter tumour containing* 1 μCi/ml *concentration activity and no background activity. The time of acquisition is* 4 sec.

6.2 The distribution of events in the image of a hot tumour with background activity.

No matter what the reason is of drug delivery to a tumour, to detect the tumour, to study its abnormal behaviour, to treat it or to follow a therapeutic treatment, always a fraction of the activity injected is taken over by the normal surrounding tissue. The presence of the activity in background region modifies enlarging the distributions presented in Fig. 6.1 and Fig. 6.2. The magnitude of this effect depends on the tumour-to-nontumour activity ratios.

Fig. 6.4 presents the distribution of events as a function of distance (number of pixel) in the image of 1.8 cm diameter tumour for tumour-to-nontumour ratios of 5/1, 10/1 and zero background activity. For comparison the curves are normalized to 1.

The uniform background activities of the above mentioned experiments, are analyzed using the same ROI defined before. Again the average number of counts per pixel obtained from these three ROI agrees in statistical limits regardless of the concentration activity used in the phantom.

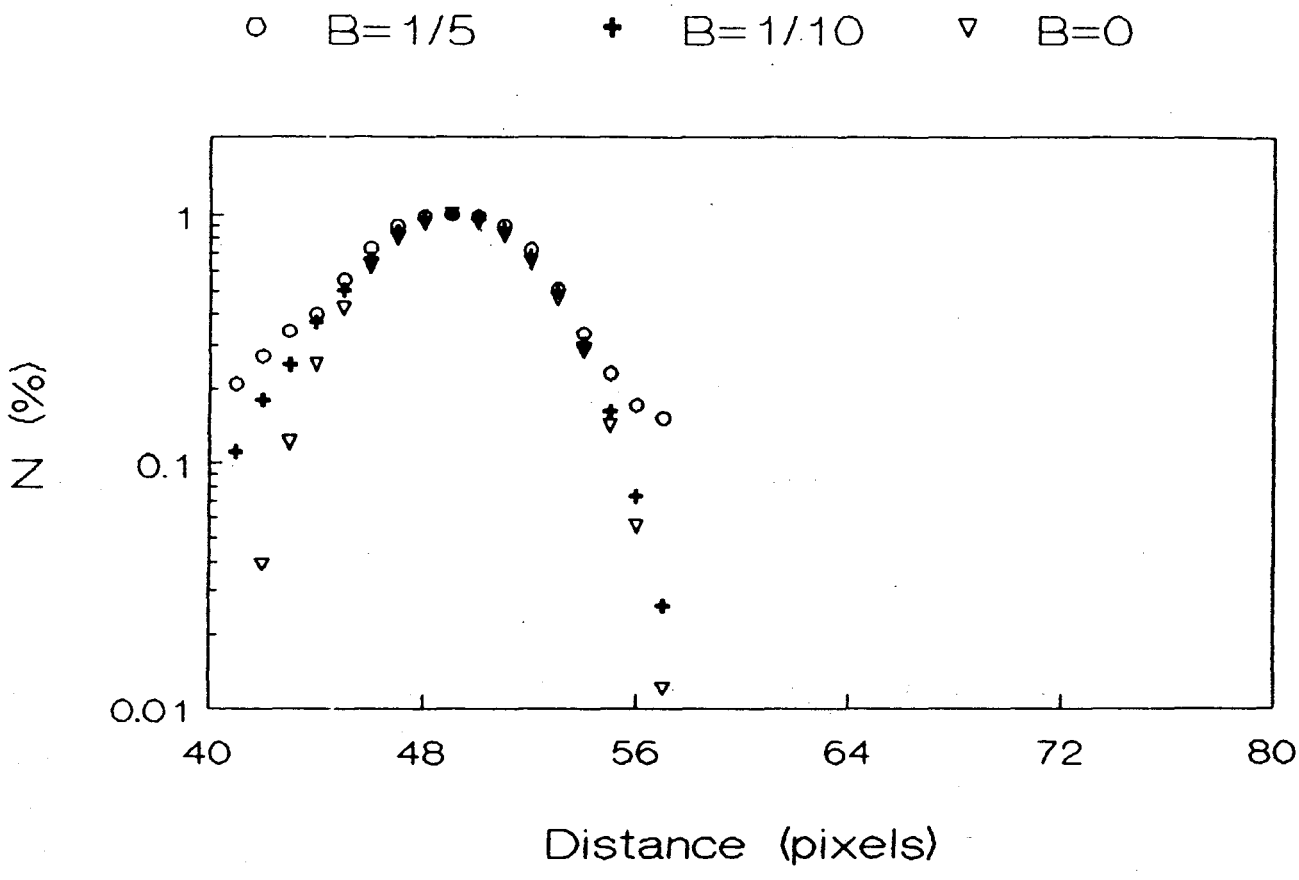

Fig. 6.4 *The distribution of events as a function of distance (number of pixel) in the image of the* 1.8 cm *diameter tumour sunk in a background activity, compared with the tumour distribution of events when no background activity is used. The concentration activity in the tumour is* 1 μCi/ml *and the background activities are* 0.265 μCi/ml *and* 0.1 μCi/ml.

7. ABSOLUTE QUANTITATION IN POSITRON EMISSION TOMOGRAPHY.

Despite a big effort, [27-32, 41, 42, 49-57], the absolute measurements in computer assisted tomography remains a goal to be attained.

Absolute evaluations in computed tomography includes:

- the tumour's (or organ target) volume determination,
- its coordinates (X,Y,Z) *position*,
- the amount of drug (μCi/ml) delivered to the tumour (or organ target),
- the absolute amount of drug (μCi/ml) in surrounding tissue.

Drug delivery has particular importance in the chemotherapy of cancer. Cancer chemotherapy is based on assumed relation between the dose administered to the patient and the response of the tumour (the dose-response relation). Absorbed doses for target tissues (tumours) and non-target tissues (normal organs) for cancer therapy using systematically administered radionuclides, requires accurate and precise determination of the time-dependent concentrations, or total amounts of radioactivity in situ. The data used for the determination of cumulated activities in the various regions of the body, can be obtained through discrete serial measurements and integration of the resulting time-activity data. However, with the notable exception of blood, a sample which can be extracted through venipuncture for direct radioassay exvivo, such measurements are highly problematic.

Absolute amounts and concentrations of radionuclide can be determined in a sample when the sensivity of the detector is determined and the geometry of the counting conditions are fixed. These requirements are readily met when a sample is counted by a scintillation detector, but can only be approximated for radionuclides in a living system. No generally applicable and/or validated method for noninvasive radionuclide quantitation in situ is yet available.

This study tries to find a simple and reliable method for absolute quantitation in Positron Emission Tomography, that can be applied to any computer assisted tomograph systems. The aspects investigated are:

- the dimensions of a tumour,
- the *position* of a tumour,
- the amount of drug accumulated in the tumour (μCi/ml), and
- the tumour-to-nontumour activity ratios, obtained from the PET images.

7.1 The dimensions of the tumour.

Two methods to evaluate the dimension of a tumour from its image were analyzed.

The first attempt to define the dimension of a tumour followed the recipe [56]. It consists of obtaining the real dimension of the tumour cylinder from the image distribution of counts presented in Fig. 6.1 and Fig. 6.2, on a predetermined constant position. The real dimension of an 1.8 cm diameter tumour (9 pixels) and 4.8 cm diameter tumour (24 pixels) may be identified at constant values on the distribution of counts regardless of the number of counts accumulated in the maximum of the distribution of the tumour image (Fig. 7.1). Applied to data in Fig. 6.1 and Fig. 6.2, if the maximum of the distribution represents 100%, then the 1.8 cm diameter tumour can be found at (35.43 ± 1.22)% and the 4.8 cm diameter tumour at (43.9 ± 1.89)%.

Contrary to the results presented in [56], these values seem to depend on the dimension of the tumour. Fig. 7.2 presents the dependence of these positions of identification of real tumour dimensions on the counts distribution in the image, versus the real diameter of the tumours. Roughly, the real dimension of a tumour may be found at ≈ 40% on the tumour distribution of events, when there are no activity in the background region, at least for these dimensions of tumour. This result gives an underestimation by ≈ 1 pixel (2 mm) for the dimension of an 1.8 cm diameter tumour and an overestimation by ≈ 1 pixel for the 4.8 cm diameter tumour. The errors increase proportional to the diameter of the tumour growth or fall.

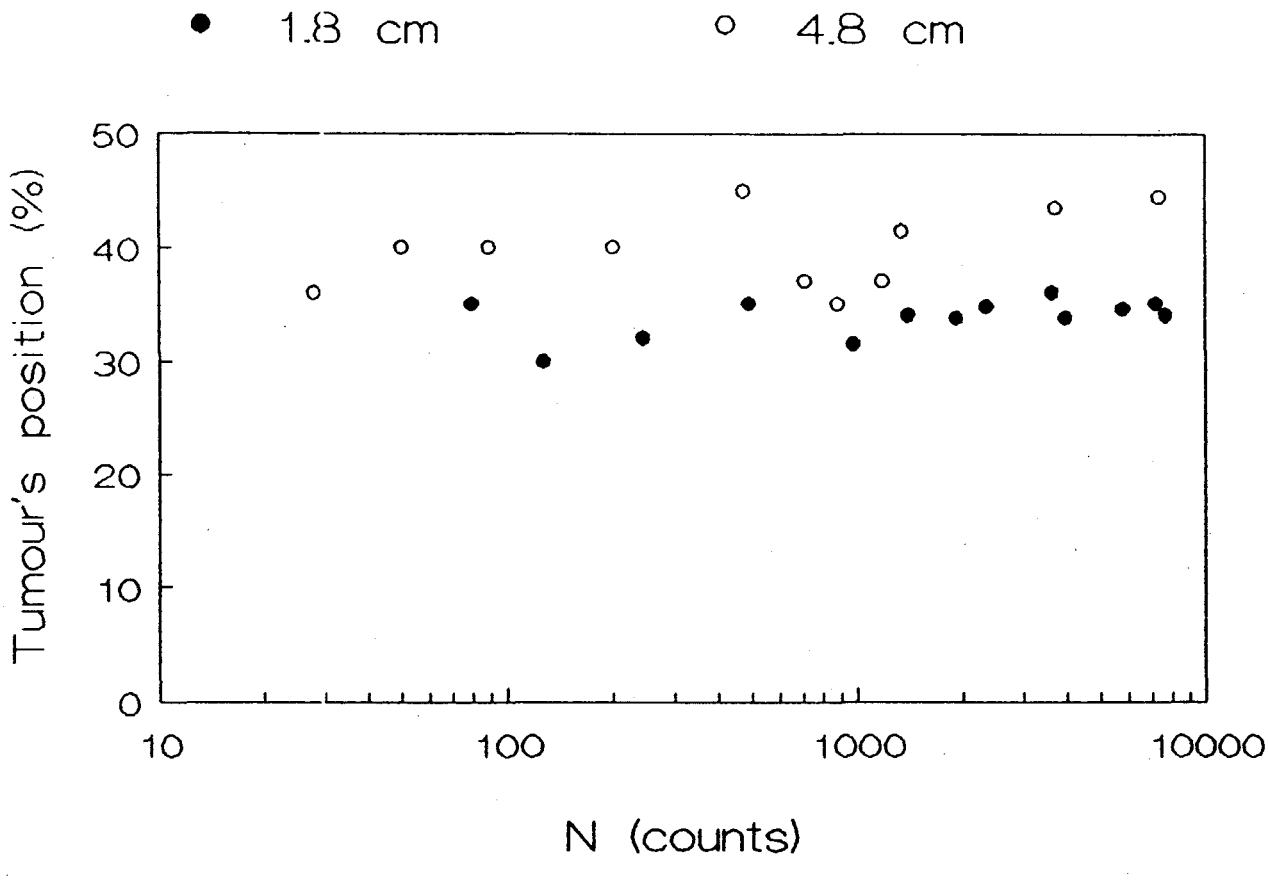

Fig. 7.1 *The position of the real dimension of the tumour (% from the maximum) on the distribution of events* (Fig. 6.1 *and* Fig. 6.2), *versus the number of events in the maximum of the distribution. The data are for the* 1.8 cm *diameter tumour and the* 4.8 cm *diameter tumour. No background activity is used.*

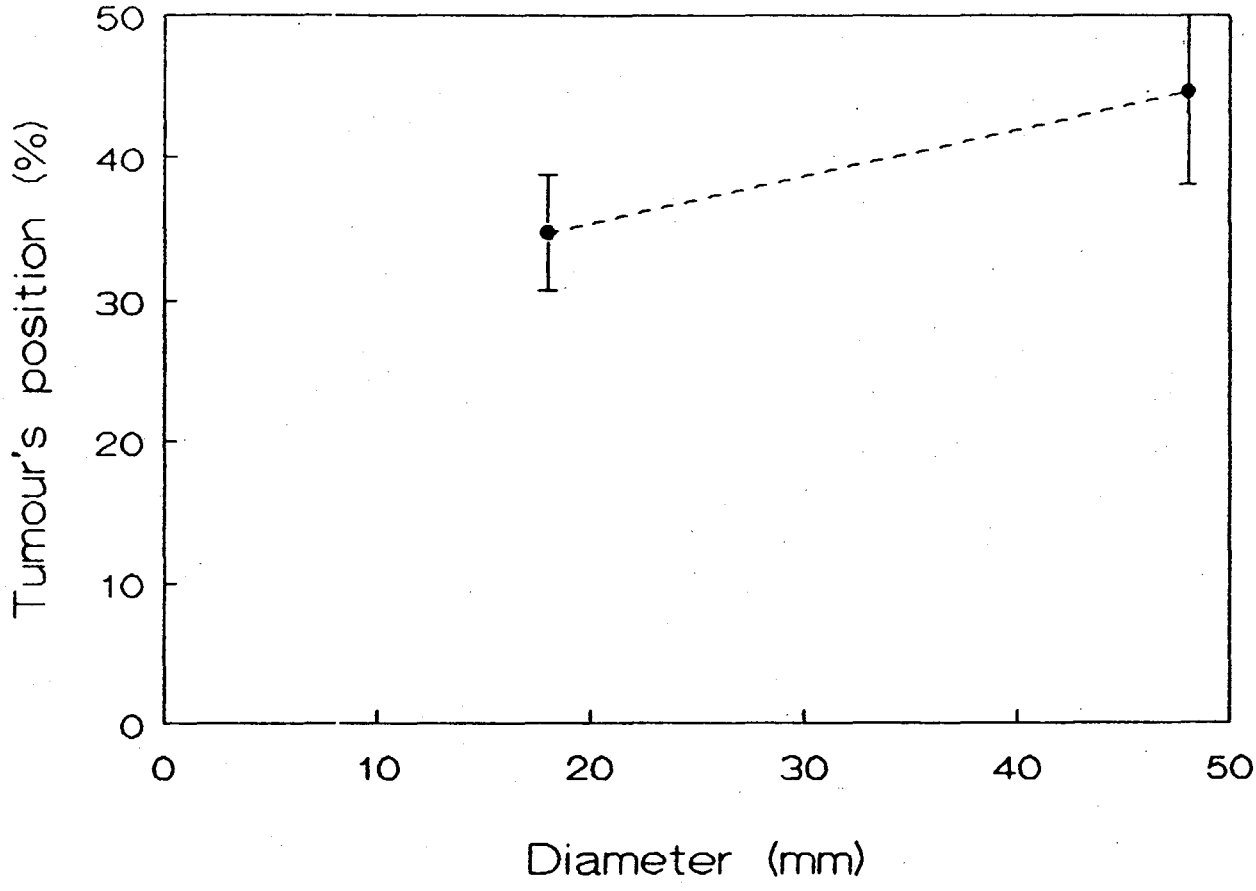

Fig. 7.2 *The position of the real dimension of the tumour (% from the maximum) on the distribution of events versus the diameter of the tumour.*

A more sensitive method to evaluate the dimension of a tumour from its image consists of creating a calibration of FWHM values of the counts distribution (Fig. 6.1 and Fig. 6.2) expressed in pixels, in absolute units (mm). The dependence of the FWHM values on the number of counts accumulated in the maximum of the tumour image (zero background activity), is presented in Fig. 7.3. For statistics higher than ≈ 300 counts/pix in the maximum of the distribution, the dependence is a constant. For these constant values, 7.62 ± 0.16 pixels for 1.8 cm diameter tumour, and 22.7 ± 0.8 pixels for 4.8 cm diameter tumour, the dependence of the FWHM on the real diameter of the tumour is shown in Fig. 7.4. At least for these dimensions of tumours, the dependence seems to be linear. This linear dependence, probably, is not valuable for very small dimensions of the tumours (< 1.8 cm) which need to be paid a careful attention.

A hot tumour without surrounding activity does not represent a real fact. Fig. 6.4 presents the distributions of the events in the image of a tumour in an experiment simulating a hot tumour in the middle of a radioactive solution. The concentration activities were changed in different experiments.

To obtain the necessary distribution of counts as a function of distance for zero background activity used in tumour's dimension evaluation, the background should be subtracted in each case. Then, the "calibration" (Fig. 7.4) gives the real dimension of the tumour under investigation.

Moving to the real brain images, this background activity has to be well defined, this being the most important source of error in tumour's dimension evaluation.

This method can be applied to different shapes of tumors. The dimension of the tumour can be found for each horizontal line of pixels and even for each vertical line of pixels to improve the accuracy of the evaluation. In this way, the dimension of the tumour can be determined for every 2 mm, in our case, in both directions, horizontally and vertically. Moreover, the method can be used in the same way to evaluate the dimension of a cold tumour or even in the case of a heterogeneous distribution of activity such as a cold nucleus surrounding by a hot ring. These aspects need to be studied more.

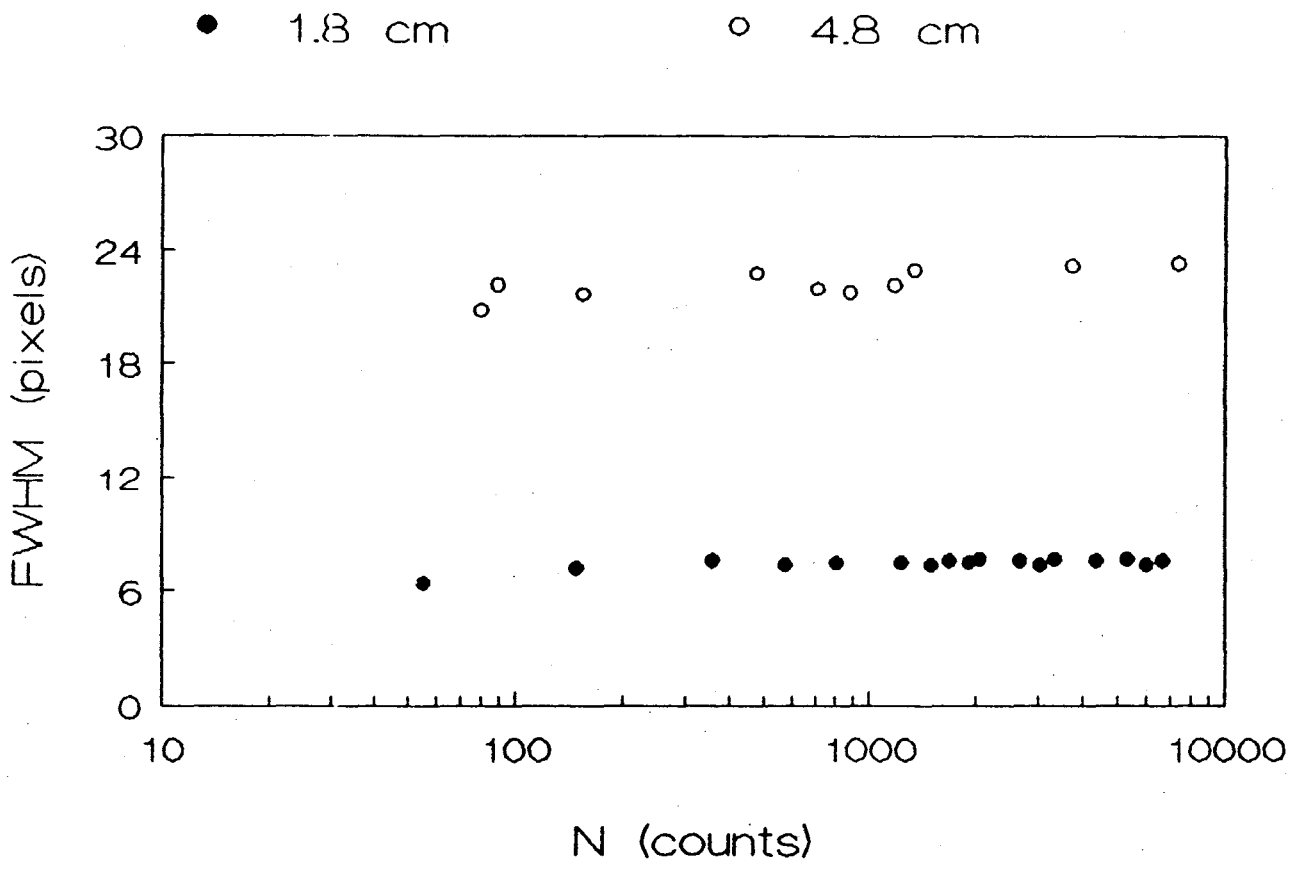

Fig. 7.3 *The* FWHM *values of the tumour image distribution of events as a function of the number of events accumulated in the maximum of the distribution. The data are for two dimensions of tumours:* 1.8 cm *and* 4.8 cm *diameter cylinders. No background activity is used.*

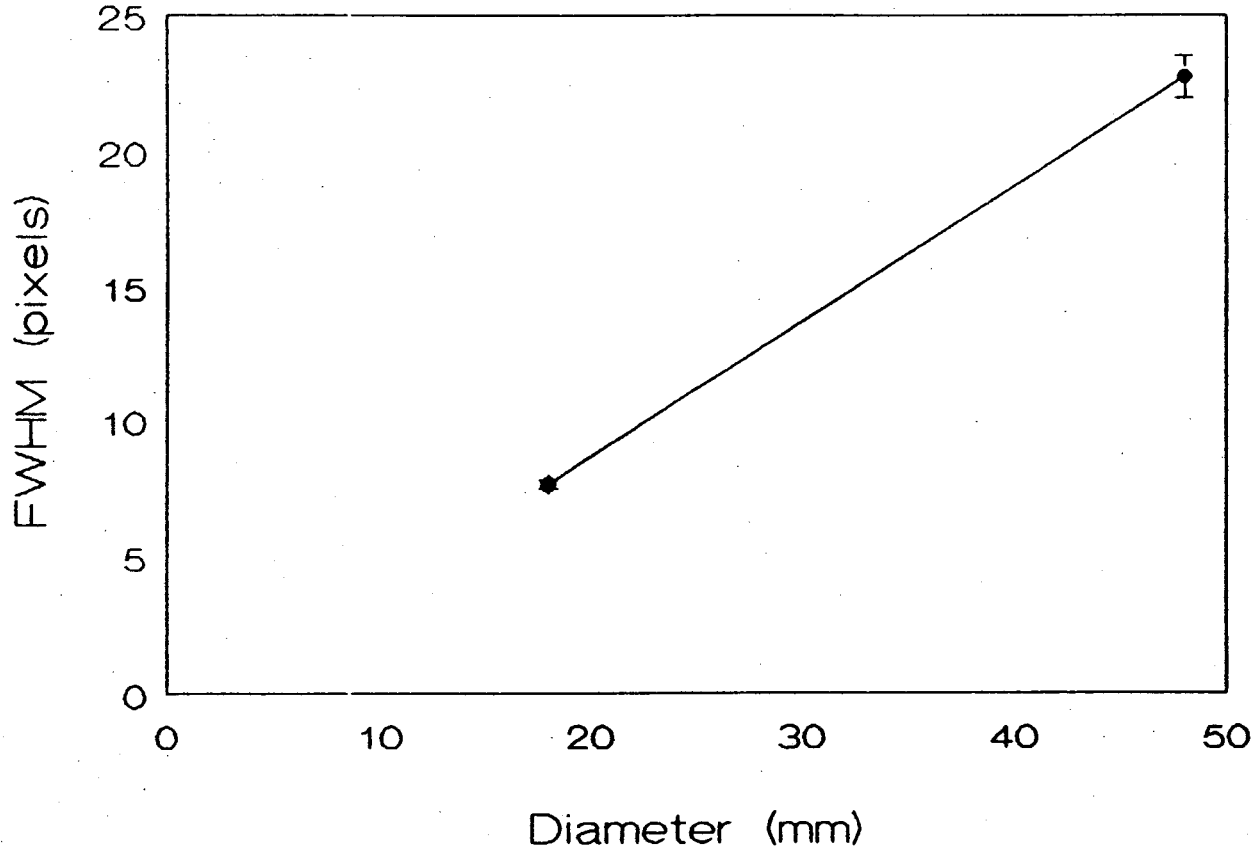

Fig. 7.4 *The dependence of the* FWHM *values of the tumour image distribution of events on the diameter of the tumour cylinders.*

7.2 The *position* of a tumour.

When the dimensions of a tumour are evaluated, its edges are defined. This is true when the tumour image can be well separated from the background. If the tumour peak lies in a very high background activity, different mathematical procedures can be used to separate the tumour contribution, such as fit with theoretical distributions for tumour and background regions.

The next step is to define the *position* of the tumour, that is to determine the (X,Y) coordinates of the centre of the tumour, on the image. The Z coordinate is defined by the slice position.

Small tumours (1.8 cm diameter cylinder) show a Gaussian distribution of events in the image. In this case, the tumour's *position* may be identified by the coordinates of the maximum of the distribution, (X,Y). Fig. 7.5 shows the X coordinate position of the maximum of the Gaussian distribution (expressed in number of pixel) versus the number of counts in this maximum. Each point represents the average value and statistical errors from 10 measurements. As expected, low statistic images are not precise in defining the position of the maximum, the errors being sometimes greater than ± 2 pixels. Even from high statistic images, the errors can be ± 0.5 pixels.

In defining the *position* of a tumour, the middle point of the FWHM of the events distributions can be of real help, regardless of the dimension of the tumour. A difficulty arises from the fact that the distribution of events in the tumour region is symmetrical only in the centre of the image. Moving to the edges of the phantom, the distribution becomes asymmetrical due to the reconstruction procedure. The middle point of FWHM may be found through fitting the experimental distribution with a symmetrical distribution.

The dimension of a tumour and its *position* aspects of absolute quantitation evaluations should be studied using a special phantom. The phantom would have few tumours cylinders inside, placed in different positions, starting with the centre of the image up to the edges.

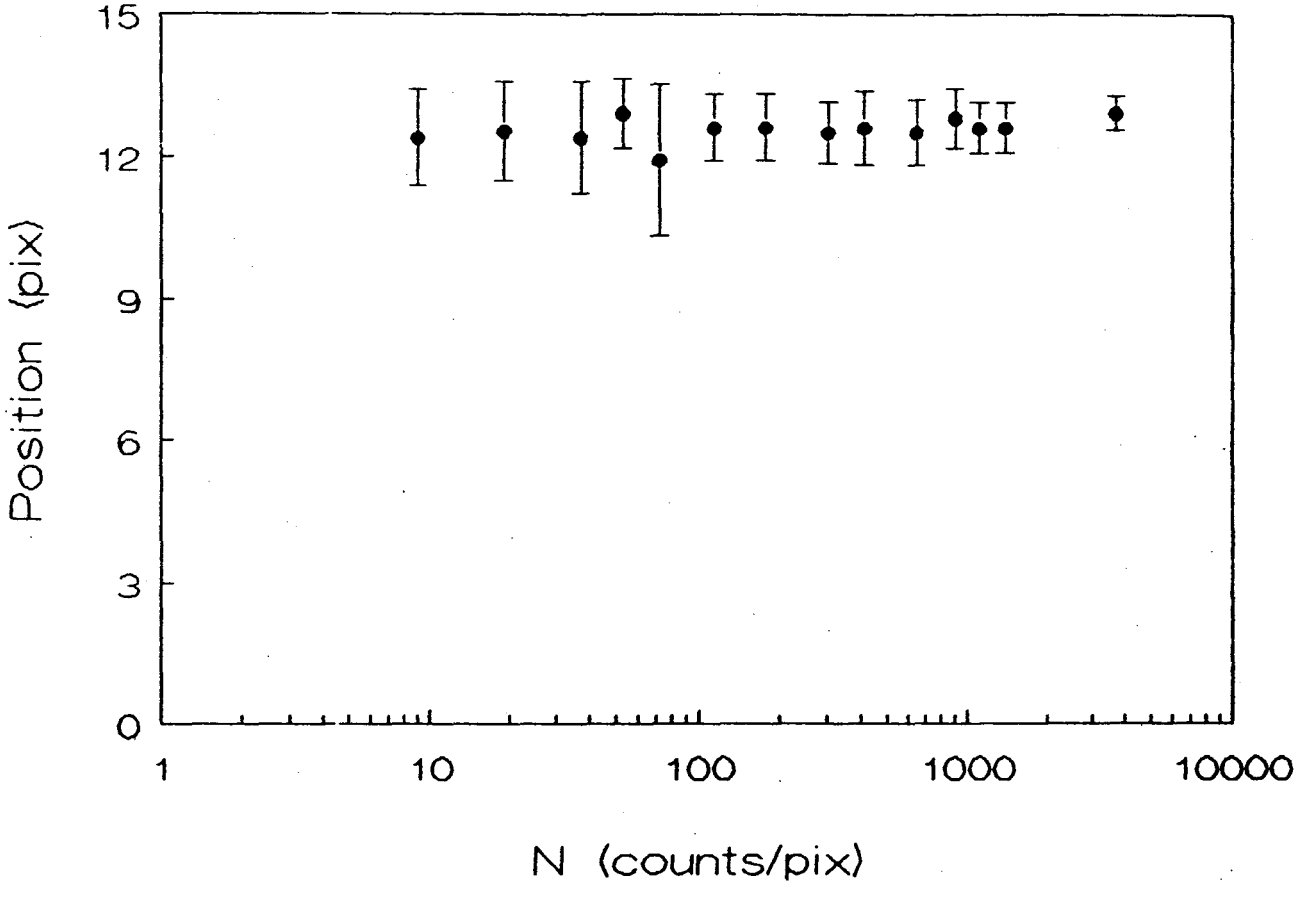

Fig. 7.5 *The position of the maximum of the Gaussian distribution of events (Fig. 6.1), versus the number of events in the maximum.*

Finally, after the *position* and the dimension of a tumour are evaluated from the image, the tumour can be localized in the brain. The brain contour fortunately is easier to define compared to other organs, due to greater drug-activity assimilation in the gray matter.

7.3 The amount of drug accumulated in a tumour.

The role of PET is to provide an accurate set of image data which would allow to determine the amount and spatial distribution of a radioisotope in the cross section of the brain, represented by its image. The differences between normal brain tissue and tumour tissue in vascularity, metabolism, as well as the effects of an anticancer treatment can be followed only in a quantitative study.

7.3.1 Hot tumour without surrounding activity.

The rate of counts (per pixel) obtained from the image can be correlated to the activity introduced in the phantom (or the brain).

In the time of experiment the rate of detected events is recorded to verify the detection system. Fig. 7.6 presents the detected rate of events versus time of acquisition in the experiment of the hot 1.8 cm diameter tumour without any background activity. The rate of detected events is constant, in statistical limits.

The detected rate of events was always followed for all images of the same experiment, in order to verify that no loss of counts can be due to an improper detection system functioning.

Fig. 7.7 presents the dependence of the maximum rate of counts (per pixel) in the image of a tumour (1.8 cm and 4.8 cm diameter) versus the number of events in that pixel.

In this experiment, the 25 cm diameter phantom is filled with water (no activity introduced in nontumour region). The variation in the number of counts accumulated per pixel is reached choosing different times of acquisition, between 2 sec up to 640 sec.

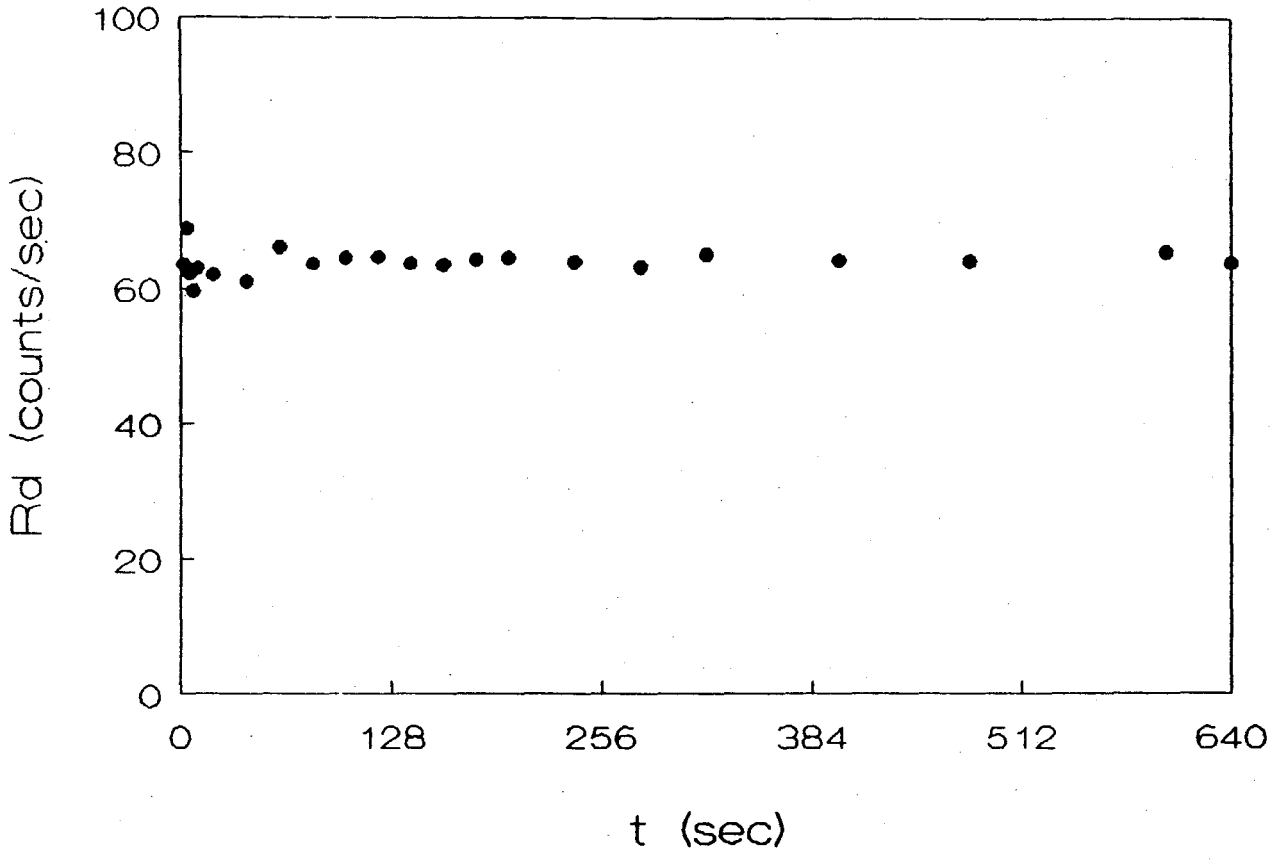

Fig. 7.6 *The detected rate of events versus acquisition time of a slice image. These values are obtained for the images of a hot* (1 μCi/ml) 1.8 cm *diameter tumour and no background activity.*

Each point in Fig. 7.7 represents the average value and statistical errors from 10 measurements. In the case of 1.8 cm diameter of the tumour, two concentration activities are chosen: 1.0 μCi/ml and 0.5 μCi/ml. The rate of counts corresponds to the maximum of the Gaussian distribution of events (Fig. 6.1).

The distribution of counts as a function of distance in the larger tumour (4.8 cm) presents a plateau (Fig. 6.2). The rate of counts is obtained from the average number of counts and the errors given by 15 X 15 pixels ROI placed in the middle of the plateau. For this dimension of the tumour only one concentration activity is used (1 μCi/ml).

The interesting results presented in Fig. 7.7 show that the real activity distribution in the image of a tumour can be obtained only for a certain statistics. The minimum number of events in the tumour image necessary to reflect the reality depends on the dimension of the tumour. In our case, for $\approx$ 1000 counts/pix, the true activity is reproduced in the image, regardless of the concentration activity used in the tumour, and $\approx$ 300 counts/pix are enough to achieve the real activity in the image of a 4.8 cm diameter of the tumour.

The authors [30] introduced a *recovery coefficient* to correct the image activity of small tumours (< 3 cm diameter in their case) (Fig. 4.8). However, this study shows clearly that the recovery coefficient depends not only on the dimension of a tumour, but on the number of events accumulated in the image as well.

Fig. 7.8 presents the experimental correction factors determined from this study, versus the number of events (per pixel) in the maximum of the distributions, for 1.8 cm and 4.8 cm diameter of the tumour. These factors have to be applied to the tumour rate readings in order to obtain the real activities. The correction factors for any other tumour dimensions between these two values can be obtained by interpolation.

From these two factors affecting the quantitative evaluations of the concentration activity in a tumour, the object size and the statistics, the last one is more important, because even for a small tumour, the real activity can be reproduced in the image if enough events are registered.

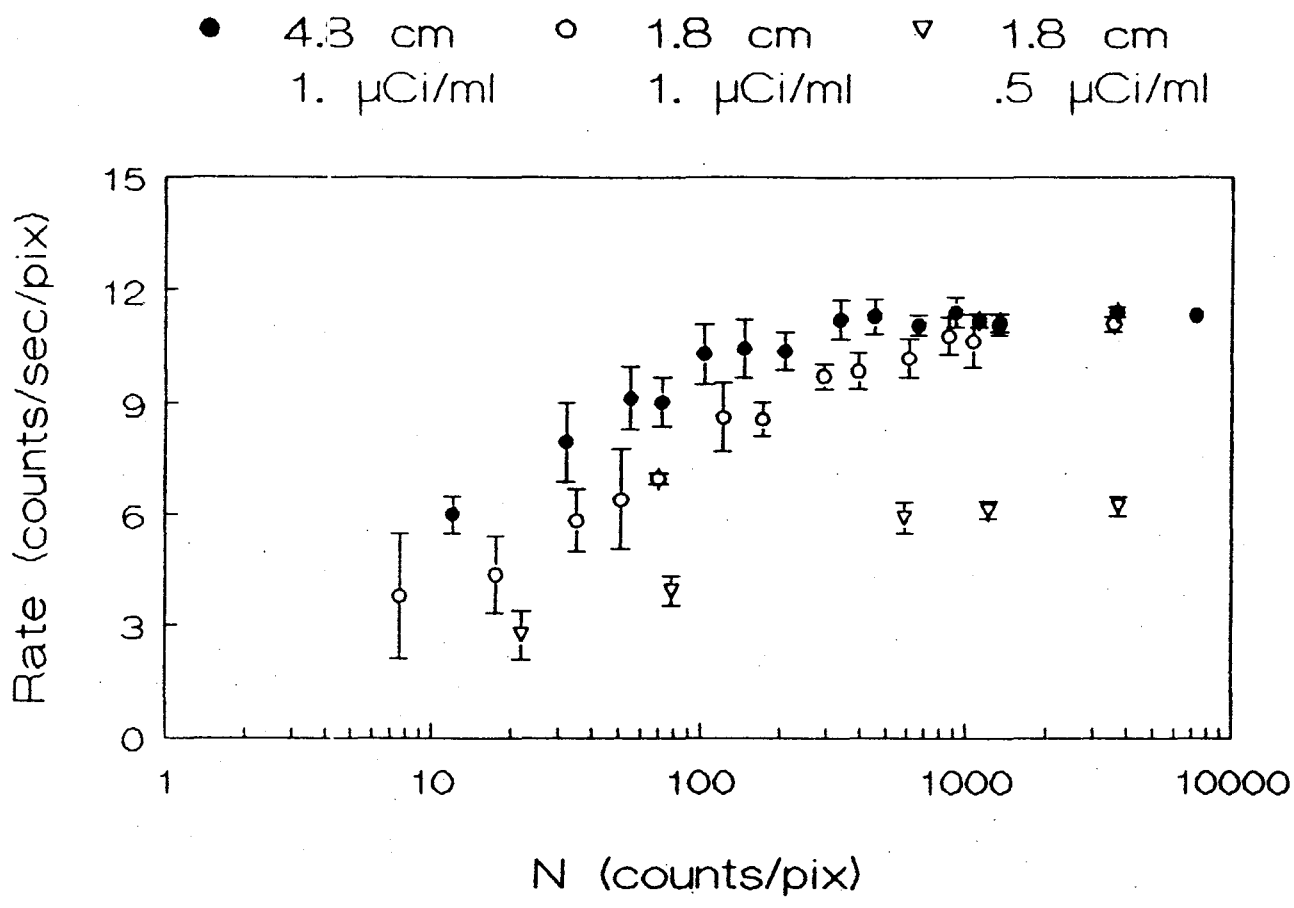

Fig. 7.7 *The maximum rate of events in the tumour image versus the number of events in the maximum of the distribution. The* 4.8 cm *diameter tumour contains* 1μCi/ml *concentration activity and* 1.8 cm *diameter tumour contains* 1 μCi/ml *and* 0.53 μCi/ml *concentration activities. No background activity is used.*

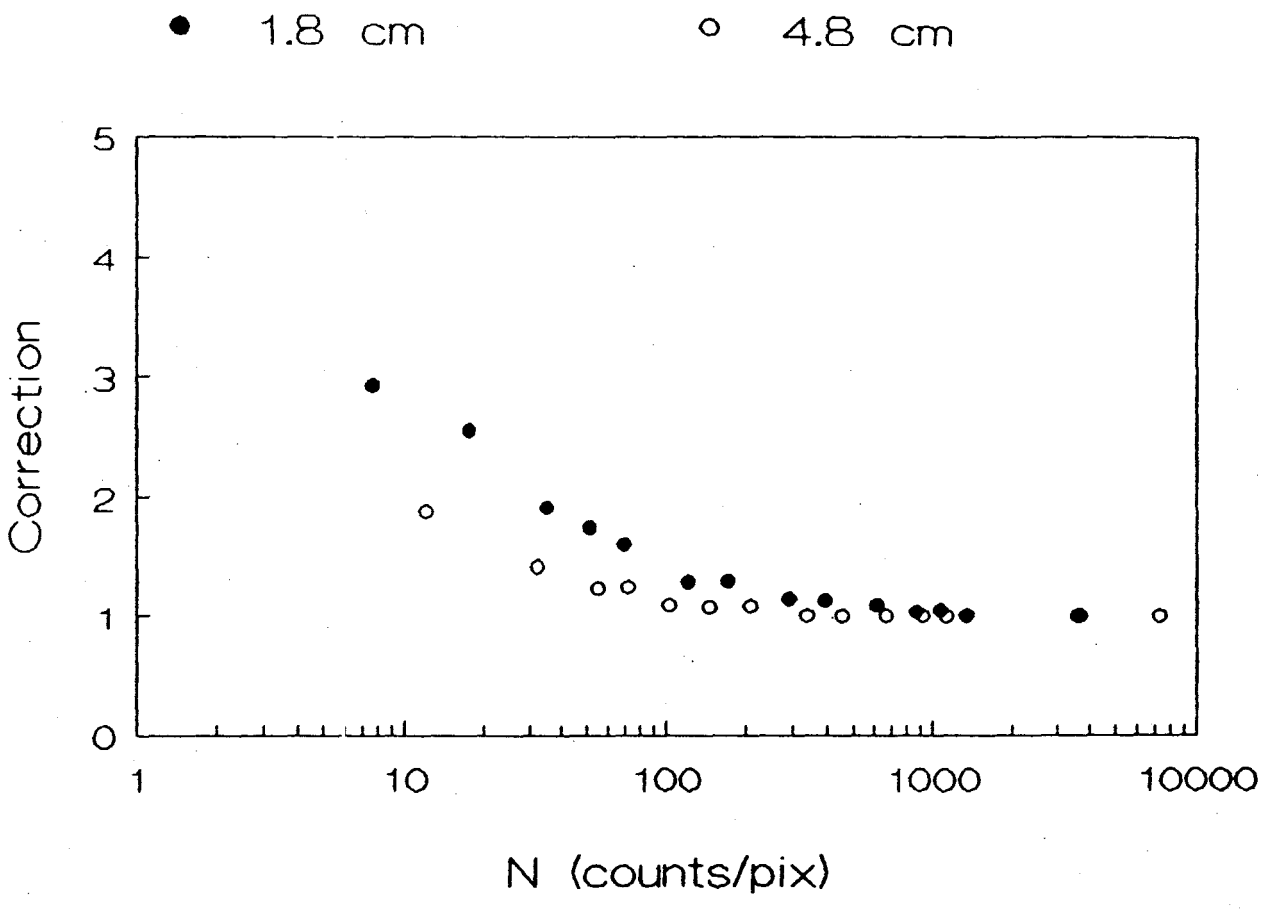

Fig. 7.8 *The correction factors for the tumour concentration activity as a function of the number of events accumulated in the maximum of the distributions of events for the two dimensions of tumours:* 1.8 cm *and* 4.8 cm *diameters.*

In these experiments, no activity was introduced in the phantom, but a background rate was registered. The background rate as a function of the number of counts per pixel in the tumour region is presented in Fig. 7.9. The values were determined from 40 X 40 pixels ROI. The constant background rate (0.14 ± 0.012) counts/sec/pix occurs at ≈ 1000 counts/pix in the maximum of the Gaussian distribution of events (1.8 cm diameter of the tumour). The lower statistics generates a slight increase in the background rate due to star artifacts formed in the reconstruction process.

The tumour-to-nontumour ratio obtained in an image of a hot tumour without any activity in surrounding region, as a function of the number of counts in the tumour image maximum is presented in Fig. 7.10. This ratio is constant (76 ± 5.8) at statistics higher than ≈ 1000 counts/pix. The lower statistical images are characterized by a decreasing tumour-to-background ratio due to decreasing in tumour rate and increasing in background rate.

The background rate includes the background generated by the reconstruction procedure, and the contributions due to scattering and accidental coincidences. However, the sum of all these effects is almost two orders of magnitude lower than the real event rate per pixel in the tumour image. This fact is useful in absolute evaluations of the concentration activities. At the same time, this background generation in the absence of any activity represents a limitation of PET method in studying very high tumour-to-nontumour ratios.

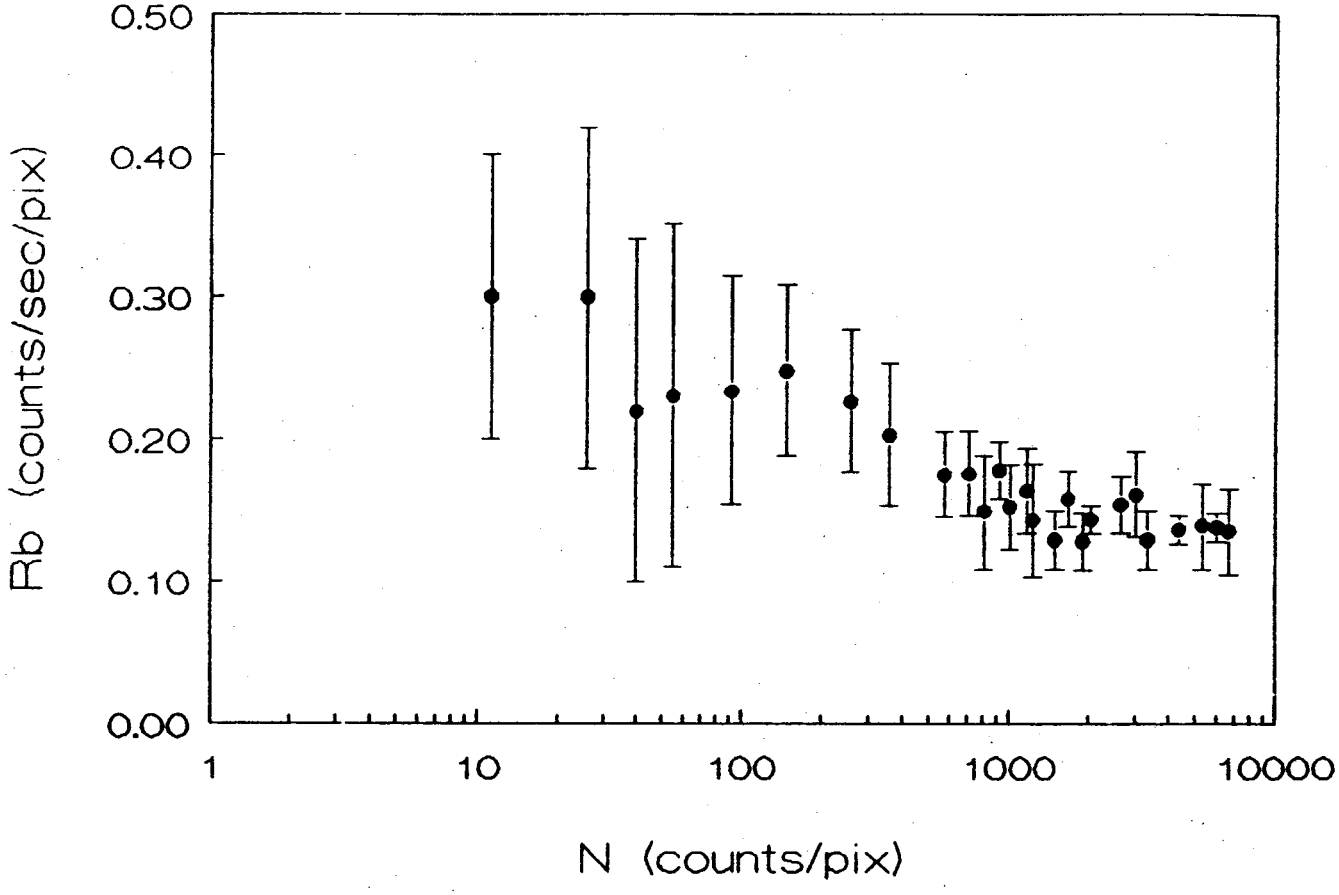

Fig. 7.9 *The background rate in a phantom containing* 1.8 cm *hot tumour* (1 μCi/ml) *and no background activity.*

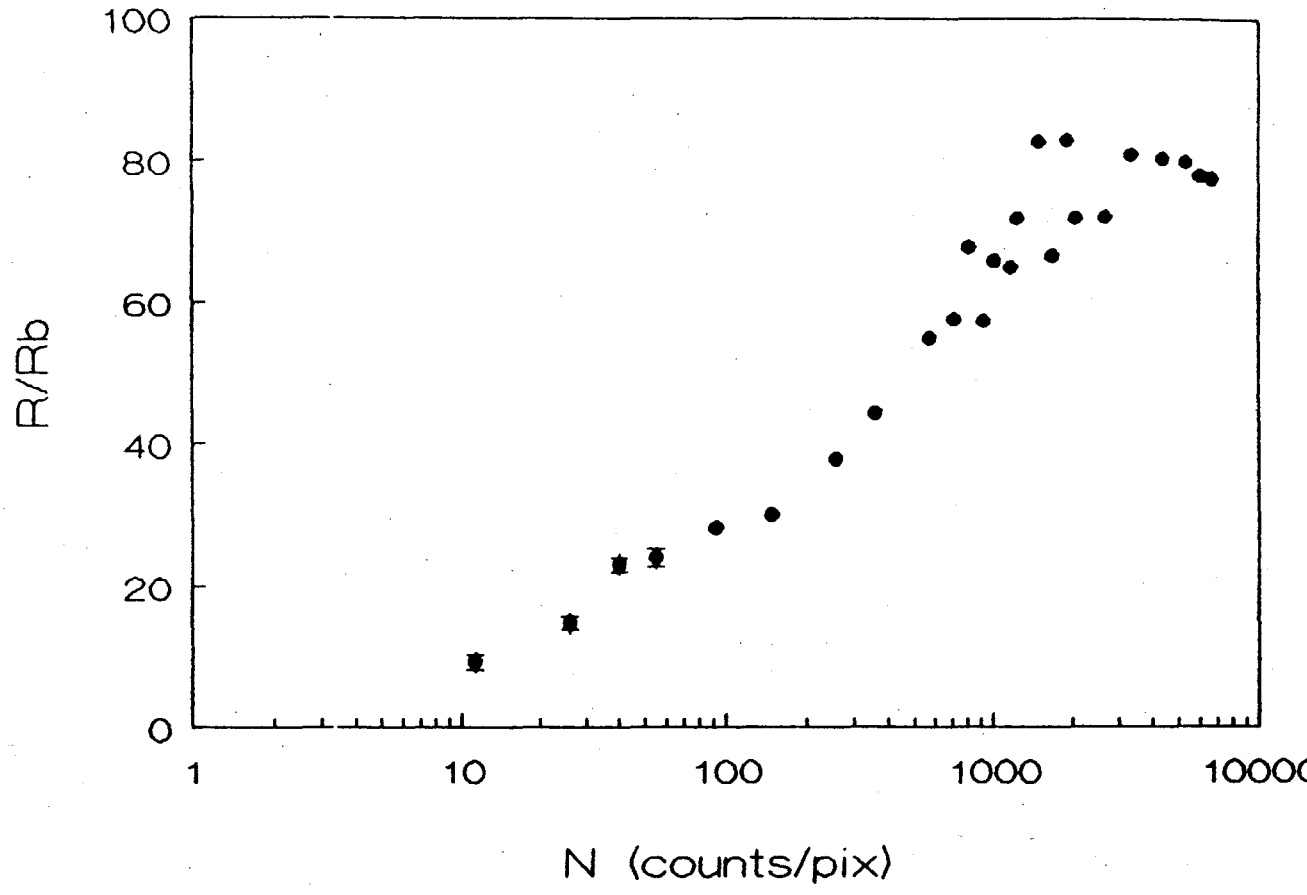

Fig. 7.10 *The tumour-to-nontumour activity ratios in the image of a phantom containing a hot tumour (1 μCi/ml) and no background activity.*

7.3.2 Hot tumour with surrounding activity.

The PET system must provide absolute quantitative measurements of concentration activities in the tumour region, in the surrounding tissues, as well as the tumour-to-nontumour ratios.

The rate of counts (per pixel) in the 1.8 cm diameter tumour image with background activity, as a function of the number of counts (per pixel) accumulated in the maximum of the Gaussian distribution of events, looks different from previous case as seen in Fig. 7.11.

The tumour activity used in this experiment was 1 μCi/ml and the background activity was 0.1 μCi/ml. Even for a small background activity (tumour-to-nontumour ratio 10/1), the rate of counts in the tumour region becomes almost constant regardless of the number of events accumulated. A slight increase in the rate occurs for low statistical images.

This behaviour of the rate of events in a tumour image surrounded by activity is different of that of a rate of counts in a tumour image without background activity (Fig. 7.6). It seems that no recovery coefficient is necessary to obtain the real concentration activity from the image of a tumour, regardless of the dimension of the tumour or the statistics accumulated in the image. The concentration activity can be extracted directly from the maximum of the distribution for a wide range of accumulated events. Contrary, the slight increase in the rate of counts at very low statistics creates the danger of overestimating the low counts images (or short time measurements) and not underestimating as predicted in [30].

The behaviour of the maximum rate of events obtained from low statistical images of a tumour surrounded by activity proves that round off errors are not the cause of the fall of the rate of events obtained in Fig. 7.7. More than this, these type of errors could not have an exponential dependence on the number of events accumulated in the image.

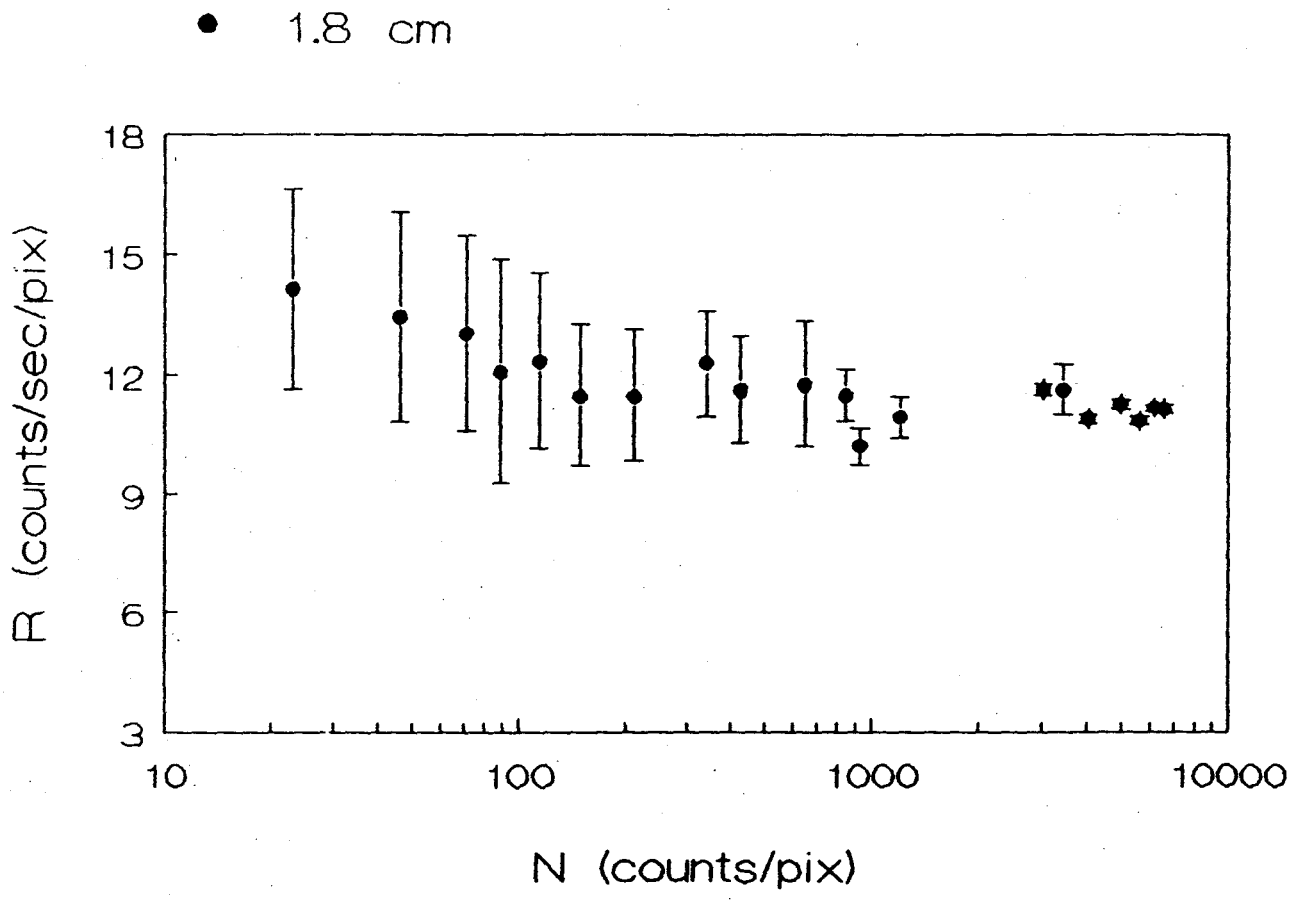

Fig. 7.11 *The maximum rate of counts in the* 1.8 cm *diameter tumour image* (1 μCi/ml), *versus the number of events in this maximum obtained from the phantom image containing* 0.1 μCi/ml *background activity.*

This very important aspect of the absolute quantitation of the drug delivery to a tumour surrounded by a background activity from a PET image should be studied for a higher background activity and for a lower background activity (lower and higher tumour-to-nontumour ratios) to confirm and to evaluate the magnitude of this increase in the rate of counts at low statistical measurements. Very small tumours (diameters less than 1.8 cm) should be included in this study as well.

The almost constant behaviour of the rate of events in the image of a hot tumour cylinder sunk in a radioactive bath is the result of the compensation in the loss of counts characteristic to low statistic images (Fig. 7.7). This compensation is due to the higher amplification of a low statistical image in the reconstruction process compared with high statistical images.

The degree of amplification of an image through the filtering process is given by the ratio of the total number of events in the reconstructed image on the total number of detected events. Fig. 7.12 presents the dependence of this ratio on the number of detected events for 25 cm diameter phantom. The values are obtained from different experiments, including different tumour-to-nontumour ratios (10/1, 5/1, 3/1). A constant amplification of the image (6.47 ± 0.16) is characteristic to the filter used and occurs at a detected number of events greater than $\approx 5\ 10^4$. Under this value of the total detected events per image slice, the amplification of the image by the filtering process is higher, up to 3 times at ≈ 4000 detected events, thus compensating the loss (up to 3 times) in events in the image of a hot tumour (1.8 cm diameter) without any background activity.

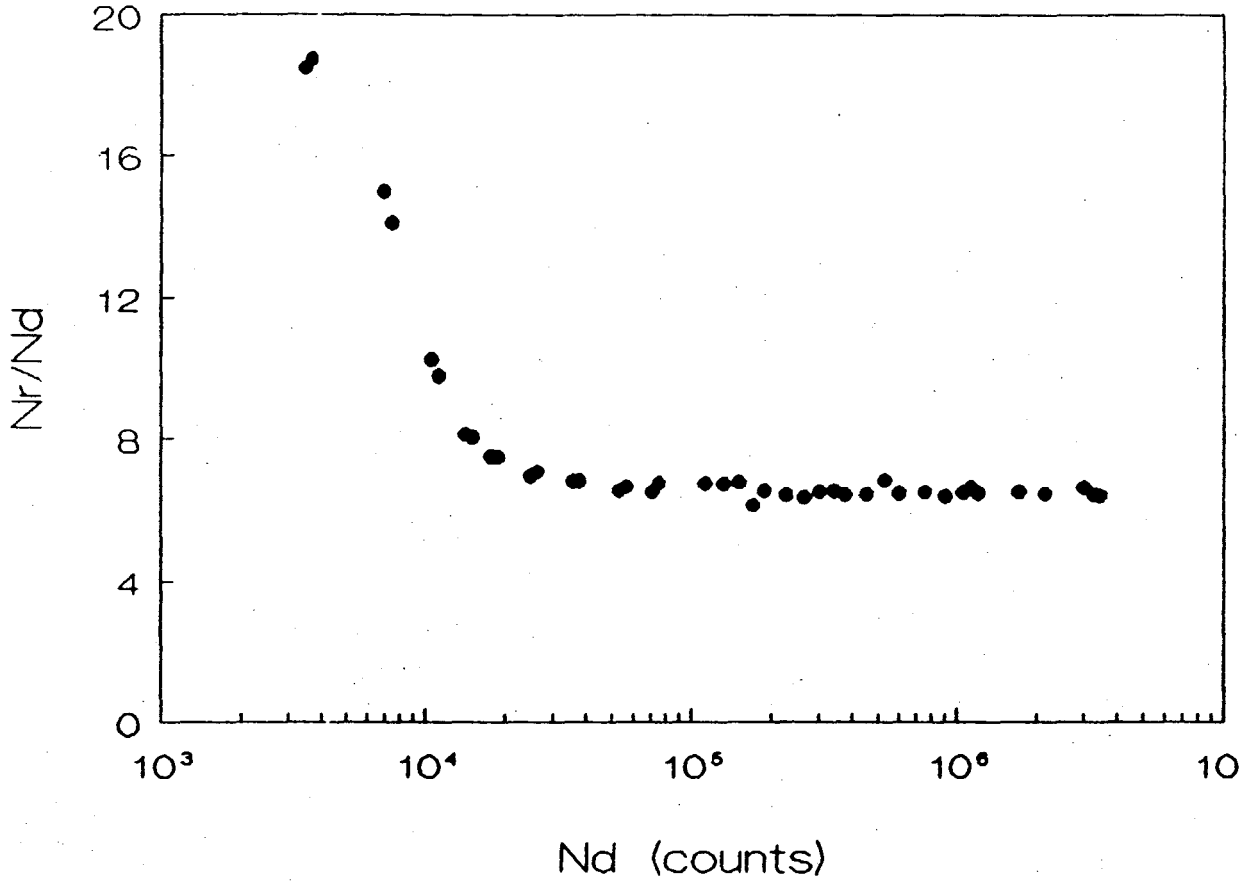

Fig. 7.12 *The degree of amplification of a real image slice by the reconstruction process. The ratio of the total number of the events recorded in the reconstructed image of a* 25 cm *diameter phantom on the total number of detected events, versus the total number of detected events. The values are obtained from different tumour-to-nontumour activity ratios experiments.*

7.4 The modified filter.

In chapter 3.3.3 the theory of the filtered back-projection method was described. To sum up, the filter in the real space is obtained:

- choosing ar window function in frequency space,
- multiplying the window by the ramp function,
- inversing Fourier transform this product.

Therefore, the filter in real space is described by:

$$H(d) = \left\{ \mathcal{F}^{-1} \left[|f| \, W(f) \right] \right\} \qquad (7.1)$$

where $\mathcal{F}^{-1}$ denotes inverse Fourier transform, f represents the frequency and W(f) is the window function.

Each projection line is convolved with the chosen filter and then back-projected in order to eliminate the high background generated by the simple back-projection method.

The discrete Butterworth filter (eq. (3.55)) used in the reconstruction of images at McMaster Hospital PET is presented in Fig. 7.13. The amplitude of the filter as a function of distance shows a sharpening kernel which is symmetric and defined for the same number of points as are sampled in one dimension. Here, the distance is expressed in line integral numbers. For practical use, the filter is limited to 15 points for one half of the filter, corresponding to 15 line integrals, indicating 29 possible coincidences between one detector and other ± 14 opposite detectors.

In order to detect the real annihilation γ rays scattered in an angle less than 30^{o}, each detector of this tomograph operates in coincidence with other 61 detectors (± 30 detectors for a central ray) (see Fig. 4.6). In this way, the whole head phantom is in the field of view.

Under these circumstances, the reason that a 15 point filter is used is probably the fact that the amplitudes of far points of the filter are very small compared with the amplitudes of the filter at small distances.

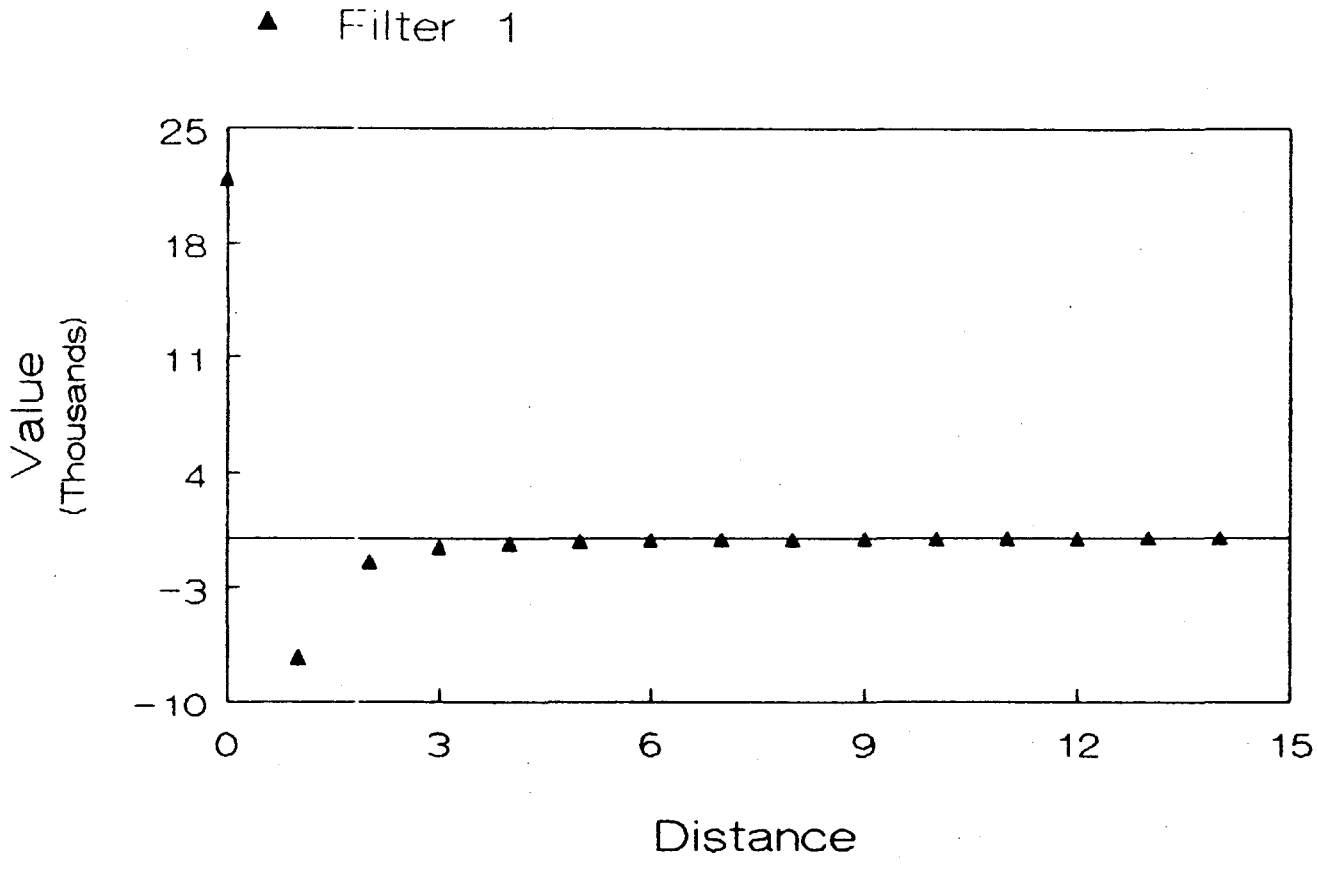

Fig. 7.13 *The discrete Butterworth filter in real space.*

To investigate the effect of the truncation of the filter, a backwards method of approach has been taken. The truncated filter in real space was represented in frequency space and the corresponding window was found.

The calculations were done using SIGPRO program. [58] SIGPRO creates and processing one dimensional, 256 sample signals.

Given the truncated filter H'(d) in real space, the filter in frequency space is:

$$G'(f) = \mathcal{F}\left[H'(d) \right] \tag{7.2}$$

where $\mathcal{F}$ denotes the Fourier transform. This is the effective filter used practically in the reconstruction of the images.

The Butterworth filter from Fig. 7.13 transfered in frequency space is presented in Fig. 7.14.

The quality of the filter is determined by the window function. The corresponding window of the truncated filter is:

$$W'(f) = G'(f)/|f| \tag{7.3}$$

To avoid the division by zero at zero frequency, the amplitude is taken the same as for frequency one.

The obtained window is presented in Fig. 7.15. The window corresponding to 15 point kernel filter in real space has an effect of amplification on the amplitude of low frequencies (up to 2 times). This effect is reflected in a preference of higher amplification of the low spatial frequencies in the reconstructed image.

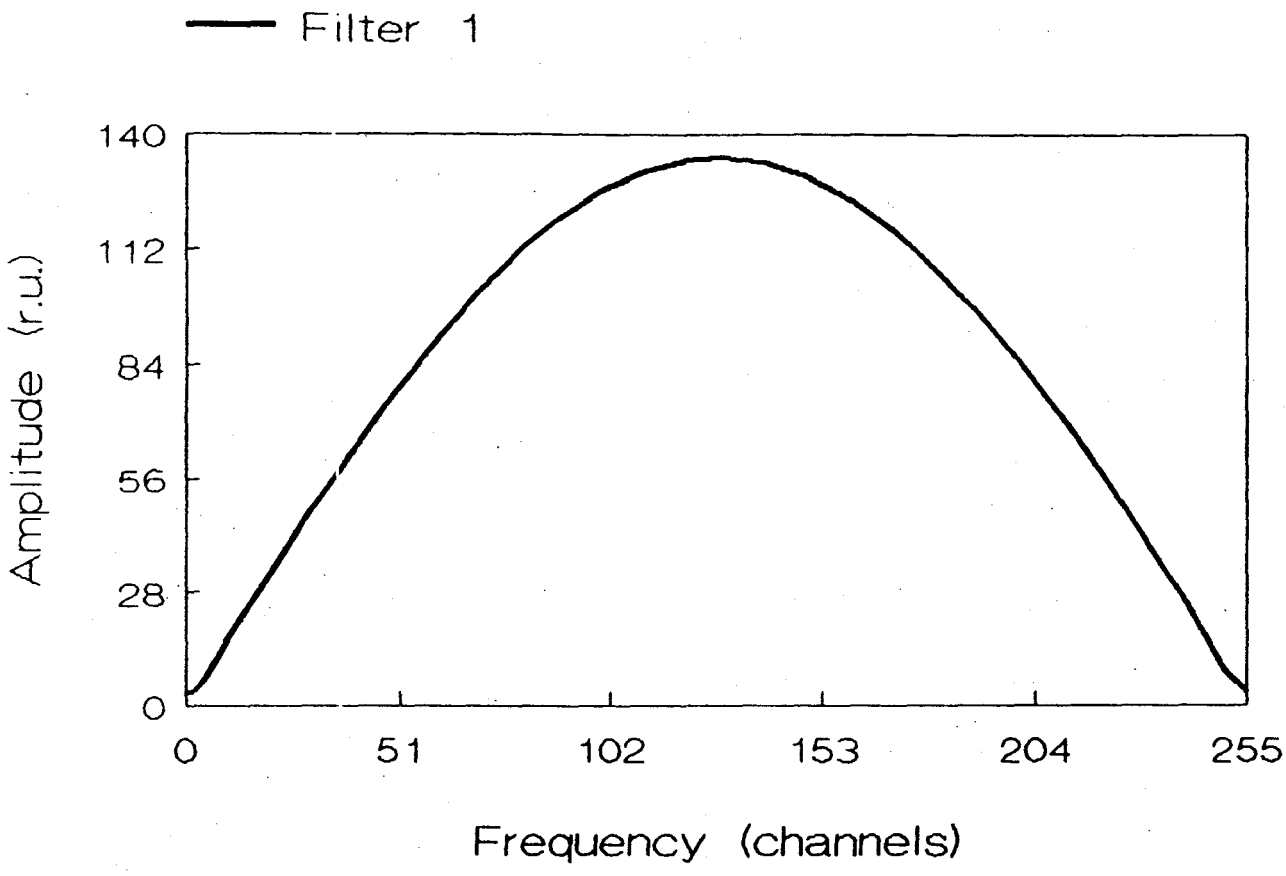

Fig. 7.14 *The truncated Butterworth filter in frequency space.*

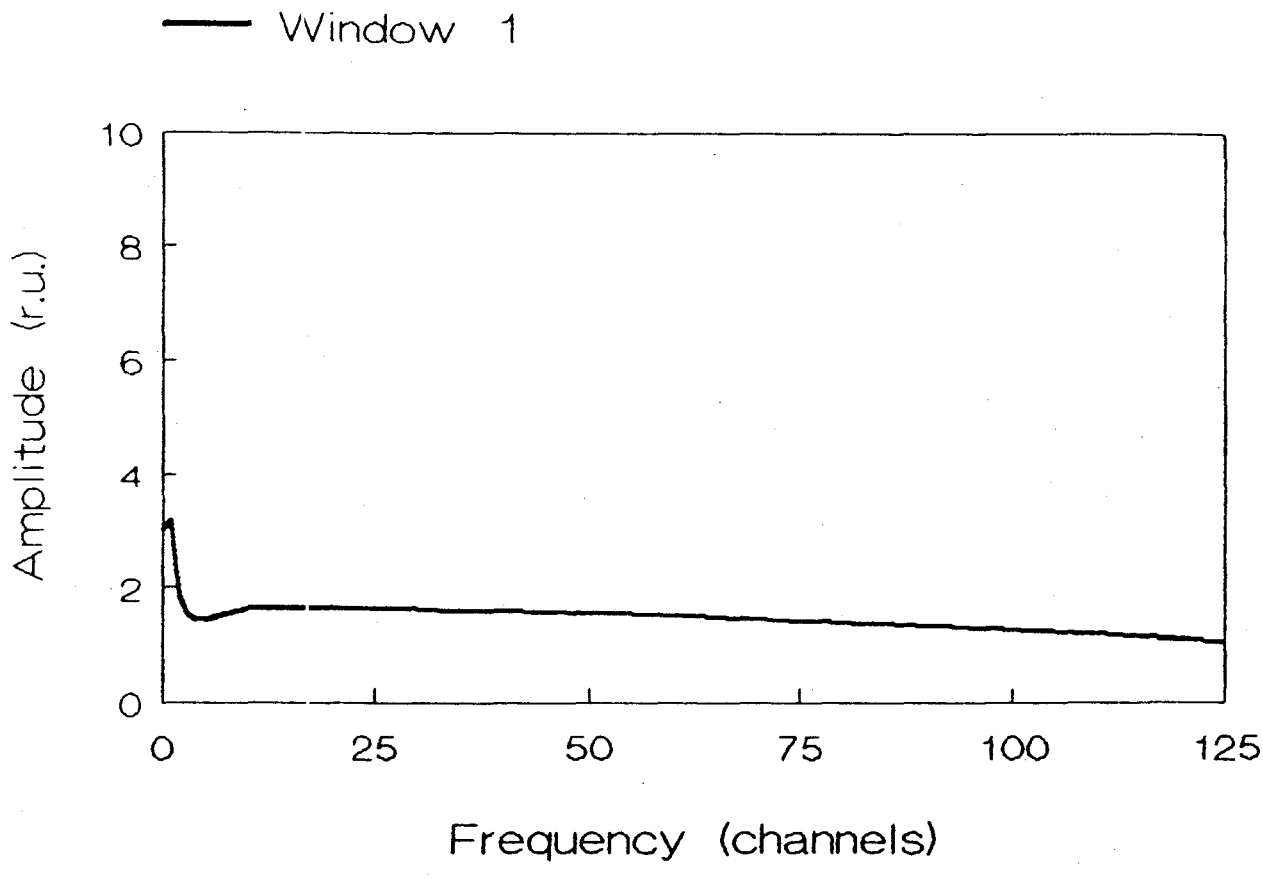

Fig. 7.15 *The window corresponding to the Butterworth filter truncated in real space at 15 points.*

The effect of the truncation of the filter in real space was studied for a Hann filter as well.

The Hann window defined in equation (3.48) is:

$$W(f) = \begin{cases} 0.5 + 0.5 \cos \dfrac{\pi f}{f_m} & \text{if } |f| \leq f_m \\ 0 & \text{if } |f| > f_m \end{cases} \qquad (7.4)$$

The corresponding Hann filter in frequency domain is, (eq. 3.49)):

$$G(f) = \begin{cases} 0.5\,|f| + 0.5\,|f| \cos \dfrac{\pi f}{f_m} & \text{if } |f| \leq f_m \\ 0 & \text{if } |f| > f_m \end{cases} \qquad (7.5)$$

In equation (7.4) and (7.5), f_m represents the maximum frequency or Nyquist frequency (eq. (3.31)).

The inverse Fourier transform of the filter in frequency space gives the filter in real space:

$$H(c) = \mathcal{F}^{-1}\left[G(f) \right] \qquad (7.6)$$

A truncation in different positions: at 15/16, 7/8, 3/4 and 1/2 distance from the origin (d = 0) of the real space Hann filter has been done. Returning these truncated filters in frequency space by Fourier transform them, the effect of truncation can be seen clearly.

Fig. 7.16 presents the Hann filters in frequency space. They have been obtainec by taking the filter from the domain space with, or without truncation. At full scale it is almost impossible to detect a difference between them. By enlarging the low frequency region scale, (Fig. 7.17), the amplitudes of the truncated filters are clearly higher than those of the initial filter. The magnitude of the amplitude at low frequency is proportional to the magnitude of the truncation of the filter in real space. The same effect of preferential amplification of the low frequencies of an image is obtained by cutting a Hann filter in real space.

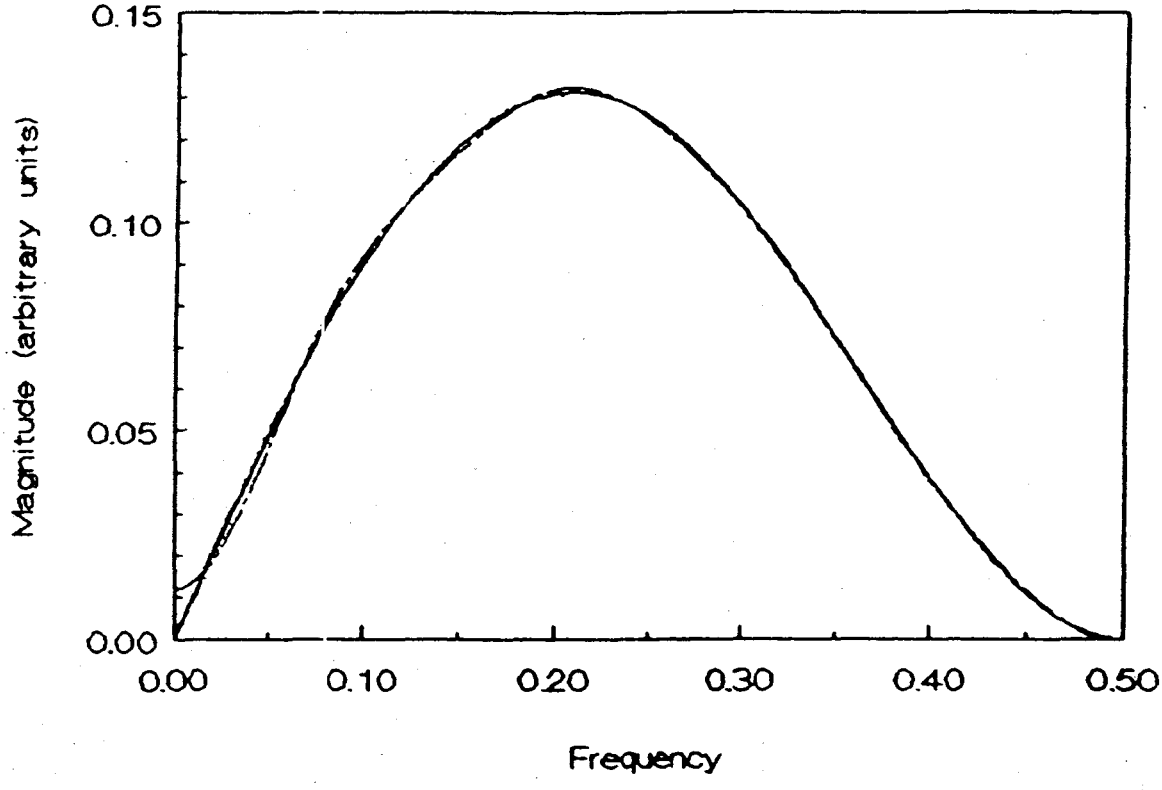

Fig. 7.16 *The Hann filters truncated in different positions in real space, represented in the frequency space, in comparison to the entire filter. At this scale no difference between them is visible.*

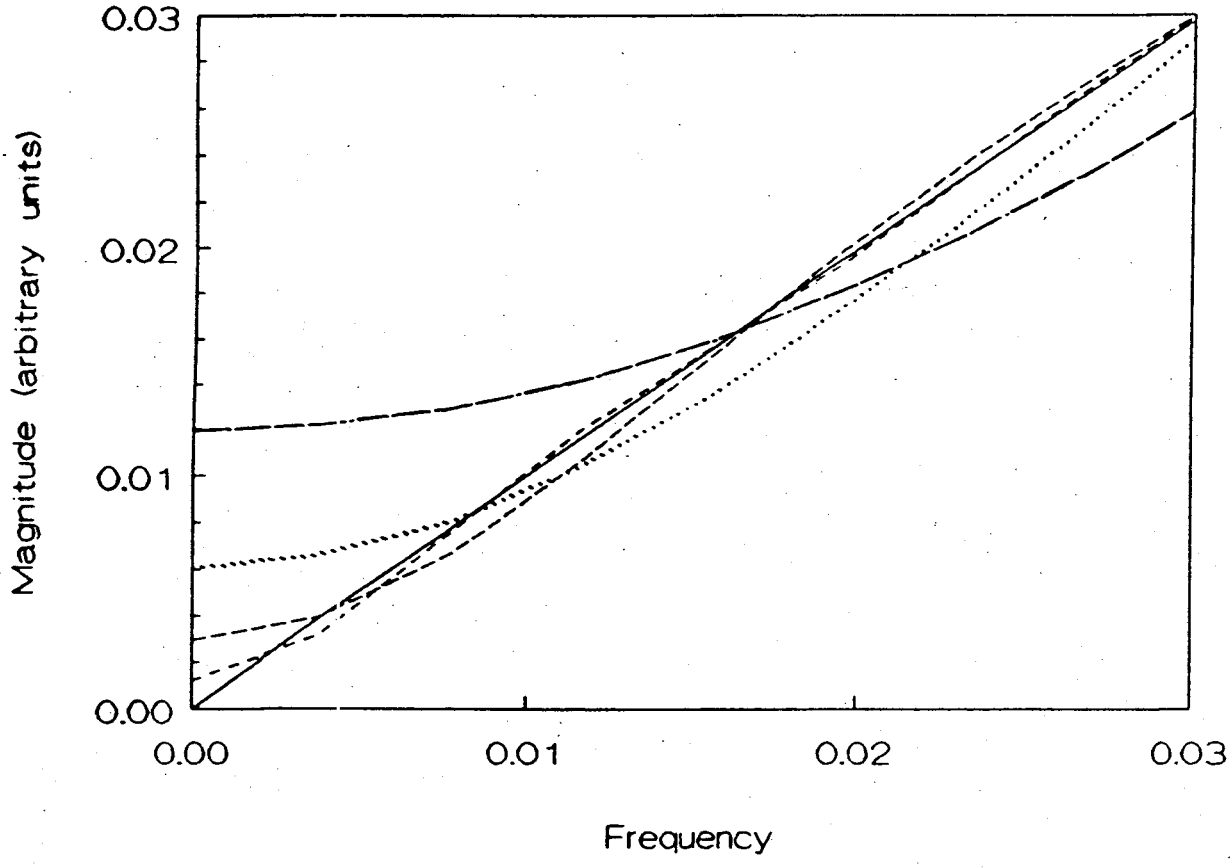

Fig. 7.17 *The low frequency region of the Hann filters.*
——— *the entire filter,*
- - - *the truncated filter at 1/2 in real space,*
— — — *the truncated filter at 1/4 in real space,*
.....*the truncated filter at 1/8 in real space,*
— — *the truncated filter at 1/16 in real space.*

A head is of a finite dimension. This is, using the entire filter in the filtered back-projection method is not logical because outside of the field of view, limited by the finite dimensions of the investigated objects, there are no experimental points. Then the question arise how the preferential amplification of the low frequencies can be avoided, making possilble the absolute quantitation of an image.

The first attempt is to follow the effect of truncation of the kernel filter in different positions in real space, trying to choose the best solution as a compromise between the necessity of truncation and the effect of amplification at low frequencies.

Fig. 7.18 illustrates the window functions corresponding to the discrete Butterworth filter truncated at different positions, so that it is defined by 3 points, 7 points, 15 points and 23 points. The effect of amplification is higher when the truncation is stronger. 15 point filter still gives unwanted amplification effects but a 23 point filter seems to be a better choice. A path ray including the coincidence of one detector with the other ± 23 detectors on the opposite side will give better images, closer to reality.

A second attempt is to modify the filter in order to avoid the preferential amplifications in frequency space compensating the effect of truncation. [60] There are different possible criteria to introduce the modification of the filter to avoid the negative effects of the truncation. In our case, the modification of the filter is performed based on the criteria of the concordance between the tumour-to-nontumour activity ratio used in the phantom and the one obtained from the image. The test value of the activity ratio is chosen 10/1 (1 μCi/ml: 0.1 μCi/ml) and the small tumour cylinder (1.8 cm diameter) is used, for different reasons. Firstly, the low concentration activity of the background corresponds to a low rate in the background of the image, which means a great sensivity in finding the best modified filter. Secondly, in this configuration of the phantom and with this low concentration activity of the nontumour region, the total activity used ($\approx$ 500 μCi) is small enough to avoid the contribution to activity reading of the random coincidences and scattering effects whose magnitude is direct proportional to the amount of activity.

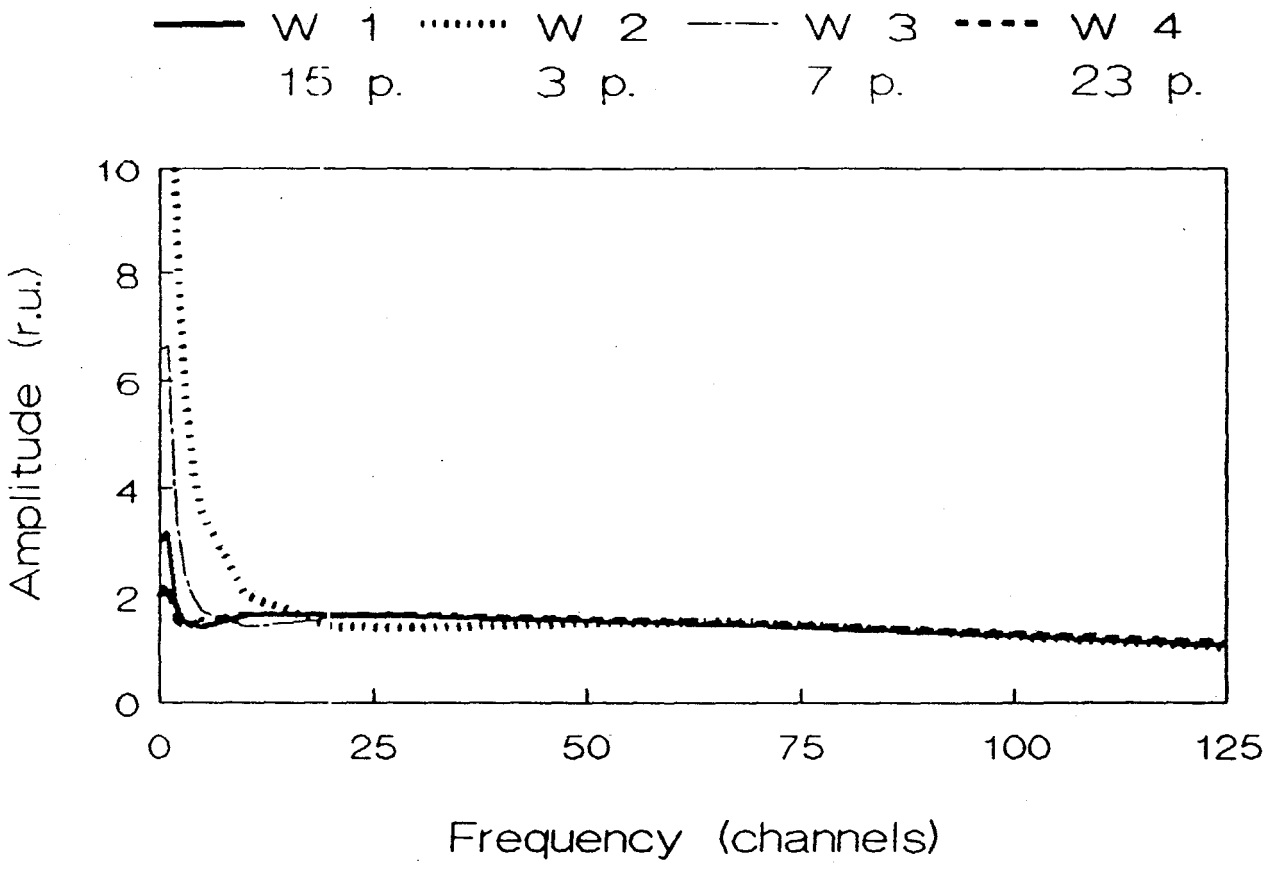

Fig. 7.18 *The windows corresponding to 3 point Butterworth filter (W2), 7 point Butterworth filter (W3), 15 point Butterworth filter (W1) and 23 point Butterworth filter (W4).*

Once the modified Butterworth filter is defined, its behaviour in frequency space is checked. Fig. 7.19 presents the modified and original 15 point filter in frequency domain. There is a very small difference between them at the maximum amplitude ($\approx 1\%$).

The low frequency region of these two filters is shown in Fig. 7.20. The modified filter has smaller amplitudes at low frequencies having almost a normal behaviour.

Fig. 7.21 presents the two corresponding window functions. The window of the modified filter does not present amplifications of the low frequency region such as the truncated filter.

Therefore, a truncated convolving function can be obtained, so that the reconstructed image is the same as for a nontruncated filter. Under these circumstances, the filtered back-projection should accurately reproduce the contours and the density changes of the activity distribution in the slice of brain under investigation. [60]

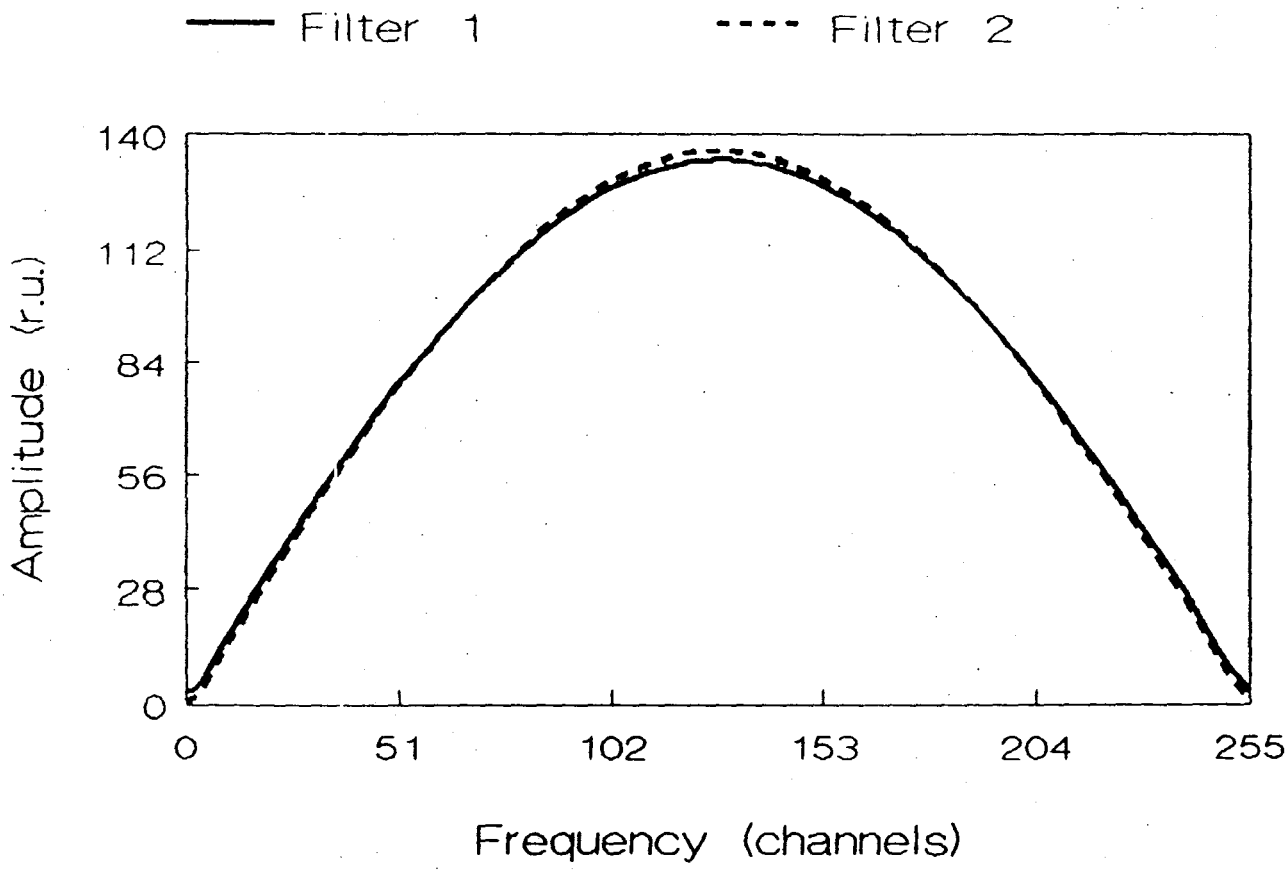

Fig. 7.19 *The truncated Butterworth filter* (Filter 1) *and the modified filter* (Filter 2), *in frequency space.*

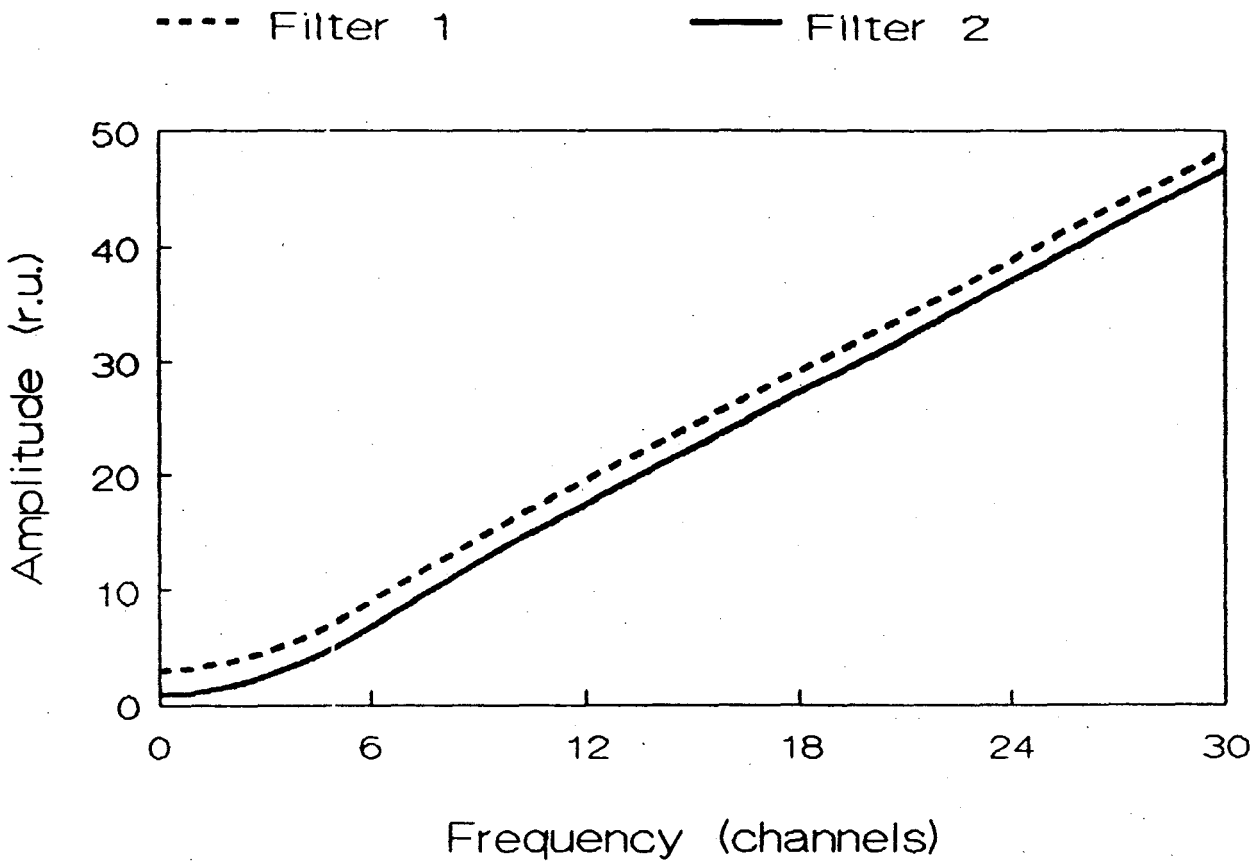

Fig. 7.20 *The truncated Butterworth filter* (Filter 1) *and the modified filter* (Filter 2) *in the low frequency region.*

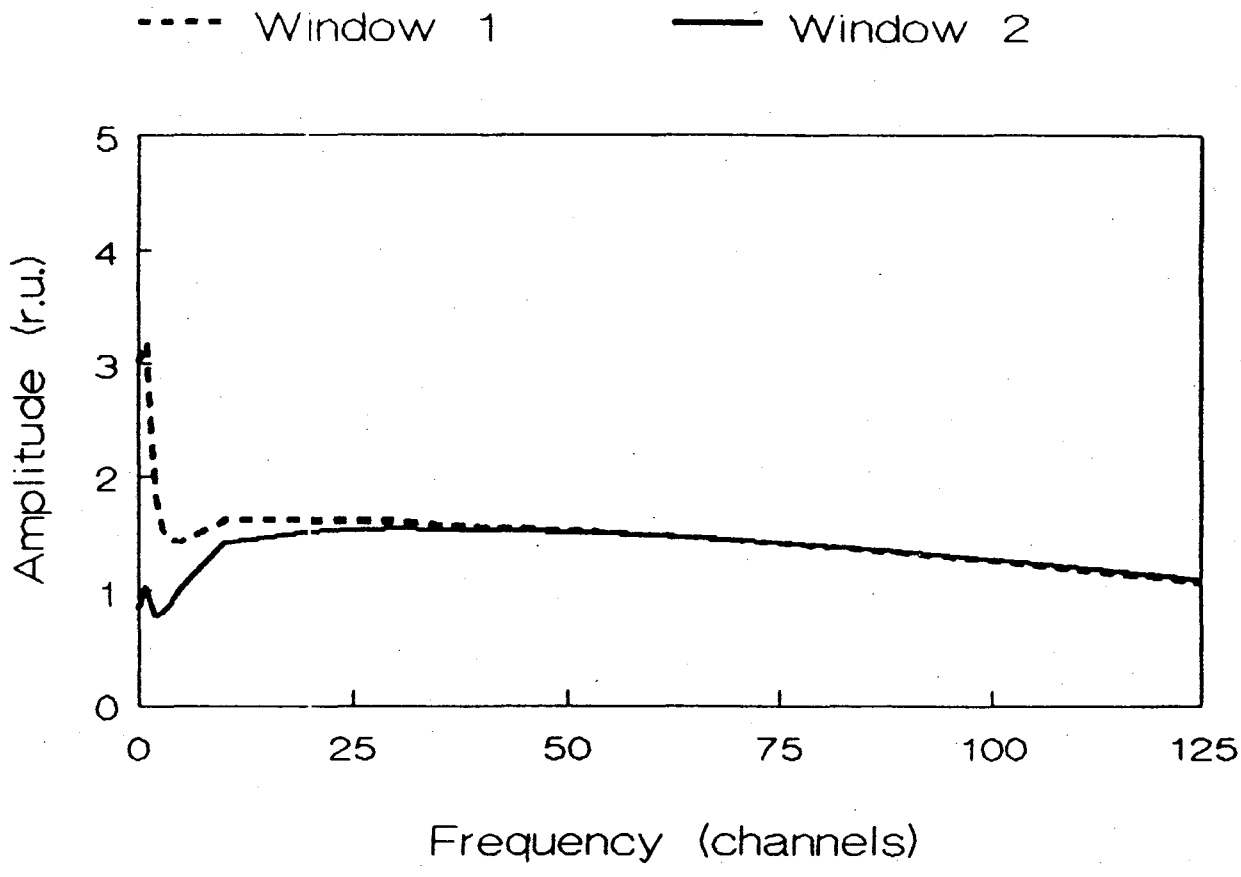

Fig. 7.21 *The windows corresponding to the truncated Butterworth filter* (Window 1) *and modified filter* (Window 2).

7.5 The tumour-to-nontumour activity ratios.

The difference between the detected activity by computer assisted tomograph system and actual concentration distribution in a portion of the body is dependent on:

- the volume of the tumour (organ),
- the volume of contiguous tissues,
- the target-to-nontarget ratios, and
- the isotope concentration. [49]

There are different methods to evaluate the concentration activities.

The *threshold method* consists of empirically eliminating the counts arising due to surrounding activity (predefined threshold value) from the reconstructed image. A systematic background count, (believed to be related to undercorection for attenuation in [57]) is taken as *a correction term*. The problem develops when different studies define different thresholds in order to achieve the true concentration activity and the volume of the target from the image. [57, 66] This is probably due to the fact that their filters were truncated in different positions. Consequently, the magnitude of background noise generated by the filtering process was different from one study to another study.

Another method, [54] calculates a concentration activity for each region of interest defined in the image. When region of interest data are extracted from the image, various strategies have been devised to circumvent limitations as: partial volume effects, filtering effects, physical factors not eliminated before the reconstruction etc. Some of the strategies attempted are: averaging the entire region of interest to reduce noise or using the maximum pixel value as the region average in regions known to exceed the average value of the surrounding neighborhood (such as gray matter structures in glucose metabolism studies). The idea is that optimal methods for extraction of region of interest must be developed.

These two methods of concentration activity evaluations present a great deal of subjectivity, their result being difficult to trust.

A more logical approach to quantitate, is to perform a test procedure to evaluate the performances of the tomograph in sensivity, resolution, count rate capabilities etc., and to introduce the determined corrections in the reconstructed image.

This approach of correcting all variables that can theoretically affect quantitation is extremely complicated since the subject is the human body with its range of topographical and individual variations.

The greatest obstacle to quantitation of radionuclides by computer assisted tomography methods relates to the problem of accounting for racionuclides in the surrounding tissues is the opinion expressed in [61]. To suppress the noise in a high noise reconstruction environment, a special filter based on the signal-to-noise ratio is proposed in [61].

The reconstruction filter was adjusted in [51] to provide final images of ^{18}FDG brain simulations with a low noise level.

In this study, the filter was designed to give an experimental image which reflects as closely as possible the reality, while conforming to the practical restrictions imposed by the measurements.

The truncation of the filter generates an amount of noise which seems to be much higher than all other kinds of noise summed together. This is seen in the target-to-nontarget activity ratios obtained using this filter in comparison to the modified filter (Table 7.1).

Table 7.1 Tumour-to-nontumour activity ratios.

Phantom	Image	
	Truncated filter	Modified filter
10.0	6.10 ± 0.95	11.63 ± 0.93
5.0	2.70 ± 0.14	5.85 ± 1.25
3.6	1.78 ± 0.17	3.70 ± 0.55

The experimental rate values are obtained as average values and statistical uncertainties per pixel, from more than 100 high statistical images. The uncertainty in a rate evaluation from an image pixel (either from a tumour image or from the background) was always in statistical limits.

The modified filter was defined at the tumour-to-nontumour activity ratio of 10/1. The tumour image readings are the same (in statistical limits) regarding of the filter used. The quantitative difference between them occurs in the image background rate obtained with these two filters as seen in Fig. 7.22. The background rate per pixel for the 15 point Butterworth filter (Filter 1) and the modified filter (Filter 2) versus the number of counts (per pixel) accumulated in the background is presented in Fig. 7.22. The truncated filter gives a constant background rate twice larger than it should be. This could not be due to the contribution from scattering or accidental coincidences because the total activity used in the phantom was very small ($\approx$ 0.5 mCi).

The very low statistical images (less than 10 counts/pix in the tumour region) present a higher background rate, almost the same, regardless of the filter used. This effect is due to star artifact generation. Between 10 counts/pix and 100 counts/pix in the tumour image, the background rate obtained using the truncated filter shows a slightly, hard to explain increase, up to the constant value of the high statistical images.

At lower tumour-to-nontumour activity ratios in the phantom (higher background concentration activity) 5/1 and 3/1, the modified filter gives the same, close to the reality, ratios unlike the cut filter, as seen in Table 7.1.

The highest total activity used (3/1 ratio) was $\approx$ 1.5 mCi which does not give yet dangerous contributions from scattered and accidental coincidences.

The advantage of using the modified filter is evident in the study of a cold tumour (no activity in the tumour cylinder and activity in the phantom). The distribution of counts as a function of distance (number of pixel) in the image of an 1.8 cm diameter cold tumour obtained using the 15 point filter and the modified filter is presented in Fig. 7.23.

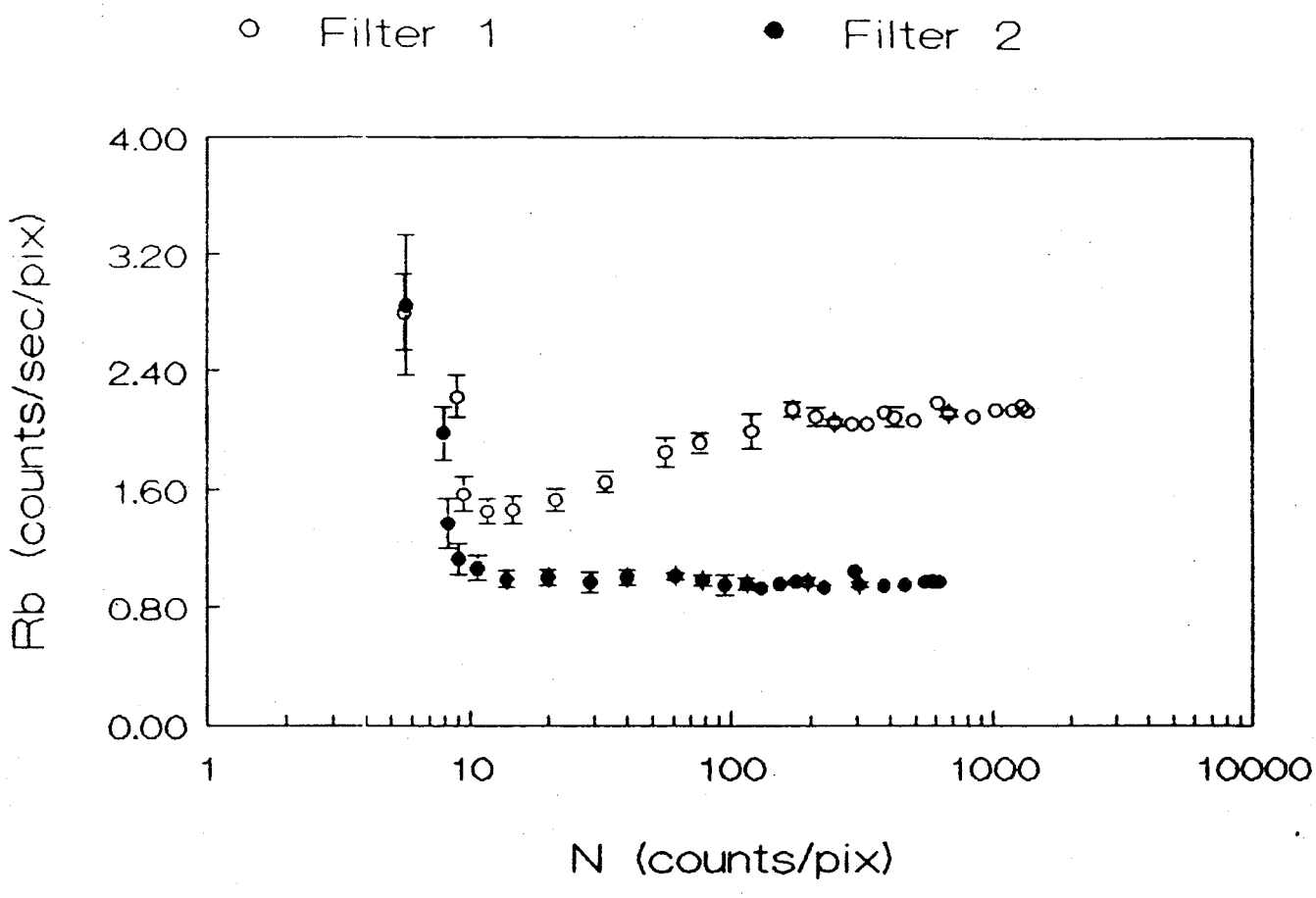

Fig. 7.22 *The background rate* (0.1 μCi/ml) *as a function of the number of events accumulated in the background region* (1 μCi/ml), *in a reconstructed image using two filters, the truncated filter* (Filter 1) *and the modified filter* (Filter 2).

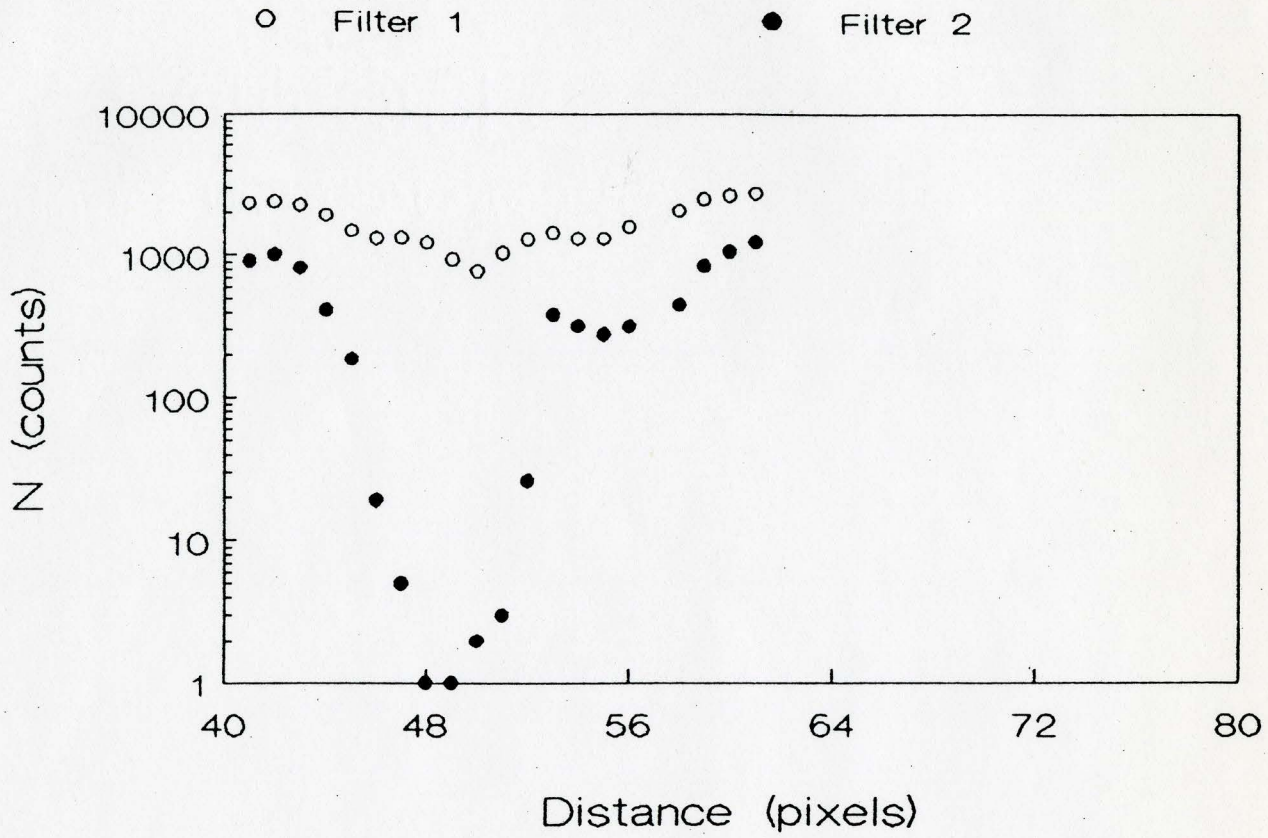

Fig. 7.23 *The image of a cold tumour* (1.8 cm *diameter) reconstructed using the truncated filter* (Filter 1) *and the modified filter* (Filter 2).

The high noise generated by the truncated filter makes almost impossible to detect the cold tumour. Unlike this truncated filter, the modified filter creates a normal image of a cold tumour. Moreover, this image can be submitted to quantitation: its *position*, its dimension and even its concentration activity (if it is different of zero) can be evaluated.

7.6 The calibration of the tomograph.

Earlier works, [63, 64] briefly describe the procedure of the calibration of their tomographs.

For the Mark IV System, the calibration obtained is expressed as:

$$A(\mu Ci/ml)_{brain} = H\ K(counts/pix)_{brain} \qquad (7.7)$$

where A is the average local concentration of activity in the brain, H is an experimentally determined factor correcting for the difference in size between the reference cylinder and the head at the level of section, and K is the calibration constant obtained from scanning the reference cylinder.

The data presented in [64] are obtained for two different diameter phantoms: 18 cm and 28 cm. The reconstructed images followed the true concentration activity ratios used in the phantom. After the decay time corrections for ^{11}C, they produced an unique line of calibration for both dimensions of the phantoms. In this case, the only observation can be related to the fact that this calibration was not tested for very small tumours, 18 cm and 28 cm diameter phantoms being too close to each other. It is very probable that they used a right filter.

Therefore, the last step in obtaining a reconstructed image expressed in absolute units at McMaster Hospital tomograph is to calibrate the tomograph in concentration activity units ($\mu Ci/ml$).

The concentration activities were measured in 1 ml sample using a Ge(Li) detector. The concentration activity is:

$$A(\mu Ci/ml) = \frac{1}{3.7\ 10^{4}} \frac{N}{t} \frac{c}{\varepsilon\ b} \qquad (7.8)$$

where N is the total number of counts accumulated in the 511 KeV energy peak (after the substraction of the background events), t is the time of acquisition (sec), b is the branching ratio of the isotope (0.88 for ^{68}Ga), $\varepsilon = 2.94\ 10^{4}$ is the detector efficiency at 20 cm distance, and c = 5.04 is the correction factor for measurements at 50 cm distance. Shortly:

$$A(\mu Ci/ml) = \frac{K\ R}{b} \qquad (7.9)$$

where K represent the detector constant for measurements at 50 cm, and R is the rate of counts in 511 KeV energy peak.

The calibration of the tomograph was performed using ^{68}Ge-^{68}Ga solution, taking advantage of the constant activity in time. [62] Two concentration activities were used in the tumour cylinder and other 4 concentration activities in the nontumour region of the 25 cm diameter phantom. The time of acquisition of an image was long enough to avoid unwanted effects of the low statistical images. The reconstruction of the images was obtained using the 15 point Butterworth filter (Filter 1) and the modified filter (Filter 2).

Fig 7.24 presents the calibration of the tomograph for these two filters. The rate of counts (counts/sec/pix) obtained from the image is represented as a function of the concentration activity (μCi/ml) used in the phantom.

The truncated filter gives a calibration dependent on the volume. For the 1.8 cm diameter of the tumour and 25 cm diameter of the phantom, two different linear dependencies are obtained. The rate of counts corresponding to surrounding tissue are shifted to higher rates due to amplification effects generated by this filter at low spatial frequencies. This means that, a family of lines of calibration dependent on the dimension of the object is obtained using a truncated filter. The real activity in the image can be calculated only using the calibration line corresponding to each investigated volume. This explains why the difference between the detected activity and the real activity was dependent of the volume of the organ (tumour) and the volume of surrounding tissues as the authors [49] declare.

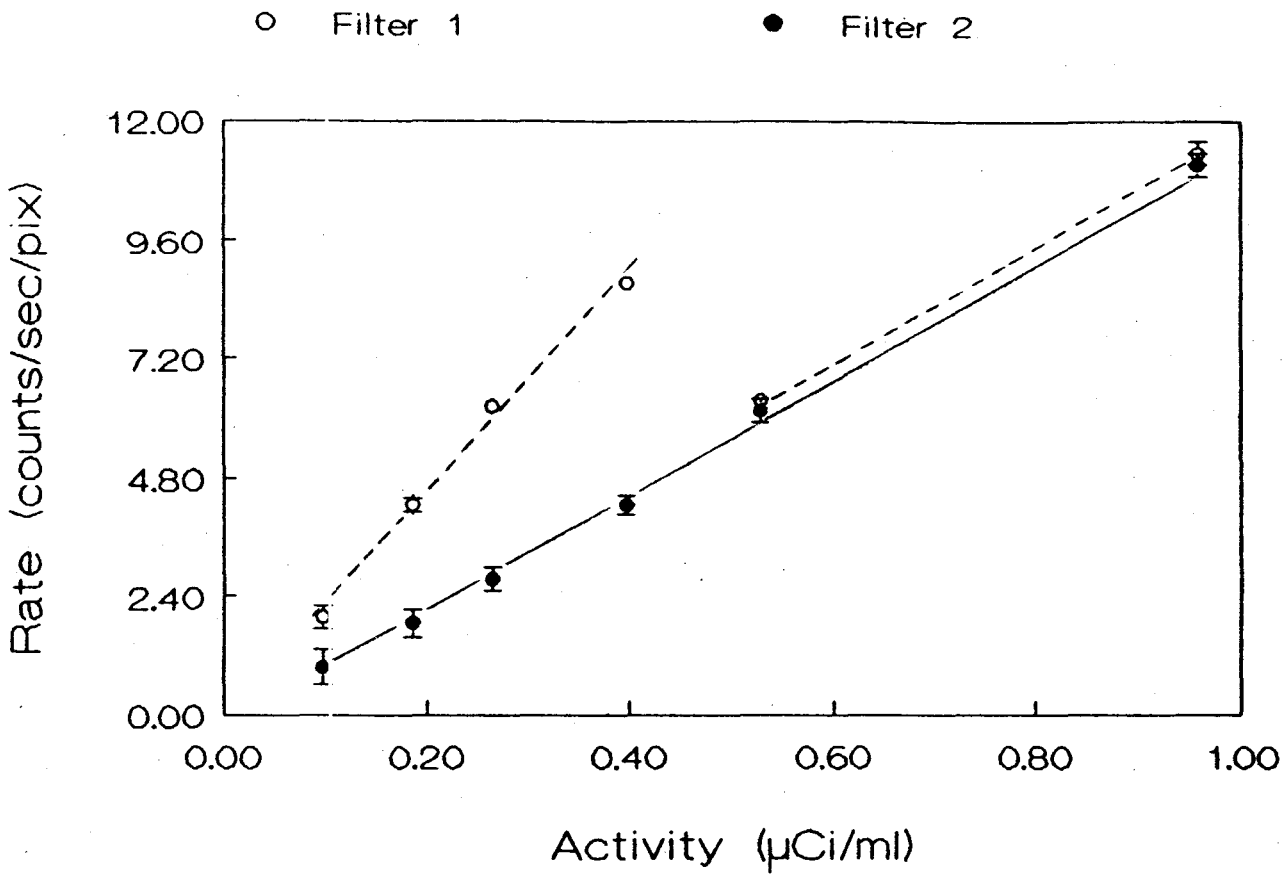

Fig. 7.24 *The calibration of the tomograph for* ^{68}Ge-^{68}Ga *solution for the two filters used in the reconstruction of the image, the truncated filter* (Filter 1) *and the modified filter* (Filter 2). *The dependence of the rate of counts (per pixel) in the image on the concentration activity used in the phantom is presented.*

One line of calibration, usually determined with a large phantom, ≈ 25 cm diameter for the brain images, can not be applied to smaller volumes. Moreover, if the calibration of the tomograph is realized using a 25 cm diameter phantom, the correct quantitation of the concentration activity could be obtained in the background region (nontumour tissues) and not in the tumour region, when a truncated filter is used.

Unlike this cut filter, the proposed modified filter (Filter 2) realizes an unique linear calibration regardless of the dimension of the objects under investigation. The tumour calibration lines obtained using the truncated filter and the modified filter coincide. The difference between them occurs for the large 25 cm diameter phantom when the truncated filter overestimates the rate of counts.

Therefore, the modified filter eliminates the dependence of the image rate of events on the volumes and tumour-to-nontumour activity ratios, leaving only the dependence on the real activity.

Once the calibration of the tomograph realized for $^{68}Ge-^{68}Ga$ solution, the calibration lines corresponding to any other β^+ isotope can be easily found. In the dependence of the rate of events on the concentration activity, the only factor changing from one β^+ isotope to another β^+ isotope is the branching ratio. The other values, including the rate of counts, the detection efficiency etc., are the same because the same 511 KeV γ rays are detected. Consequently, the similar calibration lines expected for ^{18}F (b = Ø.97) and ^{64}Cu (b = Ø.19) are presented in Fig. 7.25.

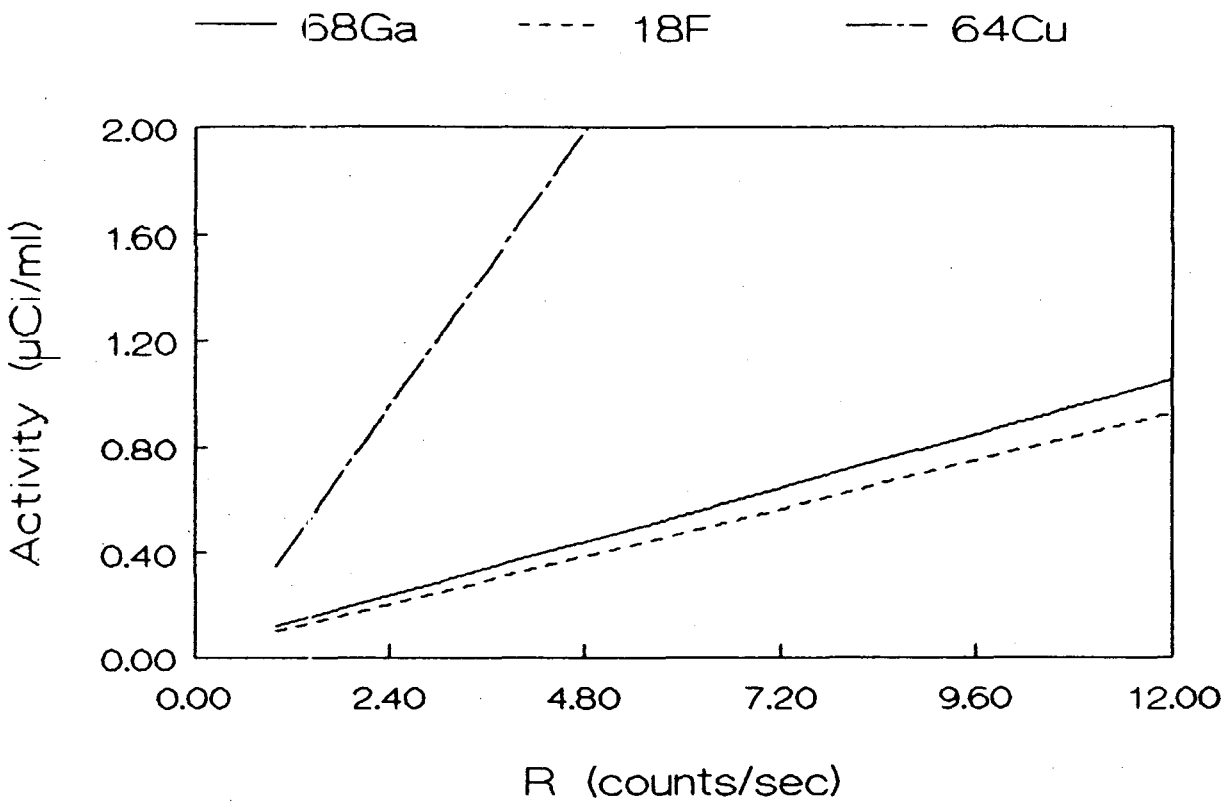

Fig 7.25. *The calibration of the tomograph for* ^{18}F, ^{68}Ga *and* ^{64}Cu.

8. THE APPLICATION OF THE METHOD FOR SHORT LIVED ISOTOPES.

The radionuclides used in PET are very short-lived isotopes. That is, the concentration activity of a radiotracer in the body is changing with time. There is no better way to verify the accuracy of this method for absolute quantitation than to compare the activity variations with time of a short-lived isotope obtained by an universally accepted method (Ge(Li) detector) and this method.

The activities of 1 ml samples from the solutions used in PET phantom experiments are measured with a Ge(Li) detector at the same time with PET. Beforehand, the Ge(Li) detector was calibrated using 1 ml ^{68}Ge-^{68}Ga solutions of known concentration activities. The calibration line of Ge(Li) detector used, showing the dependence of the activity (μCi/ml) on the rate of counts, is presented in Fig. 8.1. Again, the calibration lines corresponding to any other isotopes (^{18}F or ^{64}Cu) can be obtained for the Ge(Li) detector, taking into consideration the differences between their branching ratios and that of ^{68}Ga.

8.1. ^{18}F experiment.

In the first experiment, the 25 cm diameter phantom filled with ^{18}F solution is tested. [67] The images were taken at approximately 10 minutes interval for a total of $\approx$ 400 minutes (6.5 h). The acquisition time of an image was long enough to avoid low statistical effects presented before.

As usual, to verify the detection system functionality, the rate of detected events of each image slice acquired was registered. The change of this detected events in time is presented in Fig. 8.2. The linear dependence (in logarithmic scale) proves that the detection system was working well. The half-life of ^{18}F obtained from this dependence is 101 min.

Fig. 8.3 presents the total rate of the image (the total number of counts of a reconstructed image divided by the time of acquisition) as a function of time for both filters used in this study, 15 point filter (Filter 1) and modified filter (Filter 2).

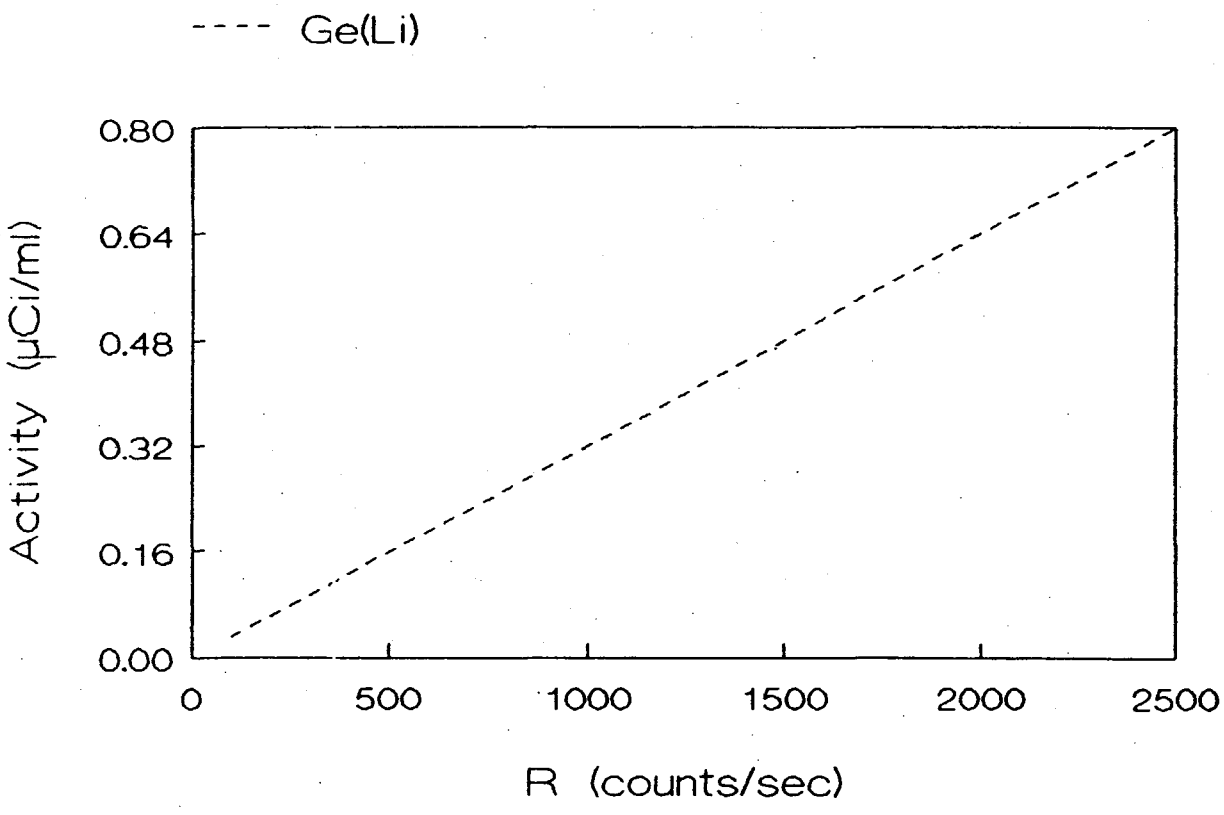

Fig. 8.1 *The calibration of the* Ge(Li) *detector in concentration activities. The concentration activities versus rate of detected events is represented.*

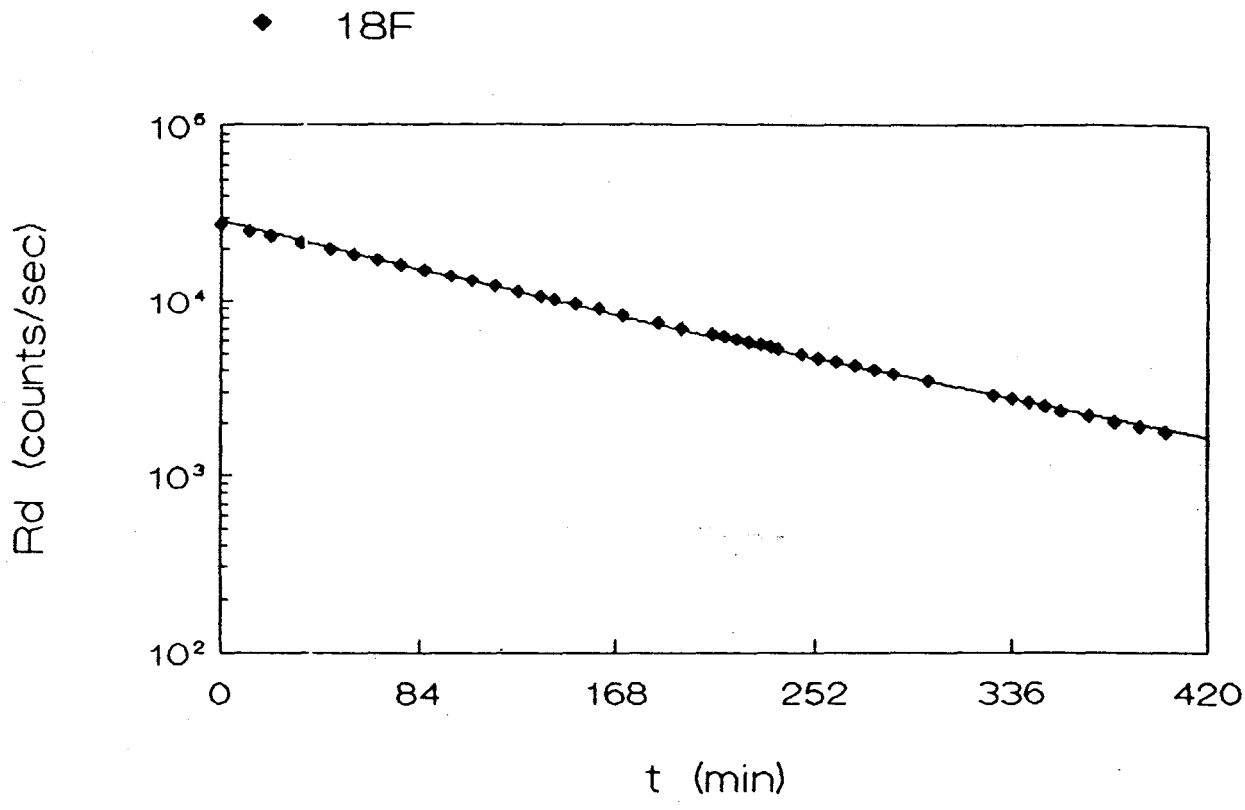

Fig. 8.2 *The dependence of the rate of detected events on the time for a* 25 cm *diameter phantom filled with* ^{18}F *solution.*

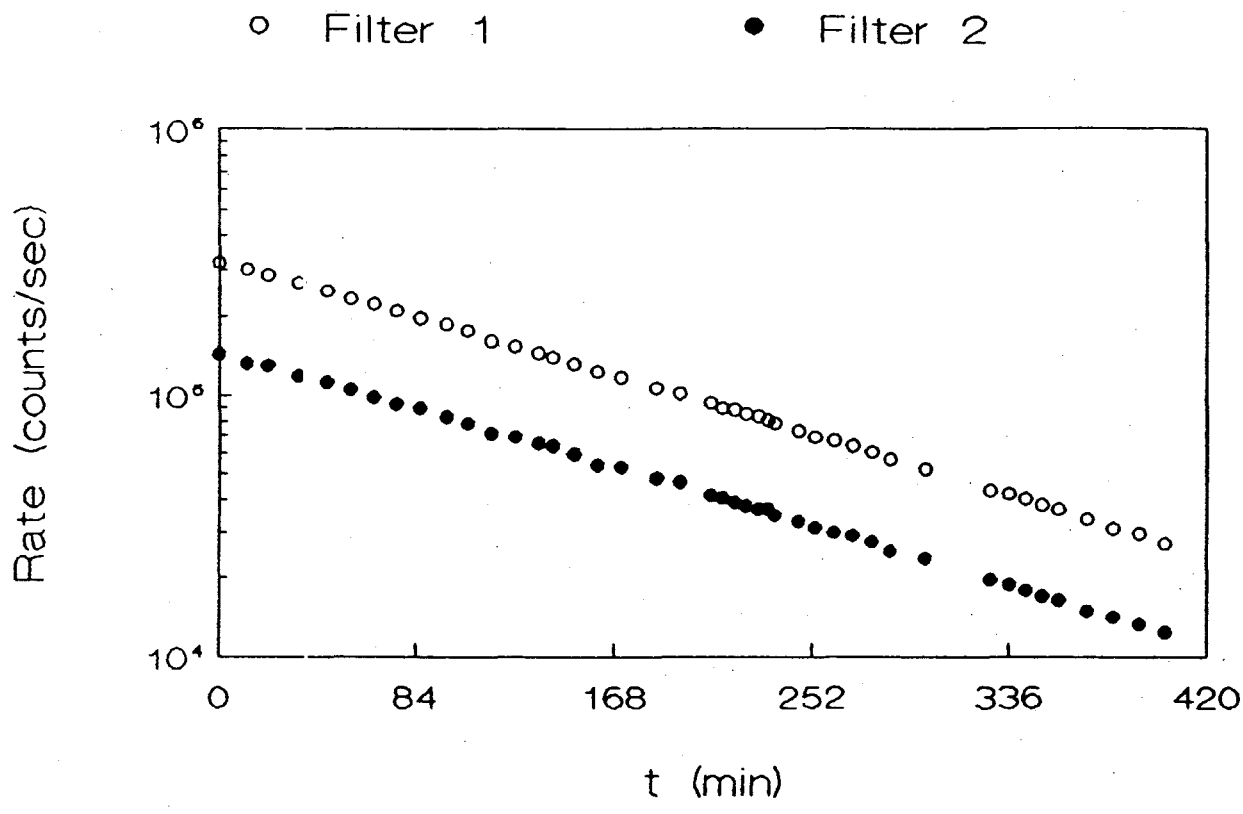

Fig. 8.3 *The total rate obtained in the reconstructed image of a* 25 cm *diameter phantom using the truncated filter* (Filter 1) *and the modified filter* (Filter 2), versus time.

This total rate of counts is important to follow to be sure that no strange amplification effects occur due to reconstruction of the image, as in low statistical cases. The linear dependence of the total rate in time in the reconstructed image proves that the filtering process was always in the constant amplification region (Fig. 7.12).

The half life obtained from this total rate dependence on time is the same for both filters used, $T_{1/2}$ = 113 min.

To analyze the image, a 40 X 40 ROI was chosen to obtain the average number of counts per pixel with small statistical errors. The rates of counts per pixel versus time are represented on Fig. 8.4, for 15 point Butterworth filter (Filter 1) and for modified filter (Filter 2). Due to a longer acquisition time, the rate values are considered to belong to the middle point of the time interval.

The same expected linear dependencies of the rate of counts on time are obtained for both filters used in the reconstruction of the image. Moreover, the half-lives obtained for ^{18}F are the same, $T_{1/2}$ = 113 min.

Using the calibration of the tomograph for ^{18}F (Fig. 7.25), the rate of counts per pixel can be translated in concentration activity. The variation of ^{18}F concentration activity versus time given by PET method is presented in Fig. 8.5. The PET values obtained using the truncated filter (Filter 1) and its calibration line for the 25 cm diameter phantom (Fig. 7.24), practically coincide with PET data obtained using the modified filter (Filter 2) and its calibration line (Fig. 7.24).

The rates of counts of 1 ml samples measured using Ge(Li) detector, in the same time with PET acquisition data, are translated into concentration activities as well. To avoid the losses of events at high rates due to dead time of the detector, the Ge(Li) data were obtained from measurements at low rates and the line extrapolated at t = 0. That is, the activity evaluations from Ge(Li) measurements in Fig. 8.5 are corrected for the dead time of the detector. To determine the accuracy of the method for absolute evaluations in PET, the Ge(Li) data are represented on the same graph with PET data.

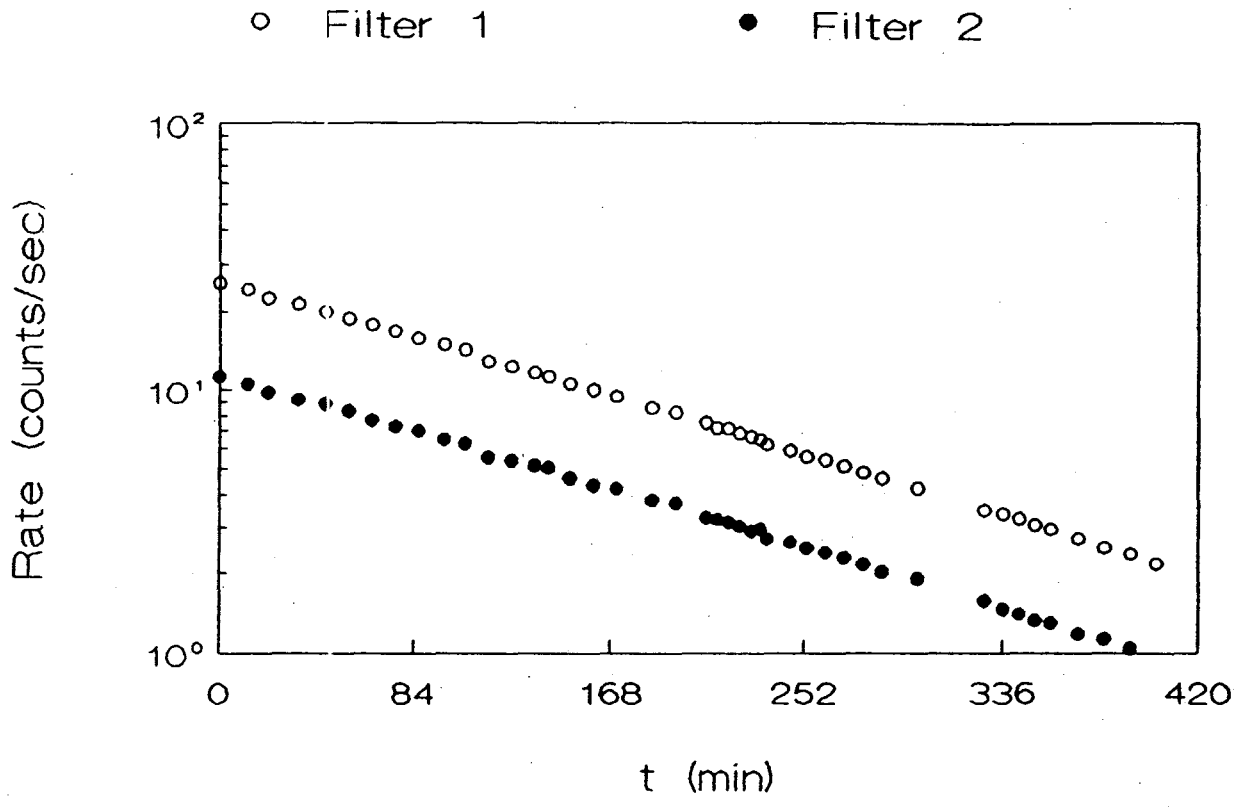

Fig. 8.4 *The rate of events per pixel versus time in the image of the* 25 cm *diameter phantom filled with* ^{18}F *solution obtained using the* 15 *point filter and the modified filter.*

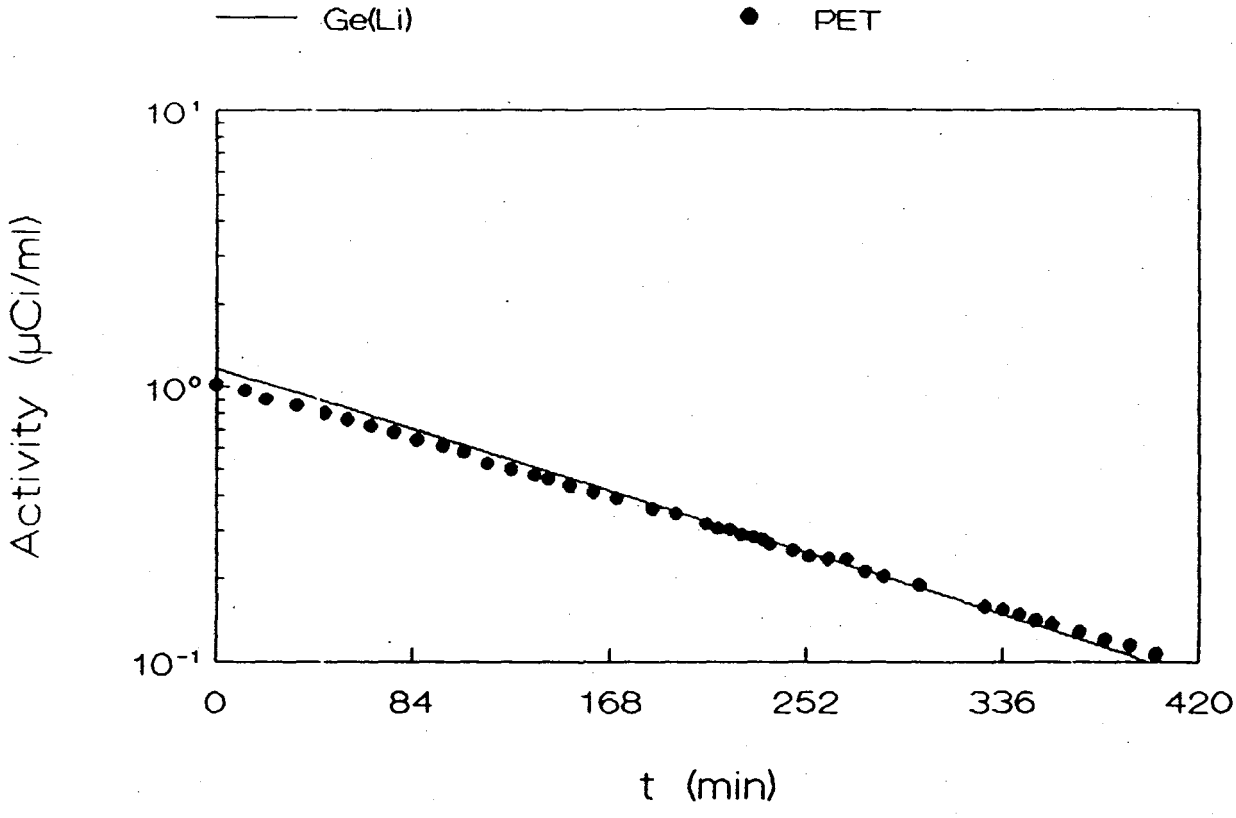

Fig. 8.5 *The variation of the* ^{18}F *concentration activity in time in the 25 cm diameter phantom obtained using* Ge(Li) *detector (full line) and* PET *method (points).*

The concordance between PET and Ge(Li) detector evaluations is almost perfect. A small difference between these two methods occurs at the beginning of the experiment. The starting concentration activity given by Ge(Li) detector is 1.2 μCi/ml which means $\approx$ 6 mCi in the entire phantom. For these activities, the effective dead time of the PET detection system becomes very important. It seems that the effect of loosing events due to dead time at high activities not only compensates but exceeds the sum of random and scattering coincidences.

From this experiment, the accuracy of the method for absolute evaluations of concentration activity with the use of PET is the best for rates of detected events less than $\approx$ 14000 counts/sec. Higher rates need dead time corrections.

8.2 ^{64}Cu and ^{18}F experiment.

A more complicated experiment is to use two different short lived isotopes in the phantom at the same time. ^{64}Cu ($T_{1/2}$ = 12.7 h) solution was introduced in the 1.8 cm tumour cylinder diameter and the phantom was filled with ^{18}F solution. The measurements by PET were done in parallel with Ge(Li) activity evaluations of 1 ml samples from each solution. [67]

The decay of ^{64}Cu isotope was observed for $\approx$ 3 days, or 3000 min. In the first day, ^{64}Cu and ^{18}F isotopes coexisted, after that the ^{18}F disappeared and only ^{64}Cu survived.

Fig. 8.6 presents the dependence of the rate of counts corresponding to the maximum of the Gaussian distribution of events versus time, for the modified filter. The line represents the extrapolation of the low rate data. The slope of the line gives a half-life for ^{64}Cu of 12.6 h.

The variation of the background rate (^{18}F) in time, obtained from 40 X 40 ROI using modified filter is presented in Fig. 8.7. The rate values at the beginning of the experiment are underestimated compared to these values obtained by extrapolating the last part of the linear dependence. If a nonparalysable system is considered, the dead time at t = 0 from the ^{18}F line is (eq. (4.10)), τ_d = 7 msec. The slope of the ^{18}F line gives the same 113 min half life for ^{18}F.

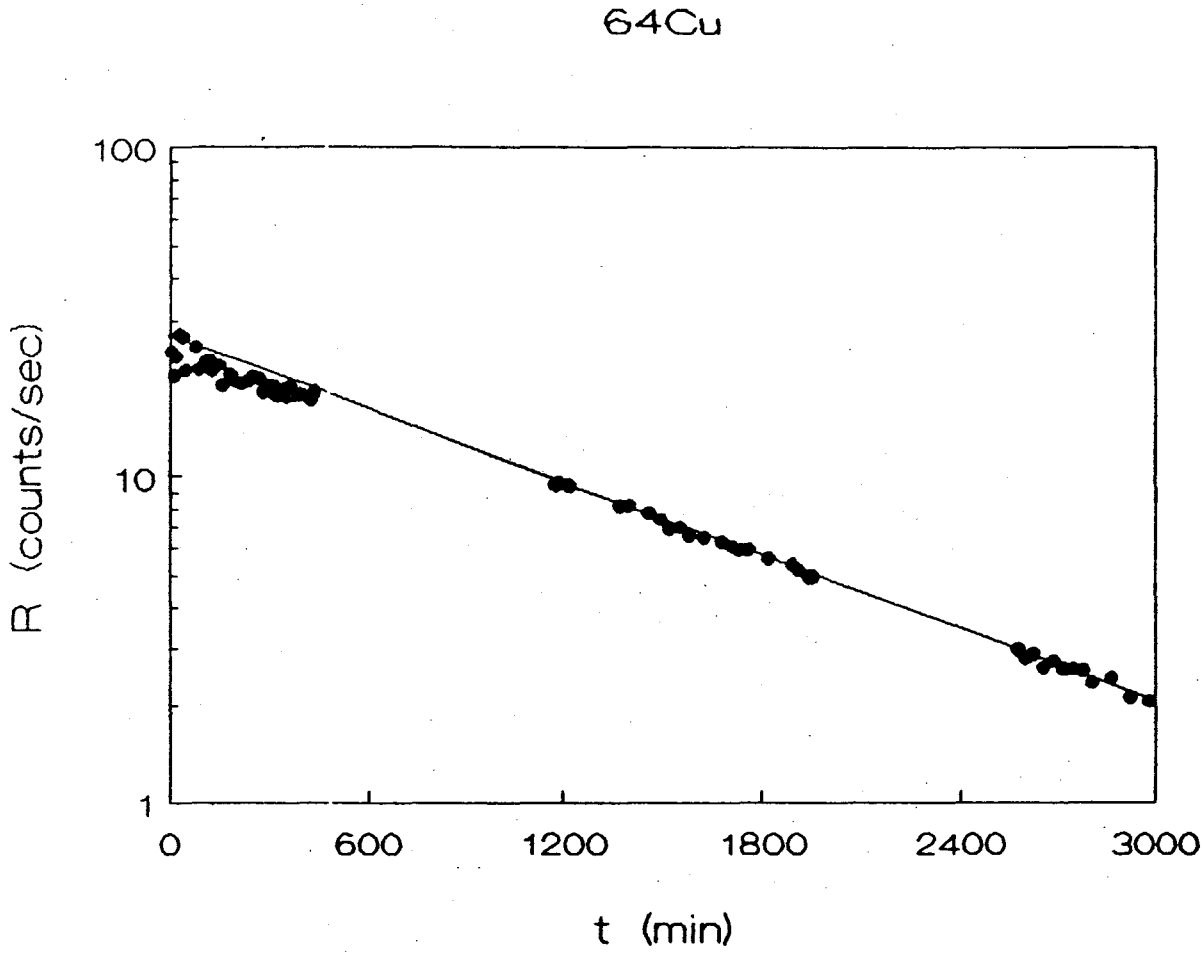

Fig. 8.6 *The variation of the rate of counts in time, in the image of the* 1.8 cm *diameter tumour filled with* ^{64}Cu *solution and sunk in* ^{18}F *background activity. The line represent the extrapolation of the low count rates.*

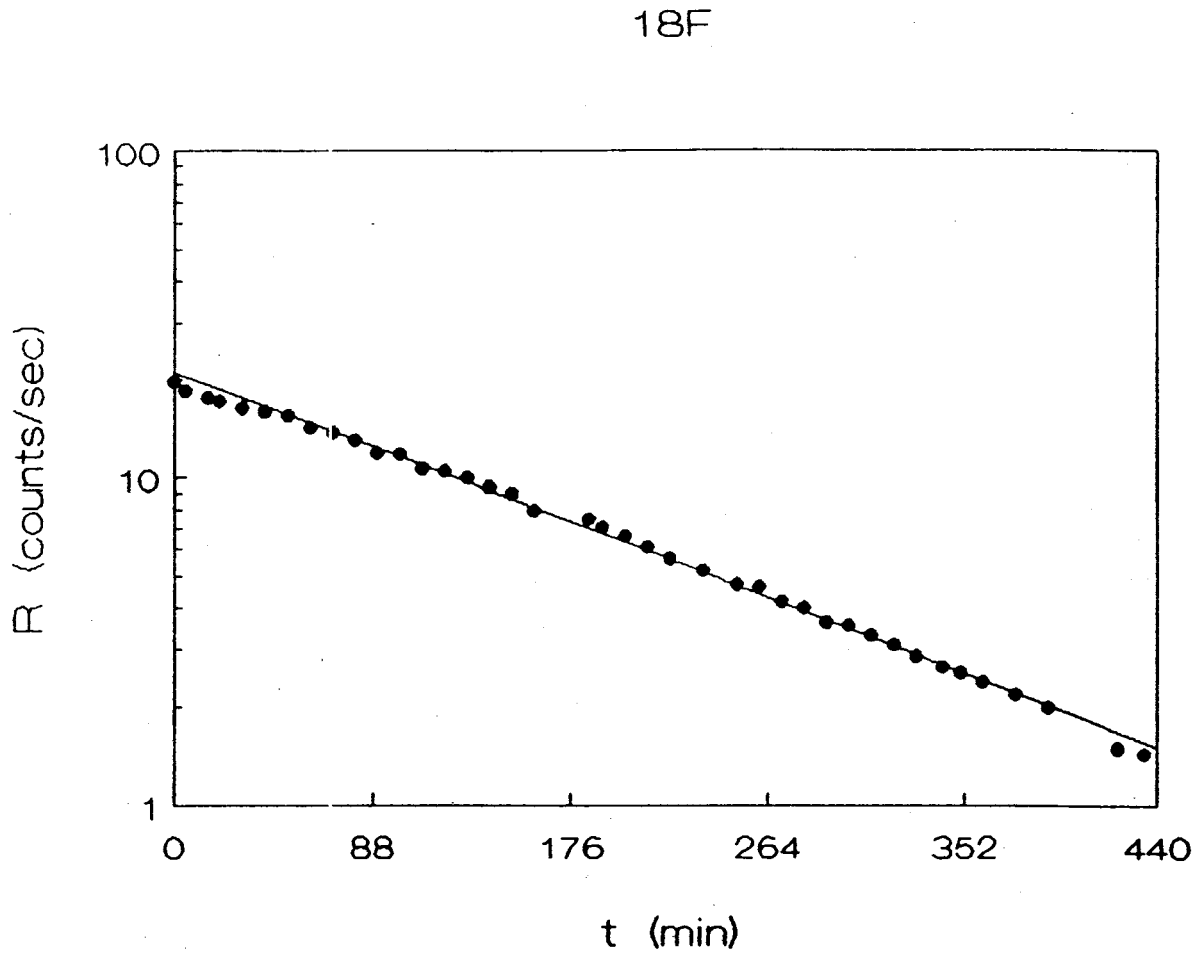

Fig. 8.7 *The variation of the background rate of events* (^{18}F) *in time obtained from the image of the 25 cm phantom filled with* ^{18}F *solution and containing a hot tumour* (^{64}Cu). *The line represents the extrapolation of the low rate data.*

Using the calibration lines of the Ge(Li) detector and of the PET system, the variation of the activities in time of the ^{18}F and ^{64}Cu can be obtained by these two different methods.

Fig. 8.8 shows the dependence of the ^{18}F concentration activity on time (the background region) obtained with Ge(Li) detector and by PET. The PET data are the same for the truncated filter and the modified filter. The concordance between Ge(Li) method and PET method is very good, almost perfect. The starting activity of ^{18}F is 2.2 μCi/ml. That is a total background activity of $\approx$ 11 mCi, which explains the lower detected concentration activities by PET due to dead time losses.

Again, using the calibration lines of the Ge(Li) detector and of the tomograph, the changes in activity of the ^{64}Cu in time can be obtained for these two methods. The results are presented in Fig. 8.9. For the Ge(Li) detector, two activity lines are presented, one taking in consideration the detector dead time and the other one without any dead time corrections. The corrected data for the dead time losses were obtained extrapolating the low count rates values to t = 0. For the PET results, two sets of data corresponding to the two filters used, truncated filter (Filter 1) and modified filter (Filter 2), are included. For the Filter 1, the calibration of the 25 cm diameter phantom was used.

The ^{64}Cu half life obtained with both filters and the Ge(Li) detector is 12.6 h.

The PET data obtained with truncated filter underestimates the real concentration activities in a small tumour up to 3 - 4 times. Therefore the calibration line of the tomograph obtained for a large phantom could not be used in the evaluation of activity in a small tumour.

The modified filter underestimates also the real concentration activities up to 25%. The reason of this discordance can be the fact that the calibration of the tomograph, (Fig. 7.23) was performed for concentration activity up to 1 μCi/ml for ^{68}Ge-^{68}Ga solution. The slope of the ^{64}Cu calibration line is much higher than that of ^{18}F or ^{68}Ga and the extrapolation to high activities ($\approx$ 15 μCi/ml for ^{64}Cu, equivalently to $\approx$ 3.5 μCi/ml for ^{18}F on the same graph) amplifies the errors of the low activities measurements.

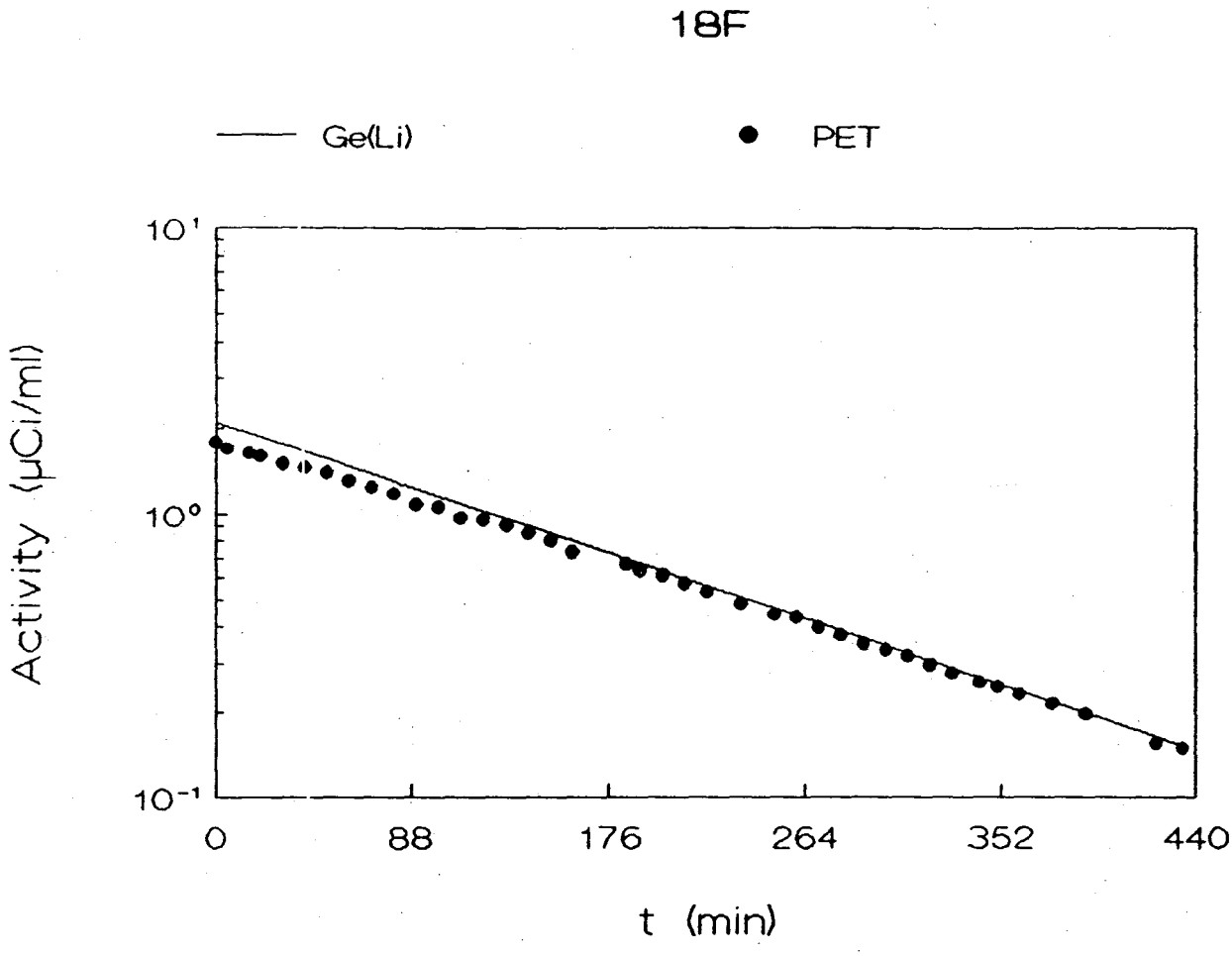

Fig. 8.8 *The concentration activity changes in time in the background activity (^{18}F) given by Ge(Li) detector (full line) and by PET (points). The experiment consists from the 25 cm phantom containing a hot tumour (^{64}Cu) filled with ^{18}F solution.*

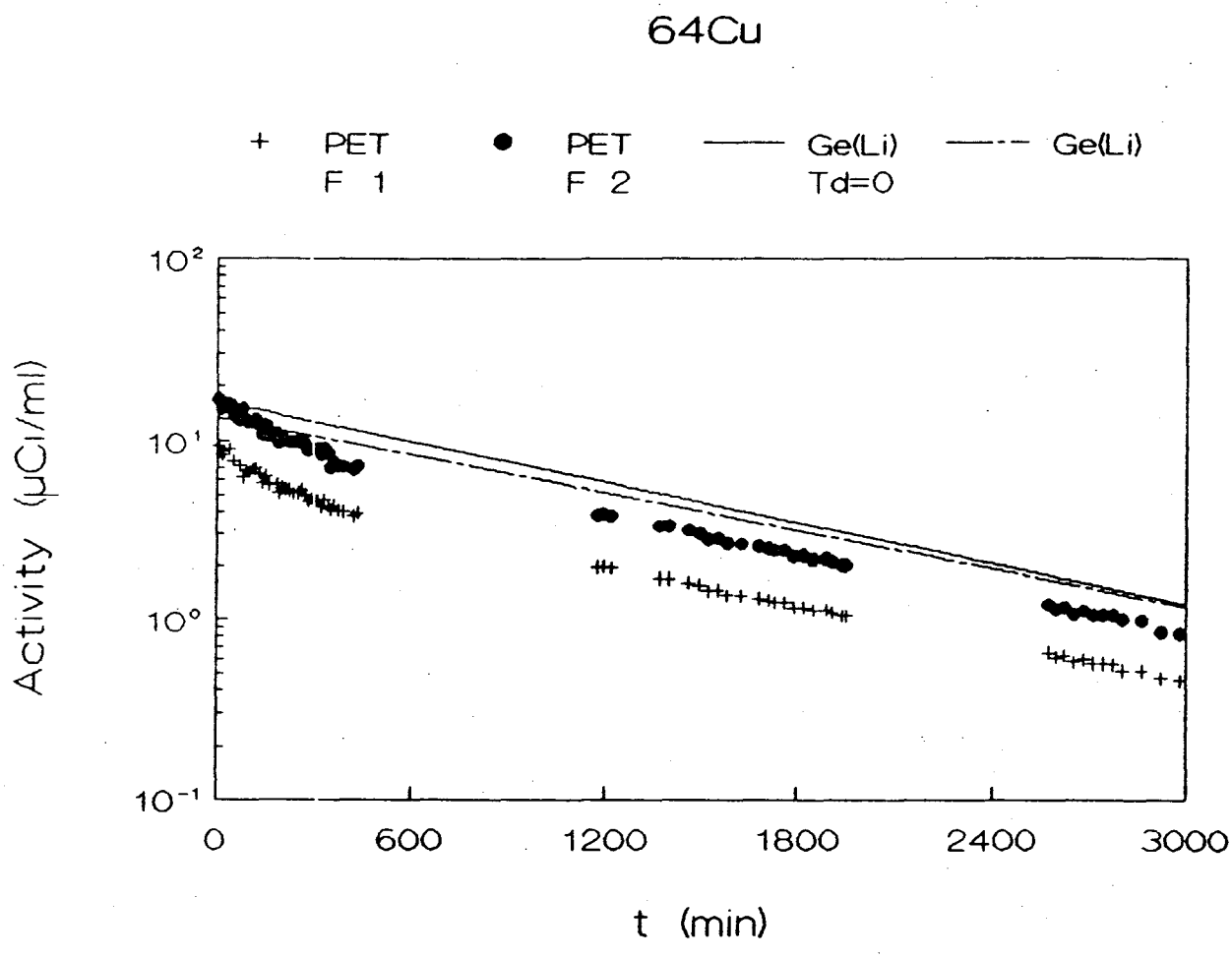

Fig. 8.9 *The variation of the concentration activity in the tumour (^{64}Cu) in time obtained using a* Ge(Li) *detector (lines) and* PET *(points). The* Ge(Li) *data presented are corrected for the detector dead time (full line) or are not corrected for the dead time losses (point line). The* PET *data are obtained for* 15 *point Butterworth filter* (Filter 1) *and for modified filter* (Filter 2).

These results concerning the measurement of two different short lived isotopes in the same time by PET did not have the abnormal behaviour, diverting from the linear dependence determined in [68]. The deviation from a linear dependence in their case is probably due to a higher amplification of the low statistical images and not due to scattering effects from ^{64}Cu high activity region. The activities used in [68] were much lower than those used in this study, and to avoid the effect of amplification of the low statistical images, the time of aquisition for each image slice should have been very long.

From this experiment, the true activity can be obtained by PET for detected rates less than $\approx$ 15000 counts/sec. Over these values, corrections for the dead time of the system losses are necessary to get the real activity.

The last test of the accuracy of the method for absolute evaluation of the concentration activity by PET consists in studying the changes in time for the tumour-to-nontumour activity ratios, in the experiments containing two different short-lived isotopes such as ^{64}Cu and ^{18}F.

The dependence of the tumour-to-nontumour activity ratio on time is presented in Fig. 8.10. The test values were obtained from Ge(Li) detector evaluations. These activities values are corrected for the detector dead time. The PET values presented in Fig. 8.10 were obtained using the two filters, 15 point filter (Filter 1) and modified filter (Filter 2), and the activities values are not corrected for the system dead time.

The tumour-to-nontumour activity ratios values from the images reconstructed using truncated filter are much smaller than the real values and less sensitive to changes in time. The modified filter gives better results. The starting time ratio values seems to be slightly higher due to lower activity background values, then they underestimate the real values due to lower ^{64}Cu activity evaluations. Very high tumour-to-nontumour ratios ($\approx$ 80) are not possible to be detected by PET due to the fact that there is a background generated by the reconstruction procedure even when no activity is used in that region (see Fig. 7.10)

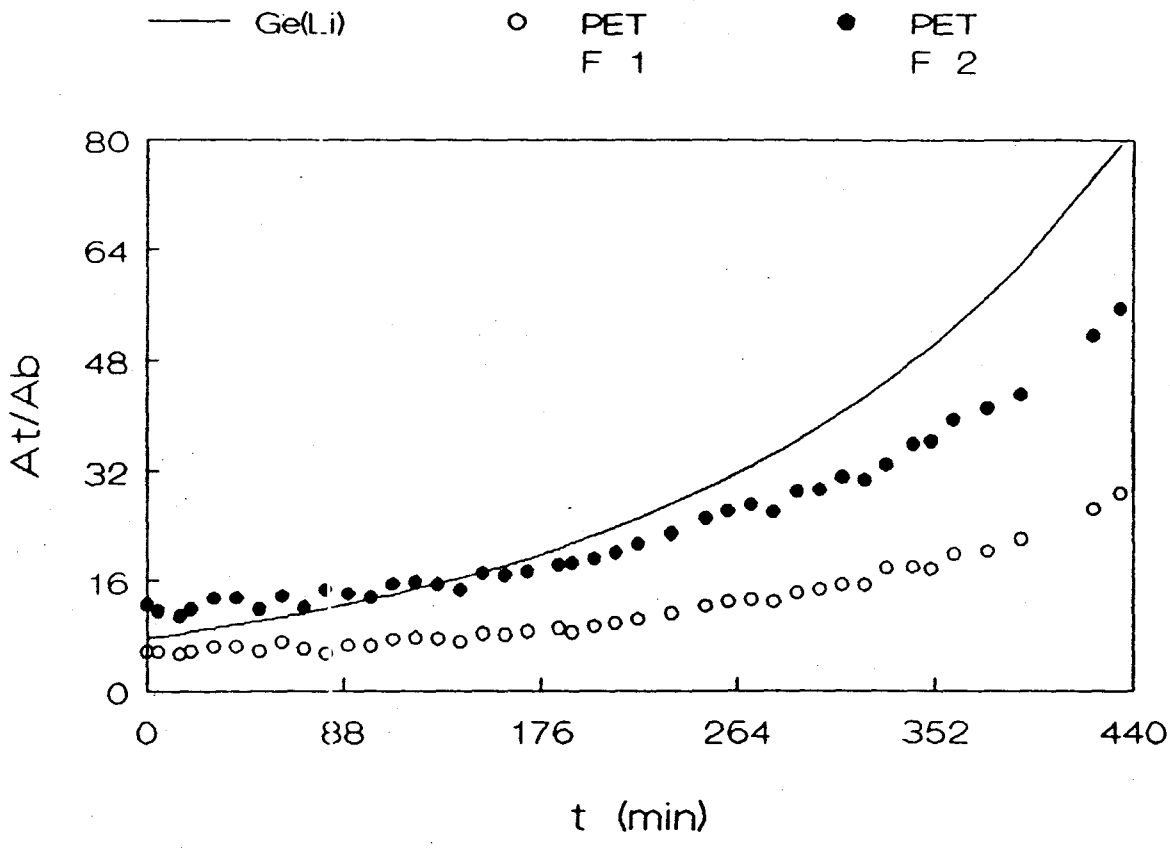

Fig. 8.10 *The tumour-to-nontumour activity ratio variation in time, obtained using* Ge(Li) *detector (corrected data for dead time losses) and PET, using* 15 *point filter* (Filter 1) *and modified filter* (Filter 2).

9. THE ADVANTAGES AND THE LIMITATIONS OF THE METHOD FOR ABSOLUTE EVALUATIONS BY PET.

9.1 The advantages of the method.

The results of surveys in an effort to identify problems and potential solutions associated with data acquisition and analysis in computer assisted tomography, indicated the necessity to establish guidelines and to seek and disseminate information within this domain. The ability to take full advantage of the power of functional imaging and to maintain credibility requires standardized, reproductibile and accurate methods of obtaining, analyzing and reporting the results data as well as recognition of the limits of these approaches. This is the area in which the physicist can bring his or her contribution.

The proposed criteria for optimal solution to the problem of functional image acquisition and analysis are [65]:

1. - accurate,
2. - reproductibile,
3. - independent of the tracer used,
4. - independent of the instrument spatial resolution,
5. - when possible, independent of imaging technique,
6. - minimize subjectivity and investigator bias,
7. - fixed assumption about normal anatomy not required,
8. - acceptable to subject level of tolerance (headholders, etc),
9. - performs well in serial studies of the same patient and individual study of separate patients in a population,
10. - capable of evolving toward greater accuracy as information and instruments improve,
11. - reasonable in cost,
12. - equally applicable in both clinical and research settings,
13. - time efficient for both data acquisition and analyze.

The method for absolute quantitation presented in this study tried to solve the most important aspects of quantitation in computer assisted tomography systems:

- to evaluate the dimension of the tumour,
- to determine the *position* of the tumour,
- to measure the amount of drug accumulated in the tumour,
- to evaluate the tumour-to-nontumour activity ratios.

The quality control terms describing the "goodness" of any assay are:

- accuracy -- giving the closeness to the true value,
- precision -- reproductibility of the same measurement, and
- sensivity -- representing the smallest difference between two measurements that can be reliablely distinguished.

By this method of absolute measurements by PET the dimension of a tumour may be evaluated in a sensible way using the calibration of the FWHM values of the tumour image counts distributions in absolute units (mm). The method is more precise in detecting the real dimension of a tumour than in finding its dimension on a predefined position on the distribution of counts in the image, and it is useful for any shape and size of the tumours or even for a heterogeneous activity distribution. The middle point of FWHM values on X and Y axes can be helpful to fix the *position* of the tumour on the image.

The accuracy of this method of absolute evaluation of concentration activities from the image is strongly related to the introduction of the new modified filter. Eliminating the high noise background generated by a truncated filter, the image sensivity and contrast were increased and the absolute evaluations of the activities became possible in a pixel-by-pixel way.

The precision of the evaluation of the concentration activity in each pixel of the image given by standard deviation, lies in statistical limits.

Unlike the truncated filter, for the modified filter, even the image represents an amplification of the real distribution of events, this amplification is constant for the whole image. In this way, the image itself represents a reflection of the real distribution of activity in the slice of the phantom (or brain) under investigation.

The filtered back-projection of an image using the modified filter reproduces quantitatively the contours and the concentration activity changes in a studied slice, eliminating the tumour volume dependence, the surrounding volume dependence and the tumour-to-nontumour ratios dependence obtained with the truncated filter.

Once this difficult step is understood and overcome, the analyzed image reveals new and interesting aspects. The most important aspect is the unique calibration line of the tomograph that can be obtained, relating the image count rate directly, in an unique way, to the concentration activities, regardless of the tumour-to-nontumour ratios or the volumes under investigation. Now, finally, the whole image can be represented on an absolute colour scale (μCi/ml), the absolute concentration activity of each pixel (or volume element from the body) being recorded without any subjective intervention of the investigator.

The accuracy and the reproductibility of the method was tested for short-lived isotopes. It seems that this method for absolute quantitation could be as accurate as a Ge(Li) detector evaluation of corcentration activity. This is understandable if we think that, in fact, the complicated system of 160 BGO crystals operating in coincidence (one detector with other 61 detectors) can be seen, in a simplified mode, as an effective system consisting from two detectors operating in coincidence. The multidetector system generates a complicated reconstruction procedure capable to perform a bidimensional image, however falsifying the truth if an improper filter is used.

This method permits to study the image of a cold tumour exactly in the same way as before, of a hot tumour. This was impossible to obtain with the truncated filter in the reconstruction process.

The high activity studies revealed that the effective dead time of the system is more important than the corrections for random and scattered coincidences when absolute quantitations have to be done. The method is valuable even at very high activities if beforehand evaluations of the dead time corrections are performed.

This method for absolute quantitation is simple reliable and can be applied to any computer assisted imaging systems with some adequate modifications. The cost to implement the method is minimum possible. Each instrument has to be calibrated once and only few more programs are necessary to obtain a colour image in absolute units and to evaluate the dimension and the *position* of a tumour (or organ). Occasionally, the calibration of the instrument has to be verified.

9.2 The limitations of the method.

The principal limitations of this method are related to the fact that this study is not completed yet.

Only two dimensions of tumours were studied, 1.8 cm and 4.8 cm diameter. Intermediary values, larger values than 4.8 cm and smaller diameters than 1.8 cm presenting a practical interest should be included in a study. It is very probable that for very small tumour diameters, the linear dependence of the FWHM on tumour diameter will not be the same as in Fig. 7.3.

Another question arises for the position of the tumour in the phantom. The reconstruction process gives a perfect image in the centre of the image, but the image is deformed towards to the edges of the phantom. This aspects should be studied with a phantom having different dimensions of the tumour in different positions. The same experiment can solve the *position* of the tumour using FWHM/2 point versus place in the phantom.

The filter introduced here and its results were studied for one case, the modified filter, in order to compensate for the effect of truncation in real space. An open solution can be the unmodified 23 (or more) point filter which probably can give good results also. Even, if this 23 point filter is modified, the modification will be much smaller. The quality of the filter should be verified theoretically before it will be tested experimentally.

The test of the method using modified filter at very high activities did not give the best result in tumour concentration evaluations. That is a calibration including high activities as well as low activities is imposed.

It seems that very high activities do not represent a limitation of the method but a limitation due to dead time of the system. If the dead time corrections are evaluated (and this can be done), the method is valuable even for very high activities (> 10 mCi).

The non-concordance between the Ge(Li) results and the results of this method at high activities, reflects in the tumour-to-nontumour ratio variations in time. This represents a very sensible way to test the quality of the filter and of the calibration. This aspects should be studied more.

Very high tumour-to-nontumour activity ratios (> 80) represents a limitation of the PET method. The reconstruction procedure creates a background even without any activity in surrounding volume which can not be avoided.

At the opposite side, very low activities (low statistics images) presents difficulties in evaluating the concentration activities. Abnormal amplifications of the image counts, regardless of the filter used, could generate false results. It is very probable that background activity can influence this low statistics evaluations as well. This is another problem to be studied also.

The results obtained using a phantom are inferred to a brain image. To understand better a more complicated image, the experiment must be enhanced using more than one tumour cylinder, filled with different concentration activity solutions and placed in different background activities.

10. CONCLUSIONS.

The goal of this study was to find a method capable to realize absolute evaluations in Positron Emission Tomography, in a pixel-by-pixel way. The method should define the dimension and the *position* of a tumour, to evaluate the amount of activity (per pixel) delivered to the tumour and to the surrounding tissues, to determine the tumour-to-nontumour activity ratios, from the reconstructed image.

The proposed method is based on:

- the use of FWHM values of the distribution of counts in the image to determine the dimension and the *position* of the tumour,
- the introducing of a modified filter in the filtered back-projection method of the reconstruction of the image,
- the calibration of the tomograph in concentration activities.

The method of defining the dimension and the position of the tumour using the calibration of the FWHM values in absolute units (mm), seems to be very sensible and accurate. This method can be applied to any shapes and sizes of tumours.

The absolute evaluations of the concentration activities in the tumour and surrounding volume in statistical limits, was possible after the understanding and corresponding correcting the effects of truncation of a filter in real space, on the image. Using the modified filter, the resulted image represents a reflection of the real activity distribution in the studied slice.

The tumour concentration activity evaluation does not need any "recovery coefficient" corrections for any dimension of the tumour (at least for the dimension of the tumour greater than the tomograph resolution), when the tumour is surrounded by activity.

The rate (per pixel) in the image can be directly correlated to the concentration activities used without any tissue volumes or tumour-to-nontumour activity ratio interference.

A test procedure using short-lived isotopes and a Ge(Li) detector was introduced to verify the accuracy of this method for absolute quantitation. The concordance between this method and Ge(Li) evaluations was almost perfect, proving that PET measurements can give the same accurate results as a Ge(Li) detector.

The high activity measurements showed that the effective dead time of the system affects the absolute measurement of concentration activity more than the random or scattered coincidences.

The proposed method is very simple, accurate, reliable, independent of the imaging system and reasonable in cost for a practical utilization.

In conclusion, a complete study following the procedure presented, would be finalized in a quantitative image capable of defining the *position* and the dimension of a tumour as well as the concentration activity delivered to the tumour and to surrounding tissues. The method permits to obtain the concentration activity in each pixel of the image, therefore an absolute colour scale of the image can be used.

There are many direct medical applications of the implementation of this method. Between them, a definition of the degree of intensity of a disease supposing that it is proportional to the amount of drug absorbed by the organ under investigation, a systematic study of the different kinds of tumour cells differentiated after the amount of drug delivered to the tumour, controlled chemotherapy of the cancer, etc.

REFERENCES

[1] C. Grouzel, Pharmaceuticals for Positron Emission Tomography. In: Physics and Engineering of Medical Physics, ed. R. Guzzardi, NATO ASI Series, Series E: Applied Science, No. 119, 1987, p. 750.

[2] A.P. Wolf and J.S. Fowler, Positron Emitter-Labelled Radiotracers - Chemical Considerations. In: Positron Emission Tomography, ed. M. Reivich and A. Alavi, New York, 1985, p. 63.

[3] G.D. Robinson Jr., Generator Systems for Positron Emitters. In: Positron Emission Tomography, ed. M. Reivich and A. Alavi, New York, 1985, p. 81.

[4] A.P. Wolf and J.S. Fowler, Labeled Compounds for Positron Emission Tomography. In: Positron Emission Tomography of the Brain, ed. W.D. Heiss and M.L. Phelps, Springer-Verlag, Berlin, Heidelberg, New York, 1983, p. 52.

[5] G. Firnau, R. Chirakal and E.S. Garnett, Aromatic Radiofluorination with [^{18}F] Fluorine Gas: 6-[^{18}F] Fluoro-L-Dopa. In: J. Nucl. Med., 25, 1984, p. 1228.

[6] A.P. Wolf and J.S. Fowler, Cyclotron and Positron Emitting Radiopharmaceuticals. In: Physics and Engineering of Medical Physics, ed. R. Guzzardi, NATO ASI Series, Series E: Applied Science, No. 119, 1987, p. 721.

[7] T.F. Budinger, G.T. Gullberg and R.H. Huesman, Emission Computed Tomography. In: Topics in Applied Physics, vol. 32, ed. G.T. Herman, Springer-Verlag, Berlin, Heidelberg, New York, 1979. p. 147.

[8] M. Reivch, Cerebral Glucose Consumption: Methodology and Validation. In: Positron Emission Tomography, ed. M. Reivich and A. Alavi, New York, 1985, p. 131.

[9] M.A. Mandelkern and M.E. Phelps, Methods and Instrumentation for Positron Emission Tomography. In: Diagnostic Nuclear Medicine, ed. A. Gottschalk, and al., 1988, p. 133.

[10] S.E. Derenzo and T.F. Budinger, Advanced Instrumentation for Positron Emission Tomography. In Physics and Engineering of Medical Physics, ed. R. Guzzardi, NATO ASI Series, Series E: Applied Science, No. 119, 1987, p. 855.

[11] M.M. Ter-Pogossian, Positron Emission Tomography (PET). In: Three-Dimensional Biomedical Imaging, ed. R.A. Robb, CRC Press Inc., vol. 2, 1985, p. 41.

[12] M.M. Ter-Pogossian, PET Instrumentation, In: Positron Emission Tomography, ed. M. Reivich and A. Alavi, New York, 1985, p. 43.

[13] S. E. Derenzo, Potential Improvements in Instrumentation for PET. In: LBL-20215, 1984

[14] S.E. Derenzo, Recent Developments in Positron Emission Tomography (PET) Instrumentation. In: SPIE vol. 671, Physics and Engineering of Computerized Multidimensional Imaging and Processing, 1986, p. 232.

[15] S.E. Derenzo, Gamma-Ray Spectroscopy Using Small, Cooled Bismuth Germanate Scintilators and Silicon Photodiodes. In: Nucl. Instr. and Meth. in Phys. Res., 219, 1984, p. 117.

[16] B.E. Oppenheim and R.N. Beck, The Scintillation Detector. In: Diagnostic Nuclear Medicine, ed. A. Gottschalk, and al., 1988, p. 55.

[17] L. Eriksson and al., Design Characteristics of Multiring Positron Camera System for Emission Tomography of the Brain. In: Positron Emission Tomography of the Brain, ed. W.D. Heiss and M.L. Phelps, Springer-Verlag, Berlin, Heidelberg, New York, 1983, p. 40.

[18] C.L. Morgan, Basic Principles of Computed Tomography. University Park Press, Baltimore, 1983.

[19] R. Bracewell, The Fourier Transform and Its Applications, McGraw-Hill Book Company, 1965.

[20] C. Nahmias, D.B. Kenyon, K. Kouris and E.S. Garnett, Understanding Convolution Backprojection. In: Single Photon Emission Computed Tomography and Other Selected Topics. ed. J.A. Sorenson, Society of Nuclear Medicine, New York, 1980, p. 19.

[21] M.A. King, P.W. Doherty and R.B. Schwinger, Digital Image Filtering of Nuclear Medicine Images. In: Physics of Nuclear Medicine, Recent Advances, ed. D.V. Rao, R. Chandra, M.C. Graham, 1978, p. 310.

[22] E.J. Hoffman, Evaluation of Performance and Accuracy in PET. In: Physics and Engineering of Medical Physics, ed. R. Guzzardi, NATO ASI Series, Series E: Applied Science, No. 119, 1987, p. 802.

[23] E.J. Hoffman, Basic Principles of Positron Emission Computed Tomography. In: Principles of Radionuclide Emission Tomography, ed. D.E. Kuhl, 1982, p. 202.

[24] E.J. Hofman, J.B. Barton, M.E. Phelps and S.C. Huang, New Design Concepts for Quantitative Emission Computed Tomography of the Brain. In: Positron Emission Tomography of the Brain, ed. W.D. Heiss and M.L. Phelps, Springer-Verlag, Berlin, Heidelberg, New York, 1983, p. 30.

[25] M.E. Phelps, S.C. Huang, E.J. Hoffman, D. Plummer and R. Carson, An Analyze of Signal Amplification Using Small Detectors in Positron Emission Tomography. In: J. Comput. Assist. Tomogr., 6(3): 1982, p. 551.

[26] M.M. Ter-Pogossian and al., Photon Time-of-Flight Assisted Positron Emission Tomography. In: J. Comput. Assist. Tomogr., 5: 1981, p. 227.

[27] S.C. Huang, E.J. Hoffman, M.E. Phelps and D.E. Kuhl, Quantitation in Positron Emission Computed Tomography: 2. Effects of Inaccurate Attenuation Correction. In: J. Comput. Assist. Tomogr., 3(6): 1979, p. 804.

[28] M.E. Casey and E.J. Hoffman, Quantitation in Positron Emission Computed Tomography: 7. A Technique to Reduce Noise in Accidental Coincidence Measurements and Coincidence Efficiency Calibration. In: J. Comput. Assist. Tomogr., 10(5): 1986, p. 845.

[29] M. Bergstrom, et al., Correction for Scattered Radiation in a Ring Detector Positron Camera by Integral Transformation of the Projections. In: J. Comput. Assist. Tomogr., 7: 1983, p. 42.

[30] E.J. Hoffman, S.C. Huang and P.H. Phelps, Quantitation in Positron Emission Computed Tomography: 1. Effect of Object Size. In: J. Comput. Assist. Tomogr., 3(3), 1979, p. 299.

[31] E.J. Hoffman, S.C. Huang, D. Plummer and M.E. Phelps, Quantitation in Positron Emission Computed Tomography: 6. Effect of Nonuniform Resolution. In: J. Comput. Assist. Tomogr., 6(5), 1982, p. 987.

[32] G. Germano and E.J. Hoffman, Investigation of Count Rate and Dead-Time Characteristics of a High Resolution PET System. In: J. Comput. Assist. Tomogr., 12(5), 1988, p. 836.

[33] S.E. Derenzo, Mathematical Removal of Positron Range Blurring in High Resolution Tomography. In: IEEE Trans. Nucl. Sci., vol. NS-33, No. 1, 1986, p. 565.

[34] S.E. Derenzo and al., Initial Results from the DONNER 600 Crystals Positron Tomograph. In: IEEE Trans. Nucl. Sci., vol. NS-34, No. 1, 1987, p. 321.

[35] H. Uchica, T. Yamashita, M. Iida and S. Muramatsu, Design of a Mosaic BGO Detector System for Positron CT. In: IEEE Nucl. Sci., Vol. 33, No. 1, 1986, p. 464.

[36] C.A. Burnham, and al., Cylindrical PET Detector Design. In: IEEE Trans. Nucl. Sci., Vol. 35, No. 1, 1988, p. 675.

[37] M.E. Casey and R. Nutt, A Multicrystal Two Dimensional BGO Detector System for Positron Emission Tomography. In: IEEE Trans. Nucl. Sci., Vol. 33, No. 1, 1986, p. 460.

[38] S. Holte and al., A Preliminary Evaluation of a Positron Camera System Using Weighted Decoding of Individual Crystals. In: IEEE Trans. Nucl. Sci., Vol. 35, No. 1, 1988, p. 730.

[39] S.E. Derenzo, T.F. Budinger and R.H. Huesman, Detectors for High Resolution Dynamic Positron Emission Tomography. In: The Metabolism of the Human Brain Studied with Positron Emission Tomography, ed. T. Greitz et al., Raven Press, New York, 1985, p. 21.

[40] A.W. Lightstone and R.J. McIntyre, A Bismuth Germanate Avalanche Photodiode Module Designed for Use in High Resolution Positron Emission Tomography, In: IEEE Trans. Nucl. Sci., Vol. 33, No. 1, 1986, p. 456.

[41] S.C. Huang, E.J. Hoffman, M.E. Phelps and D. Kuhl, Quantitation in Positron Emission Computed Tomography: 3. Effect of Sampling. In: J. Comput. Assist. Tomogr., 4(6), 1980, p.819.

[42] T.F. Budinger, S.E. Derenzo, W.L. Greenberg, G.T. Gulberg and R.H. Huesman, Quantitative Potentials of Dynamic Emission Computed Tomography. In: J. Nucl. Med., 19, 3, 1978, p. 309.

[43] R.A. Hawkins, D.E. Kuhl and M.E. Phelps, Positron Emission Tomography of Brain. In: Diagnostic Nuclear Medicine, ed. A. Gottschalk, and al., 1988, vol. 2, p. 852.

[44] W.D. Heiss, and al., Atlas of Positron Emission Tomography of the Brain, Springer-Verlag, Berlin, Heidelberg, New York, Tokyo, 1985.

[45] C. Nahmias, G. Firnau, and E.S. Garnett, Performance Characteristics of the McMaster Positron Emission Tomograph. In: IEEE Nucl. Sci., 31(1), 1984, p. 637.

[46] G. Firnau, et al., Fluorine-18 Labeled Tracers for the Investigation of Neuro-Transmitters., In: J. Label. Comp. Radiopharm., 16(1), 1979, p. 19.

[47] K.L. Leenders et al., Brain Dopamine Metabolism in Patients with Parkinson's Diseases Measured with PET. In: J. Neurol. Neurosurg. Psychiatry, 49(8), 1986, p. 953.

[48] R.P. Beaney and A.A. Lammertsma, Use of PET in Oncology. In: Positron Emission Tomography, ed. A.A. Liss, Inc., 1985, p. 425.

[49] T.F. Bucinger, Quantitative Nuclear Medicine Imaging: Application of Computers to the Gamma Camera and Whole Body Scanner. In: Recent Advances in Nuclear Medicine - Progress in Atomic Medicine, ed. J.H. Lawrence, vol. 4, 1980, p. 41.

[50] D.V. Rao, R. Chandra and M.C. Graham, Principle of Positron Emission Tomography. In: Physics of Nuclear Medicine, Recent Advances, Medical Physics Monography, Vol. 10, 1983, p. 384.

[51] E.J. Hoffman, M. van der Stee, A.R. Ricci and M.E. Phelps, Prospects for Both Precision and Accuracy in Positron Emission Tomography. In: Ann. Neurol., 15(Suppl), 1984, p. S25.

[52] J.O. Eichling, C.S. Higgins and M.M. Ter-Pogossian, Determination of Radionuclide Concentrations with Positron CT Scanning (PETT). In: J. Nucl. Med., 18, 1977, p. 845.

[53] E.J. Hoffman and J.A. Correia, I. The Role of Physics in Positron Emission Tomography and Single Photon Emission Computed Tomography Image Processing. In: J. Cereb. Flow. Metab., Vol. 7 No. 2, 1987, p. S4.

[54] J.E. Holden and R. Carson, III. Biomathematical Aspects of Physiological Brain Imaging. In: J. Cereb. Flow. Metab., Vol. 7, No. 2, 1987, p. S11.

[55] G.L. DeNardo, et al., Quantitative SPECT of Uptake of Monoclonal Antibodies. In: Seminars in Nucl. Med., Vol. XIX, No. 1, 1989, p. 22.

[56] G. Iosilevsky et al., A Practical SPECT Technique for Quantitation of Drug Delivery to Human Tumours and Organ Absorbed Radiation Dose. In: Seminars in Nucl. Med., Vol XIX, No. 1, 1989, p. 33.

[57] P.B. Zanzonico, R.E. Bigler, G. Sgouros and A. Strauss, Quantitative SPECT in Radiation Dosimetry. In: Seminars in Nucl. Med., Vol. XIX, No. 1, 1989, p. 47.

[58] M. Paterson, SIGPRO program.

[59] R.E. Bigler, T. Yoshizumi and M. Graham, Positron Emission Tomography: Intercomparison Measurements, Specifications, Test Procedure, Figure-of-Merit Optimization, Scatter Measurements. In: Physics of Nuclear Medicine, Recent Advances, Medical Physics Monography, ed. D.V. Rao and R. Chandra, No. 10, 1983, p. 411.

[60] A. Popescu and T. Farell, A Filter Designed for Absolute Quantitation in Computer Assisted Tomography, to be published.

[61] E.T. Tsui and F. Budinger, A Stochastic Filter for Transverse Section Reconstruction. In IEEE Trans. Nucl. Sci. NS-26, 2, 1979, p. 2687.

[62] A. Popescu, A Method for Pixel-by-Pixel Absolute Quantitation in Positron Emission Tomography, to be published.

[63] D.E. Kuhl et al., The Mark IV System for Radionuclide Computed Tomography of the Brain. In: Radiology, 121, 1976, p. 405.

[64] J.O. Eichling, C.S. Higgins and M.M. Ter-Pogossian, Determination of Radionuclide Concentration with Positron CT Scanning (PETT): Concise Communication. In: J. Nucl. Med., 18, 6, 1977, p. 845.

[65] J.C. Mazziotta and S.H. Koslow, Assessment of Goals and Obstacles in Data Acquisition and Analysis from Emission Tomography: Report of a Series of International Workshops. In: J. bCereb. Blood Flow and Metab., 7, 1987, p. S1.

[66] B. Soderborg, M. Dahlborn, N. Karlberg and J. Virgin, Determination of Organ Volume by Single Photon Emission Tomography. In: J. Nucl. Med., Vol. 24, 12, 1983, p. 1197.

[67] B.E. Cooke and A.C. Evans, A Phantom to Assess Quantitative Recovery of Positron Tomographs. In: J. Comput. Assist. Tomogr., 7(5), 1983, p. 876.

[68] A. Popescu, Concentration Activity Evaluation of Short-Lived Isotopes by Positron Emission Tomography, to be published.